8-26-2022 4:00 PM

Anatomical and Functional Lung Imaging with Volumetric Computed Tomography in Non-Small Cell Lung Cancer

Heather Young, *The University of Western Ontario*

Supervisor: Gaede, Stewart, *London Regional Cancer Progarm, University of Western Ontario*
Co-Supervisor: Lee, Ting-Yim, *Robarts Research Institute, Lawson Research Institute, University of Western Ontario*
A thesis submitted in partial fulfillment of the requirements for the Doctor of Philosophy degree in Medical Biophysics

Recommended Citation

Young, Heather, "Anatomical and Functional Lung Imaging with Volumetric Computed Tomography in Non-Small Cell Lung Cancer" (2022). *Electronic Thesis and Dissertation Repository*. 8858.
https://ir.lib.uwo.ca/etd/8858

Abstract

Non-small cell lung cancer (NSCLC) is one of the most diagnosed cancers in Canada, and the leading cause of cancer deaths. A significant challenge in treating NSCLC is balancing aggressive treatment with the potentially severe side effects. In radiation therapy, the management of respiratory motion and the risks of radiation-induced lung injury (RILI) pose significant challenges. 4-dimensional computed tomography (4D-CT) is an important part of motion management, but images often suffer from motion-induced artifacts. Volumetric CT scanners with wide axial field-of-view (aFOV) may reduce these artifacts and present an opportunity to advance CT-based functional lung imaging.

Chapter 2 presents a phantom imaging study to investigate the suitability of a 256-slice volumetric CT (vCT) scanner for radiotherapy treatment planning. The density of the highest density materials was under-estimated by the scanner, which can be addressed with the use of an appropriate relative electron density (RED) curve. An average RED curve for all aFOV settings may be used.

Chapter 3 presents a study of phantom and NSCLC patient 4D-CT images acquired on a clinical scanner and a vCT scanner. The v4D-CT images were re-sampled to simulate a conventional acquisition using a narrow aFOV clinical scanner. The phantom images demonstrated that target contouring variability decreased in v4D-CT imaging as compared to clinical 4D-CT. In the patient images, mean Hausdorff distance between organs at risk (OAR) contours was significantly correlated to respiratory phase, indicating that motion artifacts contribute to this variability.

Chapter 4 presents a novel acquisition and analysis pipeline to image lung ventilation (V), perfusion (Q) and V/Q ratio in a single volumetric CT scan. In a porcine study, these images of V and Q were significantly correlated to standard Xe-enhanced ventilation and PET perfusion images in voxel-wise analysis. In a NSCLC patient study, the images were sensitive to changes in V and Q between baseline imaging and follow-up 6 weeks after radiotherapy.

In this thesis, I demonstrate that volumetric CT scanners are suitable for use in radiation therapy simulation and treatment planning, and detail two scanning protocols which may reduce the challenges posed by respiratory motion and RILI risk in NSCLC.

Keywords

X-ray computed tomography, 4-dimensional computed tomography (4D-CT), non-small cell lung Cancer, functional lung imaging, ventilation imaging, perfusion imaging

Summary for Lay Audience

Non-small cell lung cancer (NSCLC) is one of the most diagnosed cancers in Canada, and the leading cause of cancer deaths. Most patients will undergo a combination of therapies which may include surgery, chemotherapy, radiation therapy, and recently, immunotherapy. Approximately one in three patients with NSCLC will undergo radiation therapy, which is the focus of this thesis. When treating this disease, a significant challenge is balancing aggressive treatment to kill the cancer with the potentially severe side effects. In radiation therapy, the management of respiratory motion and the risks of radiation-induced lung injury (RILI) pose significant challenges.

Respiratory motion presents a challenge because patients cannot hold their breath for an entire radiation therapy delivery, and the motion caused by breathing may cause their tumour to move during treatment. To give the maximum possible dose to the tumour and protect the surrounding healthy lungs, this motion must be measured and accounted for in treatment planning and delivery. 4-dimensional computed tomography (4D-CT) is an essential part of this process, in which CT images are acquired while the patient breathes freely. Current clinical CT scanners rely on very consistent patient breathing for this process, which is difficult for many NSCLC patients. Newer CT scanners with wider detectors may be able to improve these images.

In Chapter 2, many materials were scanned in the volumetric CT scanner to test its measurement accuracy. These results showed that the scanner is sufficiently accurate to be used in radiation treatment planning. In Chapter 3, a moving device was imaged using 4D-CT on a clinical and volumetric scanner, and four patients with NSCLC were imaged on both scanners. Analysis of these images showed that the volumetric 4D-CT images more accurately imaged the respiratory motion of organs in the thorax.

In Chapter 4, we developed and tested a method to image air flow (ventilation) and blood flow (perfusion) in the lungs using an injected contrast during one volumetric CT scan. The accuracy of these images was confirmed in an animal study and was demonstrated in two NSCLC patients before and after radiation therapy.

Co-Authorship Statement

The following thesis contains three manuscripts; one has been published and two are in preparation for submission to scientific journals. As the first author, I was a significant contributor to all aspects of the studies as well as the manuscript preparation and submission. Dr. Stewart Gaede, as the principal investigator, provided ongoing guidance and was responsible for study conception, participated in experimental design, data analysis and interpretation, and was responsible for revisions and approval of the manuscripts. Listed below are the specific contributions for all other co-authors for each manuscript contained in this thesis.

Chapter 2 is a technical note entitled “Volumetric computed tomography for radiotherapy simulation and treatment planning” and was published in the *Journal of Applied Clinical Medical Physics* in 2021. This manuscript was co-authored by Heather Young, Claire Keun Sun Park, Oi Wai Chau, Ting-Yim Lee, and Stewart Gaede. As the first author of this work, I was a significant contributor to all aspects of the studies as well as the manuscript preparation and submission. Specific tasks included: image analysis, statistical analysis and interpretation, and drafting and final approval of the manuscript. Claire Keun Sun Park and Oi Wai Chau assisted with image analysis, and interpretation. Image acquisition was performed by Jennifer Hadway, and this work was completed under the supervision of Ting-Yim Lee and Stewart Gaede.

Chapter 3 is an original research article entitled “Reduction of respiratory motion artifacts using volumetric four-dimensional computed tomography” and is in preparation for submission to the journal *Medical Physics*. This manuscript was co-authored by Heather Young, Jeff Kempe, Ting-Yim Lee, and Stewart Gaede. I performed image analysis, statistical analysis and interpretation, and manuscript preparation. Jeff Kempe significantly contributed to image analysis and interpretation, and final approval of the manuscript. Image acquisition was performed by Jennifer Hadway and Tony Wales, and this work was completed under the supervision of Ting-Yim Lee and Stewart Gaede.

Chapter 4 is an original research article entitled “Simultaneous Ventilation and Perfusion Using Computed Tomography: Validation of a Novel Lung Imaging Technique” and is in preparation for submission to the journal *Medical Physics*. This manuscript was co-authored by Heather Young, Feng Su, Ting-Yim Lee, and Stewart Gaede. I significantly contributed to image analysis and interpretation, statistical analysis, and manuscript preparation. Feng Su contributed significantly to image analysis and approval of the final manuscript. Image acquisition was performed by Tony Wales, Jennifer Hadway, Laura Morrison, and Susan Tyler. This work was completed under the supervision of Ting-Yim Lee and Stewart Gaede.

Acknowledgments

Completing this thesis was a tremendous challenge and could never have been accomplished without a wide network of support. I cannot name every person who contributed to this work, but I would like to personally thank the greatest contributors here.

First and foremost, I would like to thank my supervisor Dr. Stewart Gaede. Thank you for your leadership and mentorship for the last several years, leading with enthusiasm and creativity. Thank you for the many valuable lessons you have taught me about research and clinical physics, as you have supported me and prepared me to pursue my medical physics career.

I would also like to thank my advisory committee: Dr. Ting-Yim Lee, thank you for all your thoughtful support and feedback on my work, and for teaching me about imaging physics. Dr. Doug Hoover and Dr. Brian Yaremko, thank you for all the difficult questions you asked which made my research (and cover letters) stronger, and for your support throughout my graduate career.

Many thanks to Jennifer Hadway, Laura Morrison, Susan Tyler, and Tony Wales who performed all non-clinical CT acquisitions in this thesis. Of course, none of this work would have been possible without your hard work. Jennifer, Laura, and Susan also did much more work behind the scenes to make sure my experiments were possible, and to ensure I got the best possible data. Your dedication is greatly appreciated. Thanks also to Barb Barons for all her administrative help and support at LRCP, and for the friendly chats whenever I came downstairs to "visit" (ask for help).

Thank you to my lab mates who taught me about their own work and were very generous with their help and advice. Matt Mouawad, thank you for helping me understand image registration and DICOM header data, and for helping me laugh when work was frustrating. April Chau, thank you for sharing your knowledge and your funny stories, and for reminding me not to stress. Tim Yau, thank you for the sanity breaks and work chats. I enjoyed the opportunities to sit back, shake our heads, and laugh together when things go wrong. Jeff Kempe, thank you for teaching me euchre, for sharing your technical expertise, and for interesting office chats.

I have many supportive friends and family members to whom I owe many thanks. Thank you to Olivia, Eric, Megan, Derek, and Dante for your friendship, encouragement, advice, and the

knowledge you each shared with me. Thank you to my UWaterloo friends for all the laughs and support shared from a distance, and for the wonderful weekends together. Thank you to my mom Ellen, my dad Graham, and my sister Sarah for cheering me through so many years of school. Thank you to my soon-to-be-husband Brandon for your unconditional support in the many forms that it takes, and for the smiles you always bring me. And of course, thanks to Winston the cat for excellent study breaks.

Finally, I would like to express my gratitude for the funding support I have received from the Natural Sciences and Engineering Research Council of Canada, the Lawson Health Research Institute Internal Research Fund, and the Schulich School of Medicine and Dentistry.

Table of Contents

List of Tables

List of Figures

List of Appendices

List of Abbreviations

4D-CT	Four-dimensional computed tomography
aFOV	Axial field-of view
CBCT	Cone-beam computed tomography
CNR	Contrast-to-noise ratio
CT	Computed tomography
CTVI	Computed tomography ventilation imaging
DIBH	Deep inspiration breath hold
FOV	Field-of-view
GTV	Gross tumour volume
Gy	Gray
HU	Hounsfield unit
IMRT	Intensity modulated radiation therapy
ITV	Internal target volume
IRF	Impulse residue function
kV	kilovolt
LDPE	Low-density polyethylene
MAA	Macroaggregated albumin
MLC	Multi-leaf collimator
MRI	Magnetic resonance imaging
NSCLC	Non-small cell lung cancer
OAR	Organ at risk
PET	Positron emission tomography
PMP	Polymethylpentene

PTV	Planning target volume
Q	Perfusion
RED	Relative electron density
RILI	Radiation-induced lung injury
ROI	Region of interest
RTOG	Radiation therapy oncology group
SABR	Stereotactic ablative body radiotherapy
sim4D-CT	Simulated clinical 4-dimensional computed tomography
SPECT	Single photon emission computed tomography
TDC	Time-density curve
V	Ventilation
V/Q	Ventilation-perfusion ratio
v4D-CT	Volumetric 4-dimentional computed tomography
vCT	Volumetric computed tomography
VMAT	Volumetric modulated arc therapy
Xe	Xenon

CHAPTER 1

1 Introduction

1.1 Motivation and Rationale

Lung cancer is one of the most commonly diagnosed cancers in Canada, estimated to represent 13% of new cancer diagnoses in 2021[1]. It is also the leading cause of cancer death in Canada[1], as the disease is often very difficult to treat. Lung cancer treatment often incorporates multiple treatment modalities, and one in three lung cancer patients will receive radiation therapy as part of their treatment regimen[2]. This thesis will discuss patients treated for stage III non-small cell lung cancer (NSCLC), but much of this work is applicable to treatment of other thoracic cancers. Factors which make effective treatment difficult in these patients include respiratory motion that must be managed in treatment planning and delivery, and risk of harmful side-effects due to the radiation dose delivered to surrounding healthy lung tissue. The latter may lead to radiation-induced lung injury, which affects approximately 30% of patients who undergo radiation therapy for NSCLC[3].

This challenge was highlighted in the results of a multi-institutional randomized trial by the Radiation Therapy Oncology Group RTOG 0617[4,5]. The aim of the study was to test the effectiveness of increasing the total treatment dose from 60 Gy to 74 Gy, both in 2 Gy daily fractions, for patients with advanced NSCLC. The study closed recruitment early because the high-dose group suffered significantly decreased overall survival (median survival of 20.3 months in the 74 Gy group, vs 28.7 months in the 60 Gy group, $p = 0.004$) with the volume of the heart that receiving ≥ 5 Gy significantly associated with increased risk of death ($p = 0.004$)[4]. Subsequent analysis showed that the percentage of lung that receives ≥ 20 Gy was significantly related to the risk of Grade ≥ 3 pneumonitis[5]. These results highlight the difficulty of delivering a sufficiently high dose to lung tumours without delivering an unacceptably high dose to the healthy lungs and heart, which may lead to clinically significant side effects or even premature death.

This thesis will explore some of the technological advances which may be used to improve accuracy of planning and delivering radiation therapy to moving tumours in the lung. It will focus on the opportunities presented by using a volumetric computed tomography (CT) scanner for 4-dimensional computed tomography (4D-CT) imaging for treatment planning, and for functional imaging which may provide clinically valuable information about the spatial distribution of lung function to minimize the risks of radiation pneumonitis. In this chapter, the background information necessary to understand and motivate the research presented in Chapters 2 to 4 will be summarized.

1.2 The Lungs

The lungs are a complex parallel organ which facilitate the delivery of oxygen to the bloodstream and the removal of carbon dioxide from the blood so it can be exhaled. This process is called gas exchange. It is achieved through a complex branching structure of airways and blood vessels which optimize the flow of air and blood to the respiratory regions of the lungs, where gas exchange takes place, and maximize the cross-sectional area over which gas exchange occurs. This section will detail the anatomy of the lungs, define ventilation and perfusion, and how they are measured.

1.2.1 Lung Anatomy

The lungs are made up of branching airways and blood vessels, leading air and blood to the respiratory zone of the organ where oxygen-rich air and deoxygenated blood pass over a large surface area of very thin tissue in the alveoli. Gas exchange occurs here, in the respiratory zone[6]. The anatomical structure of the lungs is shown in Figure 1-1. The lungs are surrounded by a thin, smooth membrane called the pleura, and cells which produce pleural fluid, allowing the outer surface of the lungs to slide against the inner surface of the chest wall during breathing[6].

The airways begin at the mouth and nose, where air is brought in from the environment and travels down the trachea into the thorax. The trachea bifurcates to form the first generation of bronchi, with one travelling to each lung. The bronchi continue to bifurcate approximately 23 times in total, until forming the terminal bronchioles which are less than 1 mm in diameter. The airways from the trachea to the terminal bronchioles form the conducting zone of the lungs, the function of which is the delivery of air to the respiratory zone. The conducting airways do not contain any alveoli, so they do not participate in gas exchange. The respiratory zone begins with respiratory bronchioles (which have alveoli on their walls), alveolar ducts, and finally alveoli. These generations of airways are collectively called acini, which contain alveoli and are the functional units of the lung[6]. The airways from the trachea to the bronchi are structurally supported by cartilage and are wrapped by smooth muscles which control airway diameter. The bronchioles and subsequent generations contain no cartilage or smooth muscle and are structurally supported by the complex network of tissues which make up the acini[7].

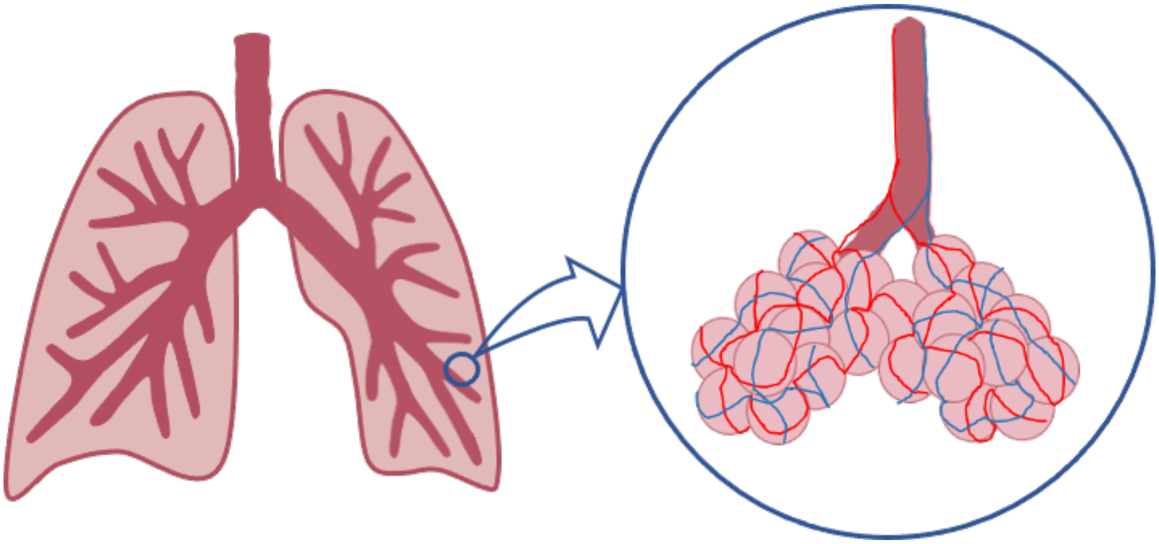

Figure 1-1 Lung anatomy.
Conducting airways, beginning with the trachea, bifurcate and bring air throughout the lungs as shown on the left. The terminal bronchiole branches into respiratory bronchioles which will terminate at alveolar sacs, shown on the right. The alveoli are surrounded by networks of capillaries, and gas exchange occurs here.

The lungs contain a low-pressure pulmonary blood supply to oxygenate blood from the right ventricle of the heart, and a high-pressure systemic blood supply to circulate oxygenated blood to the body from the left ventricle. The pulmonary arteries follow the same branching structure as the bronchi, forming a network of capillaries surrounding the alveoli. The walls of the bronchioles and alveoli are extremely thin, made largely of cells which are specialized to allow gas exchange[6].

1.2.2 Lung Ventilation and Perfusion

Ventilation is the flow of gas into the lungs through breathing, defined as the volume of gas entering a region per unit time (usually measured in units of L/min). It may describe total gas flow to the lungs per minute but can also be applied to smaller units within the lung, such as alveolar ventilation. Perfusion is analogous to ventilation in that it is also a measurement of flow. Perfusion is defined as the flow of blood through a region per unit time, and may apply to the lung or to the alveoli[6]. Air and blood flow through networks of branching airways and vessels as described above. When they reach the alveoli, they pass over a large surface area separated by a thin tissue layer across which gas exchange occurs.

The flow of air into and out of the lungs is controlled by the muscles of the thorax which alter the volume, and therefore the pressure, inside the lungs relative to the atmospheric pressure outside the body. To inhale, the diaphragm and intercostal muscles between the ribs contract, causing the diaphragm to move down into the abdomen and the ribs to move upwards and outwards. This motion increases the volume of the thoracic cavity, causing a decrease in air pressure inside the lungs. In response to this pressure change, air from outside the body flows in through the mouth and/or nose, through the conducting airways and diffuses into the respiratory zone of the lungs. This process is shown in Figure 1-2 below. Oxygen is thus delivered to the respiratory zone, increasing the concentration of oxygen in the alveoli. The blood passing outside the alveoli has a low concentration of oxygen, therefore oxygen passes by diffusion across the airway wall and capillary wall into the blood where it binds to hemoglobin. This diffusion occurs quickly, in approximately 0.25 seconds[6].

While oxygen is diffusing into the bloodstream, carbon dioxide is diffusing from the blood across the blood vessel and alveolar walls into the alveoli because of the low concentration of carbon dioxide in the alveoli. Passive exhalation is achieved by simply relaxing the diaphragm and intercostal muscles, so the diaphragm moves up into the thorax and the ribs move inward and down. This motion is driven by the elastic recoil in the lung structure itself, which relaxes inward when an external force is not acting to expand it[6]. As the volume in the thoracic cavity decreases, the pressure increases and air flows from the alveoli through the conducting airways and out through the mouth and/or nose.

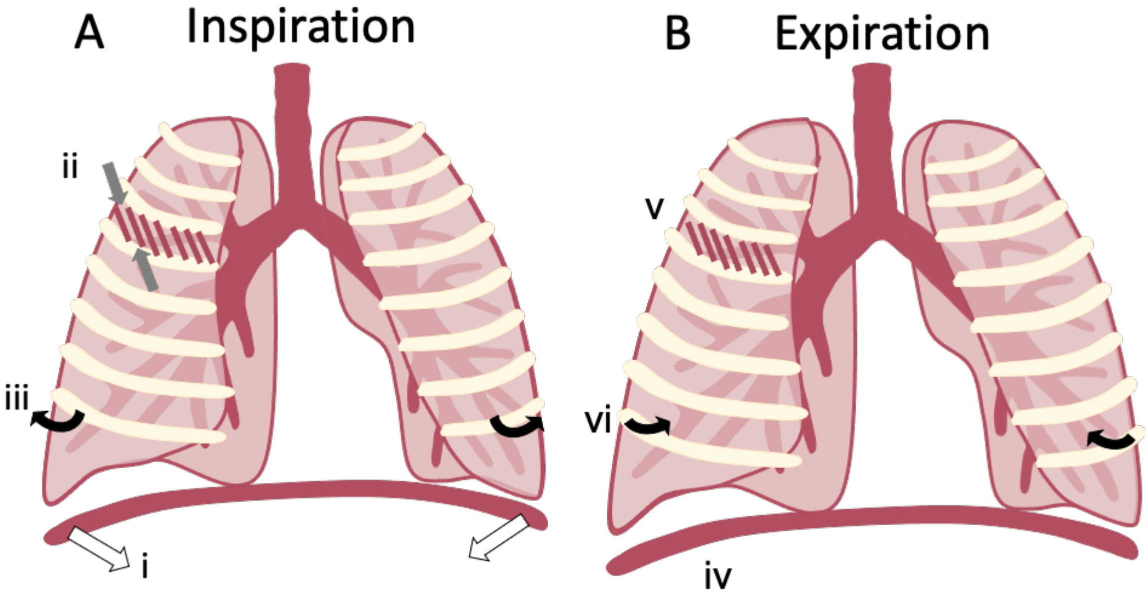

Figure 1-2 The biomechanical process of breathing.
This figure illustrates the mechanical process behind normal breathing. A. At inspiration, (i) the diaphragm contracts and moves down while (ii) the intercostal muscles contract, (iii) moving the ribs upwards and outwards. This expands the volume of the thoracic cavity, decreasing pressure, causing air to flow inward. B. At passive expiration, the (iv) diaphragm and (v) intercostal muscles relax, and the elastic recoil of the lungs causes them to contract, (vi) pulling the ribs downwards and inwards. This increases pressure in the thoracic cavity, causing air to flow outward. Adapted from Young *et al*[8].

1.3 Non-Small Cell Lung Cancer

As stated in Section 1.1, lung cancer is the leading cause of cancer death in Canada[2]. One in three patients with non-small cell lung cancer (NSCLC) will undergo radiation therapy as part of their course of treatment and delivering safe and effective radiation therapy to the thorax continues to be a challenge. This section and the one following will review the disease and the types of treatment used, including radiation therapy.

1.3.1 The Disease

There are three types of NSCLC: adenocarcinoma, squamous cell carcinoma, and large cell carcinoma[9]. Adenocarcinoma is the most diagnosed form of lung cancer, making up approximately 40% of all lung cancers. It develops primarily in the periphery of the lungs. Squamous cell carcinoma is the next most common, representing about 20% of lung cancers. This type of tumour is mainly found in the central lung. Large cell cancers make up about 10% of lung cancers and will not be discussed in detail here. Small cell lung cancer will also not be discussed.

Lung cancer is assigned a stage from I to IV based on the size of the lung tumour and the spread of the cancer in the lungs, lymph nodes, and outside the thorax. Stage I or II cancer is a tumour of less than 7cm (in most sub-stages, less than 5cm) and is spread only to lymph nodes near the bronchi[10,11]. At this early stage, patients will receive surgery if they are medically eligible, and will likely not receive any radiation therapy. If a patient at this stage is not able to undergo surgery, they will receive radiation therapy, with most patients receiving stereotactic ablative body radiotherapy (SABR) unless the tumour is not in a suitable location[9].

If lung cancer has spread to another lobe of the lung, or into further lymph nodes, it may be classified as stage III[10,11] and is commonly referred to as locally advanced NSCLC. At this stage, nearly all patients will undergo radiation. If the cancer has metastasized to other regions of the body, it is classified as stage IV, which will not be discussed in detail here.

1.3.2 Treatment of Locally Advanced NSCLC

Most patients diagnosed with stage III NSCLC will undergo radiation therapy as part of their treatment, which may also include surgery, chemotherapy and/or immunotherapy[9,12]. This patient population is very heterogeneous, because the primary tumour or nodal involvement can vary widely within stage III NSCLC. As a result, many types of treatment may be considered, and the treatment used often depends on the patient's health status or how the patient is expected to tolerate a treatment. The treatment options include radiation therapy, chemotherapy, immunotherapy, or surgery, any of which may be used alone or in combination with other treatments[9].

The most common treatment for stage III NSCLC patients who are not good candidates for surgery is a combination of chemotherapy and radiation therapy[9], and immunotherapy is being used more frequently in this group. While this thesis is focused on imaging for use in radiation therapy, it is important to consider the other treatments patients will undergo. While this combination of treatments has been shown to be the most effective for these patients[13,14], it also increases the risk of side effects such as radiation pneumonitis as compared to single-modality treatment[3].

1.4 Radiation Therapy Planning and Delivery

Radiation therapy for NSCLC is delivered using high energy x-rays delivered by a linear accelerator. The patient lies on a treatment bed, and the linear accelerator rotates around the patient to deliver radiation from multiple angles around the body. This allows the dose to the skin and healthy tissues to be kept low, while the beams overlap on the tumour and add up to deliver a large dose where it is needed. This section of the thesis will outline the process by which a NSCLC patient's radiation treatment is planned and delivered.

1.4.1 CT Simulation

In Canada, all patients who will undergo radiation therapy for NSCLC undergo 4D-CT scanning which is used to simulate radiation treatment delivery[12]. The process by which the 4D-CT is acquired is detailed in Section 1.7.1. The 4D-CT dataset is assessed to determine the magnitude of tumour motion, which informs the medical physicist and radiation oncologist on what (if any) motion management techniques are needed when treating the patient[15]. These techniques are discussed in greater detail in Section 1.5.1. If a free-breathing method is used, the 4D-CT scan will be appropriate for treatment planning. Otherwise, additional imaging must be acquired so treatment planning is performed using imaging that reflects the equipment, patient positioning, and breathing maneuver (ex. deep-inspiration breath hold) that will be used during treatment delivery.

After the imaging is acquired, the tumour and all surrounding organs at risk (OARs) are contoured on the CT dataset that simulates the patient positioning and breathing maneuver that will be used during treatment. An average CT dataset composed of all phases of the

4D-CT to represent the full range of respiratory motion may be used, or the phase during which treatment will be delivered if respiratory-gated or breath-hold delivery is going to be used. These contours are used to define the exact size, shape, and location of the tumour and organs for the treatment planning system. The accuracy of these contours is therefore highly consequential for treatment accuracy, and 4D-CT motion artifacts are known to affect these contours[16–18]. The causes of 4D-CT artifacts and their consequences are further discussed in Section 1.7.3.

1.4.2 Treatment Planning

Once all contouring is complete, the 4D-CT and radiation dose prescription are passed to a dosimetrist, who uses treatment planning software to plan exactly how the radiation dose will be delivered from the linear accelerator. The treatment planning system uses the 4D-CT to simulate how the radiation dose will be transmitted through and absorbed by the body. The dosimetrist uses this information to ensure that the contour of the tumour receives a sufficiently high dose, while the contours of all OARs receive a sufficiently low dose[19]. For patients with advanced stage NSCLC, the standard dose to the planning target volume (PTV) is 60 Gy, delivered in 30 daily fractions of 2 Gy each[20].

The two most common delivery geometries are intensity modulated radiation therapy (IMRT)[21] and volumetrically modulated arc therapy (VMAT)[22]. IMRT is a 3-dimensional treatment planning technique that entails delivering radiation from several static angles around the patient, using beams which overlap over the tumour to create a region of high dose. In IMRT, the beams used are non-uniform in order to optimize the dose distribution[21]. This is accomplished using a multi-leaf collimator (MLC), which is made up of narrow tungsten leaves which are individually positioned to shape the radiation field. A non-uniform distribution is achieved from a combination of static fields with different geometry, or from moving the MLC to modulate the dose distribution while the beam is delivered. In VMAT, the treatment gantry rotates constantly around the patient, while delivering a continuous radiation beam. This beam is constantly modulated in intensity and in shape, as are the dose rate and the rotation speed of the gantry, allowing for even greater optimization of the dose distribution[22]. The two geometries are shown below in Figure 1-3.

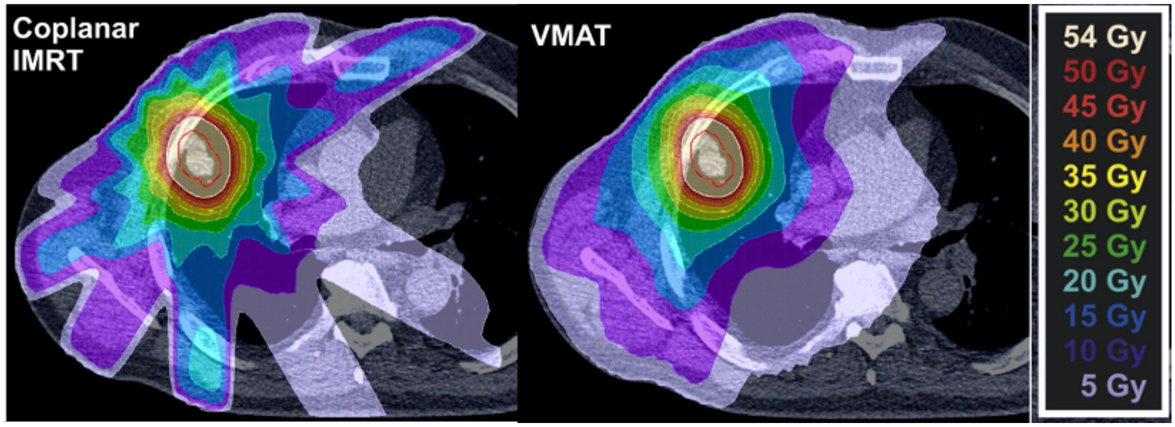

Figure 1-3 Typical dose distribution of external-beam radiation therapy.
An example of two possible dose distributions for NSCLC treatment. The IMRT plan (left) shows the distribution of dose from several static beams delivered at set angles around the patient. The VMAT plan (right) shows the distribution from a delivery which is varied while the gantry rotates constantly around the patient. Adapted from Holt *et al*. with permission[23].

1.4.3 Radiation Treatment Delivery

The patient is treated lying in the same position as they were for the 4D-CT scan, usually supine with their arms raised above their head. If the planned treatment does not encompass the motion of the tumour due to respiration, then a respiratory motion management strategy, discussed in Section 1.4.1, will be used[15].

When the patient is set up in the treatment position, imaging may be used before treatment to verify that the setup is accurate, and that the tumour is in the correct position. This is accomplished using the kV x-ray imaging system that is present on most modern linear accelerators. A pair of planar images are acquired and compared to the treatment planning CT to ensure that the patient is aligned properly. More recently, daily cone-beam computed tomography (CBCT) has been used for more accurate patient setup prior to treatment[24,25]. Optical surface tracking is a new technology which enables position verification without the use of ionizing radiation, and may be used before CBCT instead of planar kV imaging[26]. In addition, imaging performed during treatment delivery can track respiratory motion to enable respiratory motion management techniques, described in Section 1.5.1[24].

During radiation therapy delivery, as the x-rays pass through the body, some will interact with the tissue. The most common type of interaction at this x-ray energy and material type is Compton Scattering[27]. Through this method, some of the energy from the x-ray is deposited into the tissue and releases an energetic electron. The scattered x-ray may go on to interact with other atoms in the body, and the electron will interact with nearby atoms, depositing its energy. This process is continually repeated as treatment is delivered, and this physical and chemical process will result in broken bonds within molecules, which may lead to biological damage (damage to cells or to cell DNA). Using the distribution of dose during delivery and the fraction of doses over a number of days, the dose is delivered with the intention of inflicting the maximum possible damage on the tumour and the minimum possible damage on the surrounding healthy tissues and OARs[27].

1.5 Challenges in Radiation Therapy for NSCLC

Each disease site has challenges when planning and delivering radiation therapy, including NSCLC. For this disease, two of the largest ongoing challenges are related to respiratory motion and radiation-induced lung injury. This section of the thesis will explain the current methods used to address these factors, and the unmet needs in this area.

1.5.1 Respiratory Motion Management

Treating NSCLC is inherently challenging due to respiratory motion, because radiation therapy must be spatially accurate and internal organ and tumour motion during regular breathing has a highly variable trajectory across patients[28]. Treatments are usually more than one minute of beam-on delivery time, so patients cannot hold their breath for the entire delivery. Therefore, the motion of the target and the surrounding organs at risk must be well understood, and this motion must be controlled or accounted for during radiation delivery. Respiratory motion management is applied when the motion of the target exceeds 5 mm[15]. The available technology and recommendations for use are outlined in the report of AAPM Task Group 76 on the management of respiratory motion in radiation oncology[15].

Motion management techniques include motion encompassment, breath-hold, tumour immobilization, respiratory gating, and dynamic tumour tracking[12,15]. Motion encompassment is a method in which the gross tumour volume (GTV) is contoured on all phases of the 4D-CT and the internal target volume (ITV), the union of all GTVs, is created. In this way, the treatment volume is expanded to include some healthy tissue but ensures that the tumour is always within the treatment field. Treatment is delivered while the patient breathes freely. In breath-hold methods, the patient takes a deep breath and holds it for 10-20 seconds at a time, which is verified using imaging or air-flow measurements. During the breath hold, the tumour is stationary and treatment is delivered[29,30]. Tumour motion can be minimized using abdominal compression, which forces shallow breathing by restricting diaphragm motion. This technique is most often used for lower lobe tumours which are closer to the diaphragm[31,32]. Respiratory gating is a free-breathing technique in which imaging is used to track the patient's breathing motion and enable treatment delivery only in a certain window of the respiratory cycle (often during end-exhale)[33,34]. Motion may be tracked using kV x-ray imaging, ultrasound, or optical tracking methods. This method is comfortable for patients and spares healthy tissue surrounding the tumour but requires a longer delivery time due to the pauses in delivery during every respiratory cycle, and relies on the assumption that internal and external motion are highly correlated. It also requires that the patient breathes in a consistent and reproducible manner, which is not always possible for patients with poor pulmonary function. The last method, dynamic tumour tracking, is a novel method which is not yet widely used. This is also a free-breathing method, where the radiation beam is modified in real time during delivery to follow the measured or assumed motion of the tumour. This method enables minimal dose to surrounding tissues, and more efficient delivery than respiratory gating, but has significantly greater technical requirements.

1.5.2 Radiation Induced Lung Injury

Some damage to healthy tissues and organs is inevitable when a patient receives radiation therapy. The radiation delivered to the tumour will pass through healthy tissue before and after reaching the tumour itself, causing damage along the path. When cellular damage is detected in the body, an inflammatory response is triggered which may lead to symptomatic radiation-induced lung injury. The severity of this radiation-induced lung injury (RILI) is graded according to Table 1-1 below[35–37].

Table 1-1 Severity grading of radiation-induced lung injury

Grade	RTOG	CTCAE v. 5.0
0	No changes	No changes
1	Asymptomatic or mild symptoms	Asymptomatic, only radiological, or tomographic findings
2	Moderate symptoms of pneumonitis (severe cough) and radiographic changes (radiographic patches)	Symptomatic, does not interfere with daily activities
3	Severe symptoms of pneumonitis, dense radiographic changes	Symptomatic, interferes with daily activities, requires supplemental O_2
4	Symptoms of severe respiratory failure requiring assisted ventilation or continuous O_2	Threatens life, requires mechanical ventilation support
5	Death-related late effects of radiotherapy	Death related severe pneumonitis

The lungs are highly sensitive to radiation, and care is taken to minimize the dose to the healthy lung when treating NSCLC. In spite of this, approximately 30% of patients who undergo treatment for NSCLC will experience RILI[3]. This injury is typically broken down into an early (inflammatory) toxicity and a late (fibrotic) toxicity[37]. The injury process is illustrated in Figure 1-4 below. In the early stage, increased inflammation begins within days. Approximately 3-12 weeks after radiation exposure, epithelial and endothelial cell degradation leads to alveolar collapse[37]. This inflammatory cascade will reach the fibrotic phase 6 months or more after radiation therapy. In this late stage myofibroblasts and collagen deposits are present, thickening the alveolar wall and reducing lung function[37].

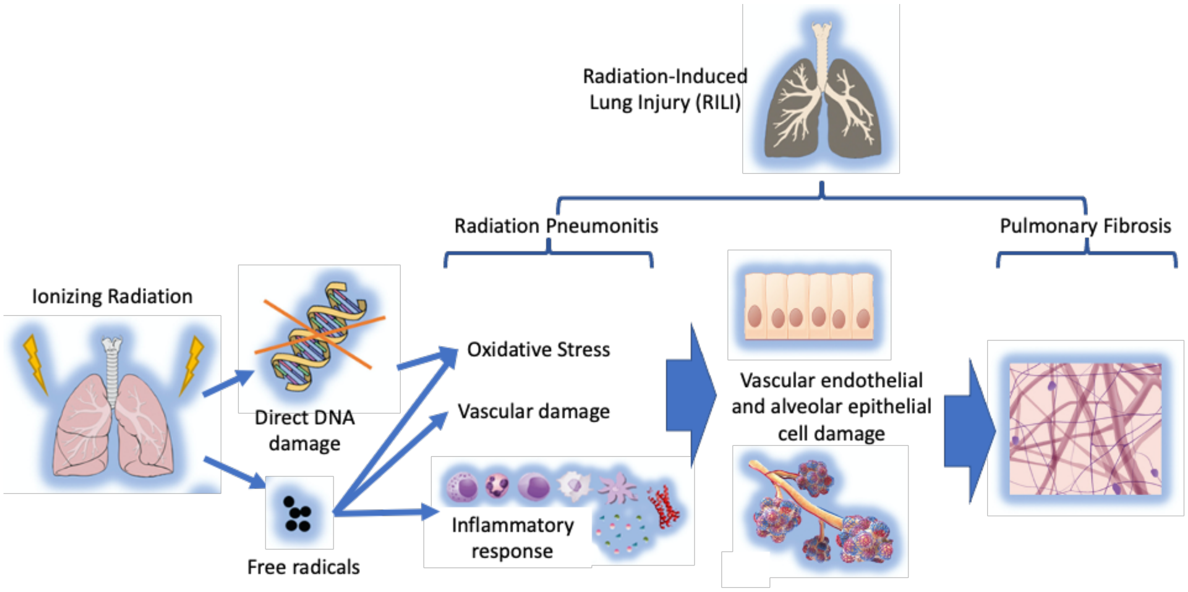

Figure 1-4 Radiation induced lung injury process.
This figure illustrates a simplified pathway by which radiation exposure leads to radiation pneumonitis and potentially permanent fibrosis. Ionizing radiation causes direct DNA damage, and the production of free radicals. These lead to oxidative stress and vascular damage, triggering a local inflammatory response. At this stage, radiation pneumonitis may occur. This process may cause damage to vascular and alveolar cells, and the late inflammatory stage leads to the development of fibrotic tissue, which may cause permanent fibrosis. Adapted from Hanania *et al*[38]. with permission.

The lungs are a parallel organ, which means the function of one region of the organ is generally not dependent on the function of another region. For this reason, a high dose to a small volume of the lung may not result in clinically significant damage, as the remainder of the organ is functioning well enough to compensate for the small damaged region. However, dose to a large volume of the lungs may significantly reduce their overall function[39].

The volume of lung tissue receiving over 20Gy is a known predictor of severe pneumonitis[3,40]. Therefore, in clinical practice, the volume of healthy lung tissue that is irradiated is minimized. However, in current clinical practice all lung tissue is weighted equally and the functional heterogeneity common in patients with NSCLC is not considered. One method which has been explored to reduce the clinical impact of radiation pneumonitis is to include functional lung imaging in the treatment planning process[41,42]. The assumption underlying this technique is that many patients who develop NSCLC have respiratory co-morbidities such as COPD from a history of smoking or environmental exposures, leading to heterogeneous function throughout the lungs. If the highly functioning regions of the patient's lungs are preferentially spared, it may reduce the risk of symptomatic pneumonitis. Functional lung imaging, including ventilation and perfusion imaging discussed in Sections 1.9 and 1.10 respectively, may be used to spatially map function in the lungs, to indicate regions to be prioritized for dose reduction in treatment planning. While there is not yet a consensus on the methods that are best suited to mapping ventilation and defining avoidance regions, early clinical trial evidence supports the hypothesis that this approach can significantly reduce toxicity[43].

This thesis focuses on the potential applications of volumetric computed tomography (explained in Section 1.6 below) in 4D-CT imaging for treatment planning, and for imaging lung function. These applications may be impactful in both research and clinical practice. First computed tomography and 4-dimensional computed tomography will be discussed, followed by the methods and applications of ventilation and perfusion imaging.

1.6 Computed Tomography

Computed tomography imaging was developed 50 years ago to create 3-dimensional images of a patient's body based on x-ray attenuation, which reflects tissue density[44]. The techniques used to acquire and reconstruct these images have evolved since then but have been largely consistent in the past few decades. This section will review the current methods used to create CT images, including the strengths and weaknesses of current methods.

The technological approach used to acquire CT images has evolved dramatically in the 50 years since its first use. Figure 1-5 below shows how CT scanner configuration has evolved. In first generation scanners, the x-ray tube and a single detector translated linearly to create a projection image from parallel beams. The system rotated around the patient, collecting a series of these parallel beam projections. Second generation scanners used the same translate-rotate geometry, but a small array of detectors was used so the x-rays were emitted in a fan beam. These were quickly replaced by third generation detectors, which used a rotating fan beam source, and a larger rotating curved array of detectors positioned opposite to the source.

Finally, multi-slice detector arrays were introduced so that multiple axial slices could be imaged in a single rotation. The x-rays are now projected in a narrow cone-beam geometry, with the fan angle and cone angle used to define the size of the beam, which determine the field-of-view (FOV) and axial field-of-view (aFOV) respectively[45]. The cone angle used in these scanners has been gradually widening, as methods to reconstruct images without cone-beam artifacts (discussed in Section 1.6.4) improve. From approximately 1998 to 2008, the number of detector rows increased by a factor of four every two to three years[46]. The widest arrays currently used have 256-320 detector rows, providing an aFOV of 160 mm. The adoption of these scanners in radiation oncology has been slow, in part due to the increased cost of these scanners as compared to 32 or 64 detector row models. However, they provide many advantages in radiation therapy, as will be discussed in detail in Section 1.8.

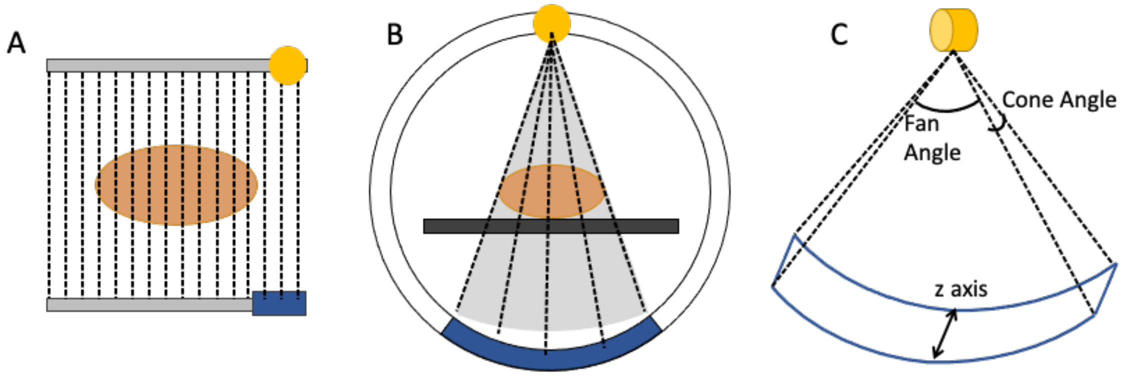

Figure 1-5 The evolution of CT scanner configurations.
A. The parallel beam projection method from 1st generation scanners. B. The rotate-rotate fan-beam projection geometry used in 3rd generation scanners. C. The narrow cone-beam and multi-detector array geometry used in multidetector CT scanners, and advanced in volumetric (or area detector) CT scanners. Adapted from Bushberg *et al*[45].

1.6.1 CT Image Acquisition and Reconstruction

To acquire a CT image, x-rays are emitted in a fan geometry from one side of the scanner bore and pass through the patient who is lying on the couch inside the bore. Some of the x-rays are attenuated as they pass through the patient's body, with the degree of attenuation depending on the thickness and electron density of the tissue in the beam path. The remaining x-rays reach a set of detectors located on the side of the bore opposite the x-ray source. The entire system rotates on a gantry around the bore, collecting projection images from multiple angles around the patient's body. This geometry is shown in Figure 1-6. The fan beam only passes through a narrow slice of the patient's body, so the couch moves the patient incrementally through the imaging bore so the process may be repeated along the length of the region being imaged[45].

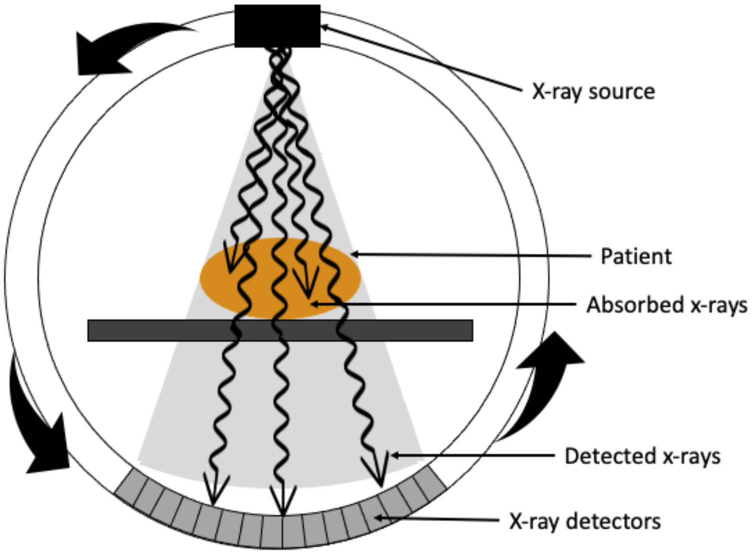

Figure 1-6 CT acquisition.

X-rays pass from the source in a fan beam or narrow cone beam geometry through the patient. The x-rays are attenuated proportionally to the electron density and thickness of the tissue they are passing through, and the remaining x-rays are detected by the array of detectors on the other side of the scanner. The entire scanner rotates around the patient's body, collecting projection images.

The many projection images must now be reconstructed to create a cross-sectional image through the patient's body. There are two categories of reconstruction; filtered back-projection and iterative reconstruction. Filtered back-projection was long the dominant method used, but iterative methods have been increasing in use as computing power has advanced. In this thesis, computed tomography images were all reconstructed using filtered back-projection, but images generated by iterative reconstruction may also be used in the future.

The final 3-dimensional CT image of a patient is given in Hounsfield Units (HU)[44], which is defined in Equation 1-1 below.

Equation 1-1

$$Hounsfield\ Unit = \left(\frac{\mu_{tissue} - \mu_{water}}{\mu_{water}}\right) \times 1000\ [HU]$$

In the equation above, μ_{tissue} and μ_{water} are the linear attenuation coefficients of tissue and water, respectively. CT number, measured in Hounsfield Units (HU), is unitless, but can be converted to a measure of electron density using a scanner-specific calibration curve. CT imaging is used in planning of radiation therapy because this 3-D map of electron density is used to estimate the deposition of dose from an electron or x-ray beam delivered for therapy. CT images are used to generate treatment plans according to the desired distribution of dose as described in Section 1.4.2.

1.6.2 Imaging Artifacts

An imaging artifact is any effect which results in inaccuracy in some or all of an image. These may be caused by patient motion, hardware or software limitations, or inaccurate assumptions underlying image generation. These artifacts may be visually obvious and may or may not be easily quantifiable. In this section, the many potential artifacts in CT imaging for radiation oncology applications will be discussed, as well as current methods and opportunities to reduce or eliminate them for optimal imaging accuracy.

Common artifacts in CT acquired for treatment planning are beam hardening and streak artifacts, which both occur when imaging high density materials such as bone or medical implants. These artifacts are illustrated in Figure 1-7 below. Beam hardening artifacts occur when the assumption of an effective linear attenuation coefficient is broken. The x-ray beam used in CT contains photons in a range of energies, and an effective linear attenuation coefficient is used in image reconstruction. However, if the beam passes through thick bone or other high-density material, low energy x-rays are preferentially attenuated, and the beam is harder (has a higher average energy). The ray passes through the tissue behind this dense material with lower attenuation than expected, and this tissue is therefore assigned a lower attenuation value. It appears as a dark region or streak in the final image[45]. Streak artifacts occur when a material, such as a dental filling, has such high density that it exceeds the range of the detectors. Therefore, in each projection it appears that the object is larger than it actually is, because so many x-rays were attenuated. When the final image is reconstructed, the object casts bright streaks around it, obscuring the surrounding structures[45].

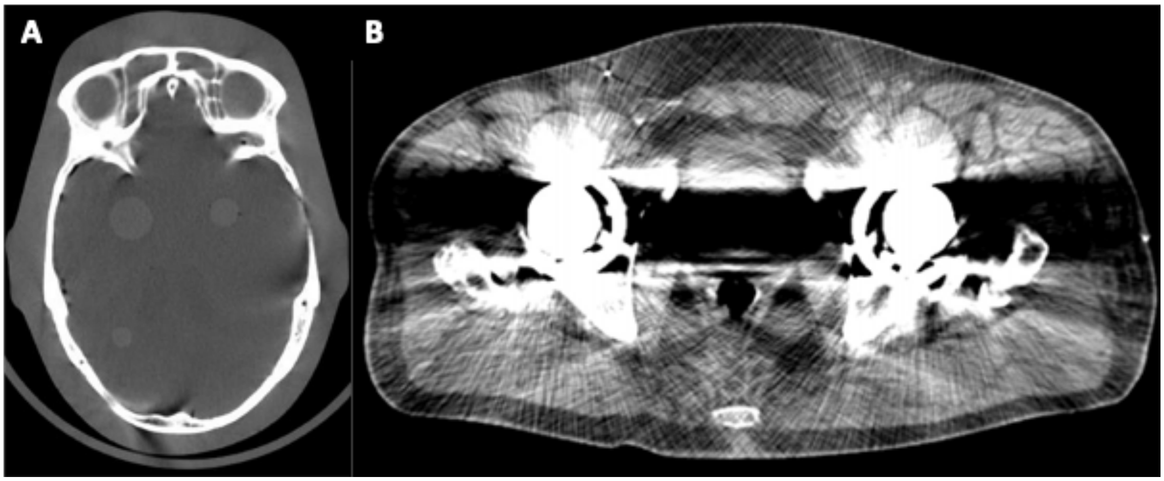

Figure 1-7 Example images of CT artifacts.
Example images illustrating (A) streaking artifact from cone beam image (B) a severe streaking and beam hardening artifacts caused by dual hip prostheses. Adapted from Tang *et al*[47]. and Axente *et al*[48].

When a narrow cone beam or full cone beam are used, cone beam artifacts may occur. These are a result of under-sampling in the direction of the cone angle (usually denoted as the z-direction), particularly for detectors at the edge of the cone[49]. These artifacts appear as streaking or stair-step artifacts if there is a high-contrast edge along that direction[45,50]. An example image is shown in Figure 1-7 above. Hardware solutions such as anti-scatter grids and advanced reconstruction techniques have enabled companies to produce volumetric CT scanners with a wide enough cone angle to enable 160 mm axial field-of-view with minimal cone artifacts in the resulting images[50]. These scanners are discussed in detail in Section 1.8.

1.7 4-Dimensional Computed Tomography

4-dimensional computed tomography (4D-CT) is a technique that was developed in response to a need to better capture and account for the respiratory motion of lung tumours during treatment planning and delivery. The technique used to generate 4D-CT was developed in the early 2000s, with the first paper using an external signal of respiratory motion published in 2002[51]. Several other papers were published shortly after this, taking advantage of multi-slice (4-slice or 8-slice) CT scanners using cine mode acquisition[52], and 16-slice scanner with helical acquisition[53].

These early studies lay the groundwork for the currently used 4D-CT protocol, which is often acquired with a helical acquisition on a multi-slice CT scanner with an external motion tracking system, as described below. 4D-CT is currently the standard of care for many patients receiving radiation therapy for sites in the liver and lungs, which are heavily influenced by respiratory motion. In these sites, tissue has been shown to move up to 20mm during free breathing[54,55]. To plan and deliver radiation accurately to the target and minimize dose to the surrounding tissues, this motion must be understood and accounted for. 4D-CT enables several different methods to account for motion: first, target contours can be drawn to encompass the full range of motion of the target such that surrounding healthy tissue receives an increased radiation dose, but the target is not under-dosed. Alternatively, a plan may be generated on a single phase of the respiratory cycle, usually end-exhale as it is the longest lasting and most stable of the phases. This requires measurement of the respiratory motion during delivery and gating the treatment beam on only when the tumour is thought to be in the correct location.

1.7.1 4D-CT Acquisition

There are two main categories of 4D-CT acquisition, axial and helical. In an axial acquisition, the patient breathes freely lying supine on the CT couch in the treatment position. A series of images are acquired in a static position, so the entire breathing cycle has been imaged. Image acquisition is then briefly paused while the couch shifts, to image the next volume. This process is repeated until the entire volume of interest has been scanned. In a helical acquisition, images are continuously acquired as the patient breathes freely. During the acquisition, the couch moves slowly forward into the bore as the x-ray source and detector rotate, creating the helical pattern of data acquisition. The pitch of the couch (the speed at which the couch moves forward) is calculated by the width of the aFOV and the patient's respiratory rate to ensure that each anatomical slice is imaged for an entire respiratory cycle before passing out of the field of view of the scanner[53]. This process is shown in Figure 1-8 below. During the acquisition, the patient's respiratory motion is monitored using an external motion tracker such as an infrared camera and reflecting block, respiratory bellows, or a whole-body infrared camera system. This external motion is used to identify what phase or amplitude of the breathing cycle the patient is in at that moment in time.

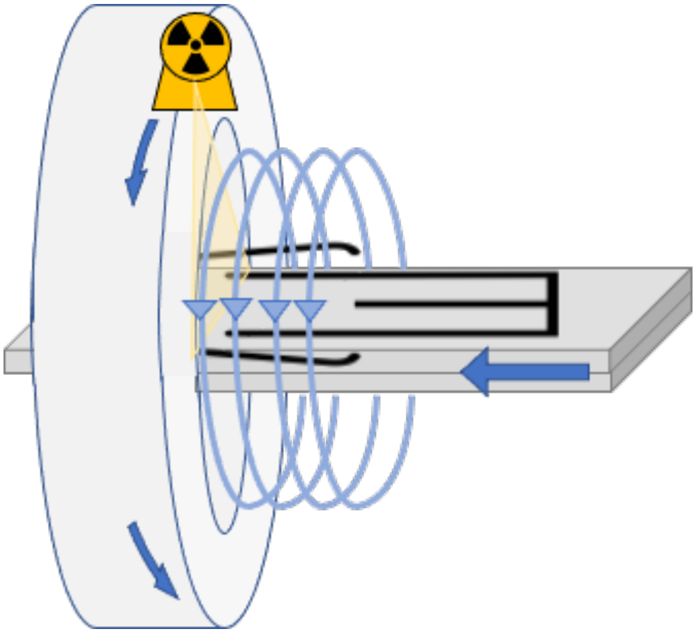

Figure 1-8 4D-CT acquisition
The schematic above illustrates how helical 4D-CT images are acquired. The patient lies supine on the CT couch and breathes freely while the couch slowly moves through the scanner bore. The x-ray source and detector are constantly rotating around the patient, so image data is collected in a helical pattern and each slice location is imaged through an entire respiratory cycle.

This method is used under a set of assumptions which may not always be satisfied. The first of these is that patient breathing motion is stable and at a consistent amplitude and frequency throughout the duration of the scan. The second is that the external motion of the patient's chest or stomach accurately reflects the internal motion of the diaphragm and lungs in both phase and amplitude. Studies of the correlation of internal and external respiratory motion suggest that they are usually highly correlated, but there is sometimes a phase delay between internal and external motion[56–59]. Coaching the patient as they breathe can improve this correlation, but takes longer to implement and therefore may reduce patient throughput[60].

1.7.2 4D-CT Reconstruction

After the scan is complete, there is a large set of CT projections from the helical acquisition, which are all tagged with an exact location along the z-axis and the precise time of acquisition. This time is compared to the external motion tracking data to determine what phase of the respiratory cycle each projection belongs to. Then, the projections are all sorted such that for every phase in the respiratory cycle, there are sufficient projections at every slice location to create a full 3D volume. If there are insufficient projections for a particular slice and phase, data from the closest possible phase may be used to fill in the missing data and complete the image as accurately as possible.

There are two main categories of 4D-CT reconstruction: phase-based and amplitude-based. In phase-based reconstruction, all end-inhale points of the respiratory curve are identified, and the data points in between each end-inhale point are equally divided into 8-10 respiratory phases. This method relies on the assumption that (relative to the total length of the breathing cycle) the time taken from inhale to exhale and back to inhale is the same every time. In amplitude-based reconstruction, specific positions (amplitudes) of the external motion are identified to represent the end-inhale and end-exhale positions. Then the distance between the two positions is divided into 5 segments, for a total of 10 positions from end-inhale to end-exhale. This process is depicted in Figure 1-9 below.

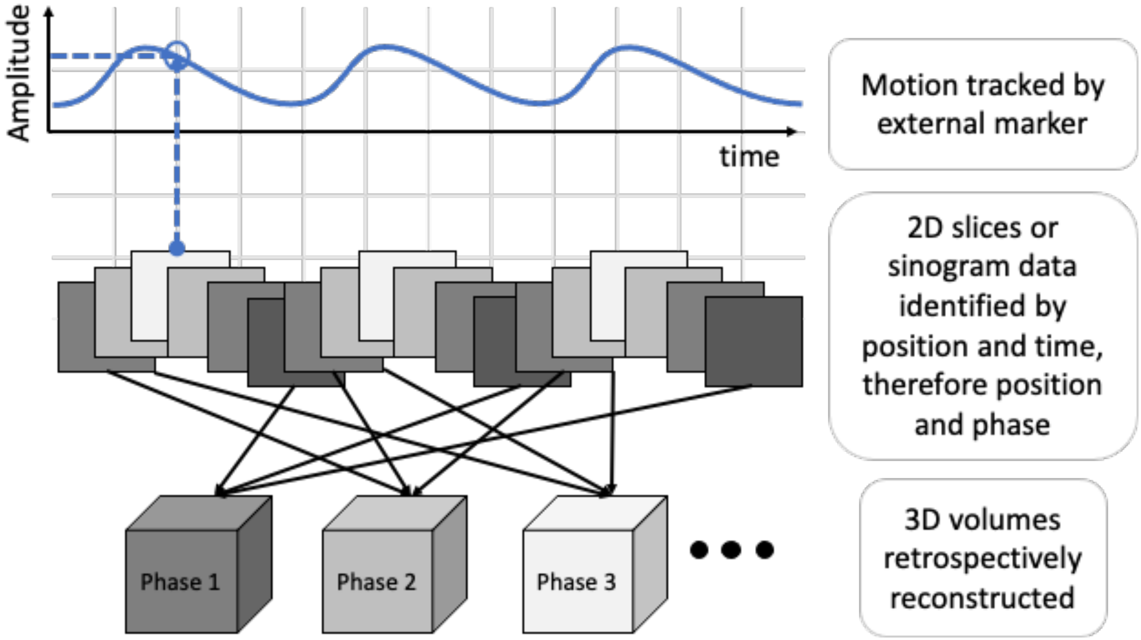

Figure 1-9 4D-CT Reconstruction.
The above schematic illustrates how 4D-CT images are reconstructed. The blue breathing trace at the top of the image represents the respiratory data collected from an external monitor. The images or sinogram data have a location and time, which correspond to a location and phase of the respiratory cycle. Using these two parameters, the images or sinogram data are sorted into 8-10 "bins" representing each phase of the respiratory cycle so an entire 3D image may be reconstructed at each phase.

1.7.3 4D-CT Motion Artifacts: Causes and Types

As detailed above, there are two key assumptions made when acquiring and reconstructing 4D-CT images. In particular, the assumption that the patient's breathing will remain stable and consistent in amplitude and frequency throughout the scan is often not held true. Many patients undergoing 4D-CT simulation are nervous and are not able to relax into their resting breathing pattern until partway through the one- to two-minute scan. In addition, many of these patients experience breathing difficulties due to their lung cancer or co-morbid conditions such as COPD, resulting in an inconsistent respiratory motion trace through the scan.

There are three common patterns of irregular respiration data: incomplete sampling, baseline drift, and irregular amplitude. The first refers to the case where the frequency of the patient's breathing decreases as they relax after the start of the scan. The patient's respiratory rate is used to determine acquisition parameters such as the couch pitch in a helical scan. If breathing rate decreases, then a slice will not be imaged for the entire respiratory cycle before it moves out of the FOV of the scanner. With this incomplete data, projections from the nearest possible slice and respiratory phase will have to be used to complete the image, resulting in a loss of accuracy. The other two types of irregular motion refer to mostly to changes in amplitude. In a baseline drift condition, the amplitude and frequency of a patient's breathing is largely unchanged, but the entire respiratory curve shifts due to patient movement or a change from shallow to deeper breathing with relaxation. In this case, it can be difficult or impossible to correctly match images taken at the beginning of the scan to images from the same phase later in the scan. One slice in an image may not really be from the same respiratory condition as another slice in the image, so the depicted anatomy is not entirely correct. Lastly, in the irregular amplitude condition the patient breathes erratically, taking some deep and some shallow breaths. This may affect both amplitude and frequency of breaths, and as above, makes it difficult or impossible for the reconstruction algorithm to accurately sort all images correctly by phase or amplitude. In previous research, phase-based binning often leads to more motion artifacts in the final 4D-CT images than amplitude-based binning, but both techniques are used clinically.

The artifacts which result from these irregular breathing patterns vary widely in appearance and severity. However, they can be classified into four artifact types which are easily visually identified[61]. Example images of these artifacts are shown in Figure 1-10.

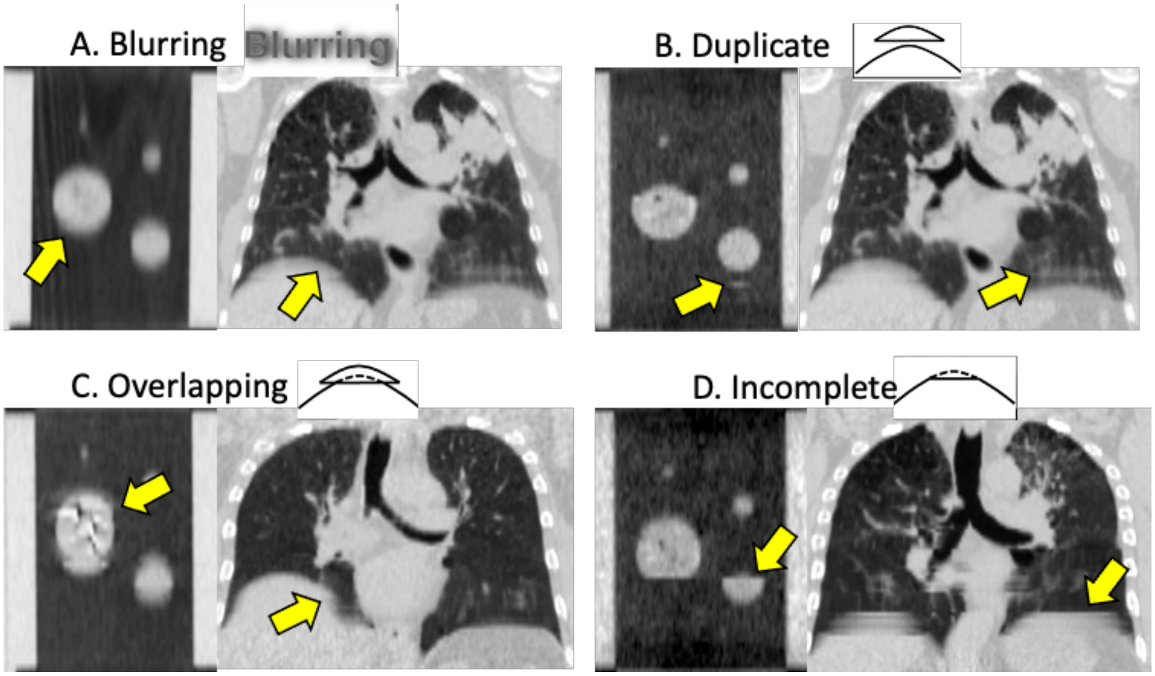

Figure 1-10 Types of 4D-CT motion artifacts.
Four types of motion artifacts are shown in examples from a Quasar Respiratory Motion Phantom and from the treatment planning 4D-CTs of three patients with NSCLC. Each artifact is highlighted with a yellow arrow. Adapted from Yamamoto *et al*[61].

The impacts of 4D-CT motion artifacts in radiation therapy can be significant. Studies have shown that these artifacts can lead to inaccurate GTV contours[16,62], which may result in under-dosing the target or over-dosing surrounding healthy tissue. In addition, these artifacts can lead to inaccurate contouring of surrounding organs at risk, which may again result in the delivered dose not matching the intention of the treatment plan. This has been proven to affect patient outcomes, with a 2020 study showing that in patients with liver cancer, the presence of 4D-CT motion artifacts was associated with reduced local control of the disease[63].

Efforts have been made to reduce motion artifacts, addressing the problem from different aspects of the imaging process. One approach has been to improve the image sorting and reconstruction process[64,65]. This approach generally requires an increased imaging dose to acquire additional data to compensate for irregular breathing motion. Other methods include coaching, where digital tools are used to assist patients in breathing at a consistent pace and amplitude for the duration of the scan[66]. These methods generally require an increased appointment time as the patients must be taught how to use the coaching device and get comfortable using it.

1.8 Volumetric Computed Tomography

Until recently, CT scanners collected data in a fan-beam geometry to prevent unacceptable scattering artifacts produced from using a cone-beam geometry (these are explained in Section 1.6.2). When a cone-shaped beam is used there is increased scatter, and increased variation in beam intensity and energy received at the detector. These factors must all be accounted for in vCT scanners to minimize cone-beam artifacts in the reconstructed images. In early iterations of this technology, these cone-beam effects were shown to degrade image quality as compared to a conventional narrow-aFOV CT scanner[67]. Throughout the following decade, methods used to reduce these artifacts generally fell into two categories; hardware designed to reject scattered photons at the detector, and software designed to compensate for the presence of remaining scattered photons during image reconstruction. Using one or both techniques, CT manufacturers are now able to use "wide fan" geometries, which approach a cone beam, and reconstruct images with acceptable image quality for radiology.

1.8.1 Volumetric CT Scanners

Currently, these scanners are capable of imaging a volume with an axial field-of-view (aFOV) of 16.0 cm, and an in-plane field-of-view (FOV) of 50.0 cm. These scanners are called volumetric scanners (because a larger volume is imaged in a single rotation) or area detector scanners (because to capture this wide fan beam, the detectors used are much wider, i.e. 256-312 detectors as compared to 32-64 detectors). This difference in scanner geometry is shown in Figure 1-9 below. These scanners can capture large volumes very quickly, which is advantageous when one is imaging a moving part of the body or wants to collect a dynamic image series across a large volume with high temporal resolution.

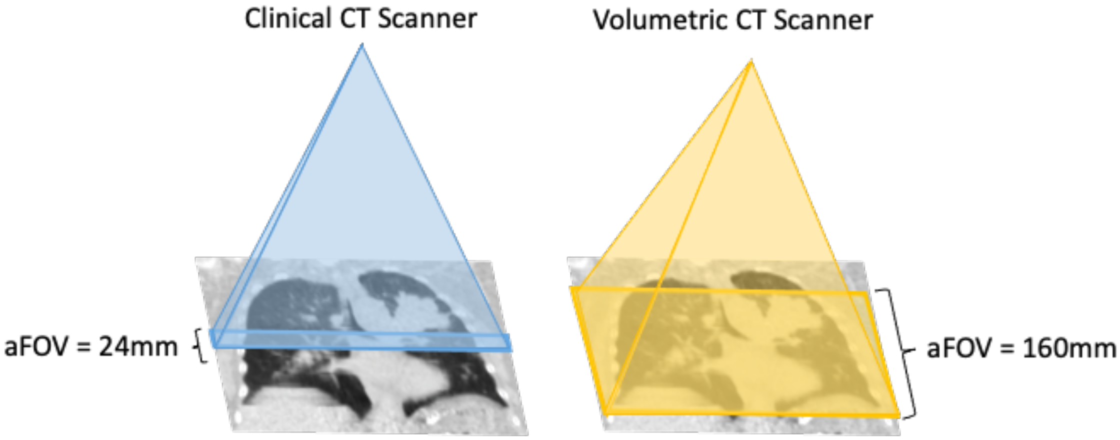

Figure 1-11 Volumetric CT geometry.
A typical clinical CT scanner (left) has a narrow cone angle, giving a narrow aFOV (24 mm in this example). In a volumetric CT scanner (right), a much wider cone angle is used, giving an aFOV of up to 160 mm.

In addition, this approach may have dose-reduction benefits. When comparing the imaging dose of a different 256-slice CT scanner (aFOV = 128mm) to a conventional 16-slice scanner, a 2014 study found that the dose from the 256-slice scanner was lower[68]. This was because the margin on the axial edges of the beam contributed less dose to the patient when a wide (128 mm) beam was used compared to when a narrow (16 mm) beam was used.

1.8.2 Volumetric 4D-CT

As discussed in Section 1.7, 4D-CT is an important part of the treatment planning process for NSCLC and other thoracic cancers. Capturing the effects of respiratory motion and appropriately compensating for this motion is essential to accurate radiation delivery. 4D-CT imaging must encompass a large volume (usually greater than 200 mm in length), and most clinical CT scanners have a narrow aFOV (often less than 40 mm), so they are prone to motion artifacts due to inconsistent patient breathing. Volumetric CT scanners can acquire 4D-CT across a 160 mm aFOV (or 140 mm aFOV with full lateral FOV) in a single couch position, because that entire volume is captured in a single rotation. Therefore, 4D-CT of that volume can be acquired within a single respiratory cycle with no visible motion artifacts. In addition, new CT scanners have faster rotation times than previous generations, reducing blur within images due to respiratory and cardiac motion.

To capture a longer field, a second or third couch position will be necessary, and a small overlapping region between each couch position may greatly reduce motion artifacts with minimal additional radiation dose. Image acquisition may also be performed in cine mode, which means that the x-ray beam is on and projection data is constantly being acquired for the duration of the scan. Cine mode acquisition allows reconstruction of images with very high temporal resolution (down to 0.1 s between images). This can also be used to accurately match images acquired from different couch positions to the same respiratory phase, resulting in minimal motion artifacts. The reduction of motion artifacts in v4D-CT and the quantitative improvements in contouring will be explored in Chapter 3 of this thesis.

1.9 Ventilation Imaging

This section will review the imaging methods used to estimate the regional distribution of ventilation, which describes the flow of air into and out of the lungs. Imaging methods directly or indirectly measure the amount of air, or a tracer, that was delivered to a voxel within the lungs, which is assumed to be directly related to the air flow in that region.

1.9.1 Contrast-Enhanced CT Ventilation Imaging

Ventilation can be directly measured by CT using the inhalation of ^{133}Xe, which is radio opaque. Researchers began studying this over 40 years ago[69,70], but the amount of work done in the area has greatly increased since 2000[71], and has been done in both animal and human studies. Generally, lower concentrations of Xe gas are used for human studies to minimize the sedative effects of Xe. Often, multiple breaths of Xenon are used so the gas has ample opportunity to fully wash into the lungs. Images may be acquired during the wash-in process to map wash-in and wash-out constants[71,72], or a single image each from baseline and estimated peak Xe concentration may be used[73]. In the latter case, both images are acquired at the same place in the breathing cycle to ensure that the change in density is from Xenon alone. One recent study demonstrated the feasibility of imaging ventilation with a single breath of high-concentration (70%) Xenon[73]. Image registration and subtraction can then be used to map the change in electron density, which is linearly related to the amount of Xenon in each voxel[71] and assumed to be directly related to ventilation within that region. Xe is able to diffuse into the bloodstream, so measures of gas exchange and perfusion are also possible using inhaled Xe[74].

1.9.2 Non-Contrast Enhanced CT Ventilation Imaging

This method has been used on breath-hold CT images acquired at end-inspiration and -expiration, and on end-inspiration and -expiration phases of a 4D-CT scan. Deformable image registration is used to register the inspiration image to the expiration image, and the density change at each voxel is assumed to be the result of a change in air content in the voxel. The first published method to derive a ventilation map from 4D-CT uses the following formula in which $\mathrm{HU_{in}}$ and $\mathrm{HU_{out}}$ are the CT number of the voxel in the inhale and exhale images, respectively, to calculate specific ventilation, SV[75]:

$$SV = 1000 \times \frac{HU_{in} - HU_{ex}}{HU_{ex}(1000 + HU_{in})}$$

This method estimates specific ventilation, which is ventilation per unit lung volume. Several different formulas have since been developed to convert the two images into the most accurate ventilation map possible. When compared to direct measures of ventilation such as PET and MRI methods, the performance of this class of methods has varied widely[76,77].

Shortly after the publication of the first density-based method for non-contrast enhanced CT ventilation imaging, another method was published which does not require a density calculation but relies on the deformation vector field generated by registration between inhale and exhale images. The following formula is applied to the deformation vector field, u(x,y,z), to calculate the Jacobian determinant of the field, J[78]:

$$J(x,y,z) = 1 + \begin{vmatrix} \frac{\partial u_x(x,y,z)}{\partial x} & \frac{\partial u_x(x,y,z)}{\partial y} & \frac{\partial u_x(x,y,z)}{\partial z} \\ \frac{\partial u_y(x,y,z)}{\partial x} & \frac{\partial u_y(x,y,z)}{\partial y} & \frac{\partial u_y(x,y,z)}{\partial z} \\ \frac{\partial u_z(x,y,z)}{\partial x} & \frac{\partial u_z(x,y,z)}{\partial y} & \frac{\partial u_z(x,y,z)}{\partial z} \end{vmatrix}$$

Many variations of this original approach have been published to attempt to improve the stability and accuracy of the method[79–82]. To date, registration-based CT ventilation imaging methods show low to moderate correlation with gold-standard methods and contrast-enhanced methods described above[76].

The reasons for the variable correlation between non-contrast enhanced CT methods with gold-standard methods are debated and may be broken down into three main categories. The first possible cause is the images used for ventilation calculation. 4D-CT motion artifacts have been shown to cause artifacts in ventilation imaging, so every effort to reduce motion artifacts can be expected to support more accurate ventilation calculations[83]. Breath-hold imaging is a possible way to address this problem, but this would require additional imaging dose to the patient and does not represent the way the patient will be breathing during radiation therapy in most cases. The second variable is the choice of image registration method. Both density-based and registration-based ventilation calculations are highly dependent on the image registration used[84], so consistently accurate registration is required for consistently accurate ventilation mapping. The final variable is the method used to calculate ventilation maps, and there is still much research activity ongoing to optimize these methods. However, no method will be reliable without high quality images and registration.

1.9.3 Other Methods of Ventilation Imaging

Nuclear imaging was the first method used to image lung ventilation, initially using radioactive ^{81m}Kr nearly 50 years ago[85], followed by ^{133}Xe[86]. Today, the standard method uses aerosolized solid particles labelled with ^{99m}Tc, called Technegas[87]. Inhaled particles are deposited by collision with the airway walls and by diffusion in the alveoli[88]. The deposited particles are then imaged by SPECT, generating a relative map of ventilation. ^{68}Ga can also be used in a Technegas generator to create an aerosol agent suitable for PET imaging, called "Galligas"[89]. While PET imaging is more expensive and less widely available, it has high sensitivity and spatial resolution[90].

MRI has been used to measure ventilation directly and indirectly. Hyperpolarized noble gas MRI is a direct measure of ventilation in which a noble gas isotope (most commonly

^{129}Xe) goes through a "hyperpolarization" process. The patient inhales a volume of this hyperpolarized gas and holds their breath while the gas itself is imaged by the MR scanner[91,92]. In the resulting image, the strength of the signal in each voxel is assumed to be directly related to the volume of noble gas contained in that voxel, and therefore a measure of the flow of air into that region of the lung in a single breath. The patient's anatomy is also imaged in breath-hold for anatomical reference. Non-contrast methods have also been developed to estimate ventilation using MRI sequences used under breath hold[93,94] or while free breathing[95,96].

The rapid growth of machine learning and deep learning in medical imaging has also led to recent investigations of deep learning techniques to derive ventilation images directly from 4D-CT or breath-hold CT images. Several studies have been published in the past 5 years demonstrating the many ways this approach can be used[97–100]. The published results are highly variable by method, and many have not yet undergone validation with an external dataset. However, these methods show moderate correlation with accepted methods, and are a promising avenue for future research.

1.10 Lung Perfusion Imaging

This section will review the methods used to image perfusion, or blood flow, in the lungs. Most images use an injected contrast agent which will change the signal intensity in each voxel of the resulting image. As with ventilation imaging, perfusion information is useful in assessing lung health and function for a variety of applications and may be useful for making treatment decisions for patients with NSCLC, such as suitability for surgery or for functional avoidance in radiation therapy.

1.10.1 Nuclear Perfusion Imaging

Ventilation and perfusion imaging were among the early uses for nuclear imaging, which began with 2-dimensional scintigraphy. Today, both SPECT[88,101] and PET[102] are used to generate 3-dimensional images of perfusion. This technique was first used in SPECT, when macroaggregated human albumen (MAA) is labelled with a radioactive tracer, usually ^{99m}Tc, which emits gamma rays for SPECT imaging. It was later shown that by using the same method, the MAA can also be labelled using ^{68}Ga, which emits positrons for PET imaging[103]. When the labelled MAA is injected into a vein, it travels with the blood through the right side of the heart and into the lungs through the pulmonary artery. The MAA particles are too large to pass through the capillaries in the lungs and become lodged there. The number of lodged particles in a region of tissue, and therefore the signal measured from that tissue, is proportionate to the blood flow through that area.

1.10.2 CT Perfusion Imaging

Dynamic contrast-enhanced CT perfusion takes advantage of the high temporal (0.5 s or less per image) and spatial (0.625 mm in-plane) resolution of modern CT scanners. It is a well-established technique for measuring blood flow and related properties such as mean transit time[104]. It has been validated for use in the lungs under breath-hold conditions, and is used widely in the brain and other organs[104].

The imaging procedure involves the venous injection of a bolus of iodine-based contrast, which reaches the organ of interest. The contrast agent strongly absorbs imaging x-rays (usually 100-120 kVp)[105], so it causes CT signal enhancement as a linear function of the concentration[105]. After injection, it is assumed to be uniformly mixed with the blood. High temporal-resolution imaging is acquired as the contrast washes into the organ, passes through the arteries into the capillaries, and travels out through the veins. The contrast agent can permeate the blood vessel walls, so some contrast diffuses out of the vessels and into the surrounding interstitial space[104].

Dynamic CT perfusion is an analysis of the change in CT number within a voxel over time. Therefore, image registration may be required to ensure that a single voxel captures the same tissue region throughout the entire image series. The registered images are then analyzed using a deconvolution-based method, which requires variables defined here. The blood flow is the rate of flow through a blood vessel (F, units: mL/min/100g), the concentration of contrast agent in the artery is $C_a(t)$, and the signal from a single voxel over time is called the time-density curve ($Q(t)$)[104].

If we consider a special case where the arterial concentration of contrast approaches a delta function (an infinitely narrow volume of contrast in which unit mass is deposited instantaneously in the region to be measured) then the time-density curve would take a particular form called the impulse residue function (IRF, R(t)). Plots to demonstrate these functions are given in Figure 1-12. To approach a more realistic scenario, one may imagine an arterial concentration composed of a series of delta functions of different heights, and the limit as this function becomes continuous. The tissue time-density curve (TDC) will then be made up of a series of IRFs, and in the continuous limit, also becomes a continuous function. The TDC can therefore be defined by Equation 1-2 below where $\otimes$ is the convolution operator[104]:

Equation 1-2

$$Q(t) = F \cdot C_a(t) \otimes R(t)$$

In Equation 1-2 above, Q(t) is the time-density curve, F is the rate of flow, $C_a(t)$ is the concentration of contrast agent in the artery, and R(t) is the impulse residue function.

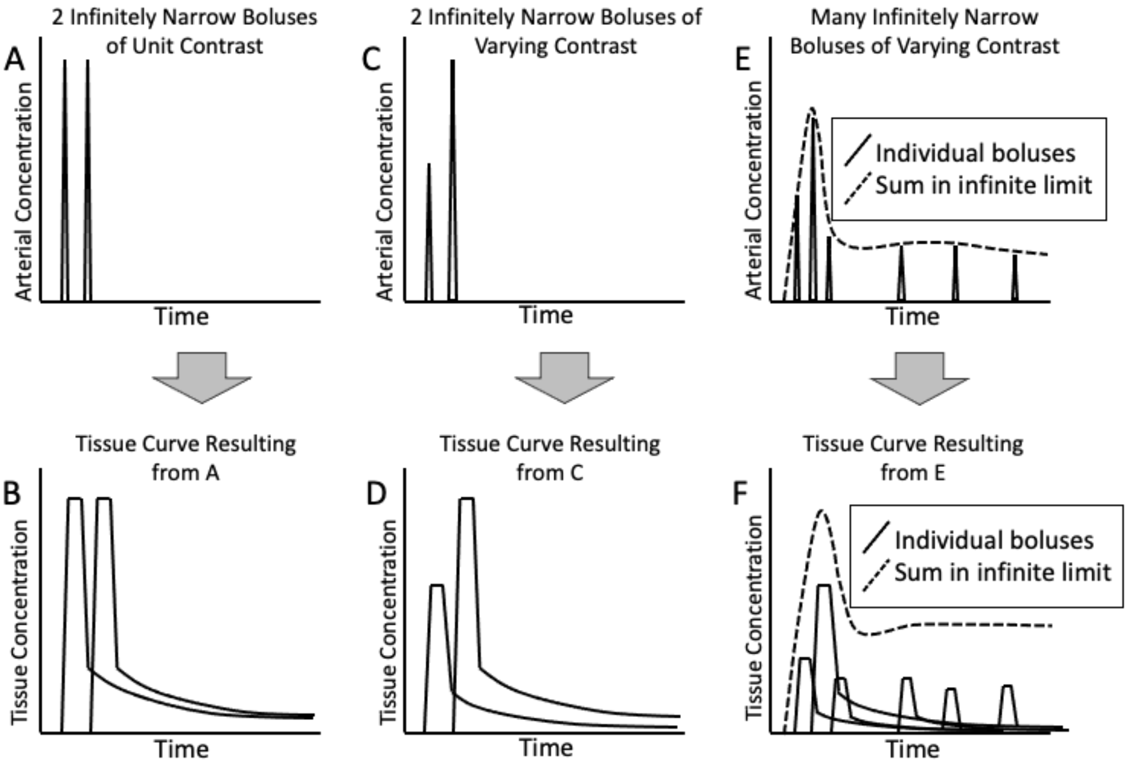

Figure 1-12 Convolution of an arterial contrast concentration curve and an impulse residue function.
This figure illustrates the convolution process by which the time-density curve measured in tissue can be derived from the convolution of an arterial contrast concentration curve and an impulse residue function. Adapted from Miles and Cuenod[104].

If the TDC and $C_a(t)$ are known from the image data, then R(t) is calculated for each voxel by deconvolving $C_a(t)$ from the TDC, and blood flow (F) is the height of R(t). Medical software is available for this analysis, and for this thesis a modified trial version of the software was used (CT Perfusion, GE Healthcare, Milwaukee).

For lung perfusion imaging, a bolus of iodine-based contrast is injected into a vein, which moves with the blood flow into the heart and through the right atrium and ventricle, into the lungs via the pulmonary artery. In this case, the pulmonary artery is used to define the arterial input function. If the images are acquired during free-breathing, then deformable image registration is required to register the entire image series before voxel-wise analysis.

1.10.3 Ventilation-Perfusion Imaging

As described in Section 1.2, both ventilation and perfusion must occur in the functional units of the lung, the alveoli, for gas exchange, the function of the lungs, to occur. If either ventilation or perfusion is reduced, the function of that lung region is also reduced. Changes such as these appear clearly in a ventilation-perfusion ratio (V/Q) map. For example, in the case of a pulmonary embolism, perfusion to a region of the lung is suddenly reduced due to a blood clot, but ventilation is largely unchanged. Therefore, the V/Q ratio will be higher in this region of the lung than the surrounding areas.

V/Q imaging is a well-established technique in nuclear medicine, used to diagnose pulmonary embolism and other disorders[88,90]. First, ventilation imaging is performed as described in Section 1.9.3. Then, there must be a waiting period to ensure that the signal from the ventilation imaging tracer has sufficiently decayed and will not contaminate the perfusion image. The perfusion imaging is performed with a higher radiation dose than ventilation, so it is performed second to ensure that one signal does not contaminate the other. Perfusion imaging with PET or SPCT is performed as described in Section 1.10.2. The voxel-by-voxel ratio of the two images is calculated to generate a V/Q map, which is then typically analyzed qualitatively by a radiologist for signs of pathology.

As introduced in Section 1.5.2, functional lung imaging has been proposed as a method to reduce the chance of RILI by prioritizing the sparing of highly functional lung tissue. There have been many studies showing that avoidance volumes can be generated from ventilation[41,42,106,107] or perfusion imaging[108–110], and a small number of studies incorporating both ventilation and perfusion from nuclear imaging[111,112]. While ventilation-alone or perfusion-alone methods show promise, each provides an incomplete picture of lung function. In patients with NSCLC, PET-CT based ventilation, perfusion, and V/Q imaging were each shown to contribute unique information about the patient's lung function, as correlation between ventilation and perfusion maps varied widely[113]. This suggests that ventilation, perfusion, and V/Q ratio should all be studied to determine which metric, or combination of metrics, performs best in reducing risk of RILI in patients. One animal study has reported CT perfusion as a stronger predictor of CT-measured density change than CT-based Jacobian ventilation, but the clinical consequences of this finding require further study[114]. So far, studies to explore all these metrics rely largely on nuclear imaging methods. However, PET imaging is costly, and clinical translation of PET V/Q imaging for all patients is unlikely. If V/Q imaging could be performed using CT in the same session as CT simulation for treatment planning, it may be more easily and widely applied. There is therefore a need for an accurate method for CT-based V/Q imaging which can be easily integrated into existing clinical routines.

V/Q imaging using CT has been shown to be feasible in patients with suspected pulmonary embolism[115] but is not part of any clinical standard of care. This is due, in part, to the fact that dynamic CT perfusion imaging has not been possible over the entire lung volume at high temporal frequency. In this thesis, we took advantage of the wide axial field-of-view of a volumetric CT scanner to generate both ventilation and perfusion imaging in a single dynamic contrast-enhanced CT scan. This enabled CT-based ventilation, perfusion, and V/Q mapping in NSCLC patients for the first time. This method is introduced in Chapter 4 of the thesis and may have wide applications in research and clinical practice.

1.11 Thesis Hypotheses and Objectives

The goals of this thesis are to demonstrate the utility of volumetric CT for clinical and research applications in radiation oncology, and to develop a simple functional lung imaging pipeline to generate ventilation, perfusion, and ventilation-perfusion ratio imaging using a volumetric CT scanner. In this thesis I developed and demonstrated how new imaging protocols using volumetric CT advance both anatomical and functional lung imaging in ways that can be implemented to impact clinical care and provide new opportunities for clinical research into lung function in patients with thoracic cancers. The specific research objectives of this thesis are:

1. To test the utility of volumetric CT imaging for simulation and radiation treatment planning using a Catphan phantom.
2. To study the reduction in respiratory motion artifacts when 4D-CT imaging is performed on a volumetric CT scanner, and quantitatively evaluate the impact of

this artifact reduction on contours of images of a motion phantom and patients with NSCLC.

3. To develop, validate, and demonstrate the feasibility of using a pipeline for generating ventilation, perfusion, and ventilation-perfusion ratio (V/Q) images in a single imaging session using a volumetric CT scanner.

1.12 Thesis Outline

In Chapter 2, I demonstrated the utility of volumetric CT imaging for simulation and radiation treatment planning using a Catphan phantom. Volumetric CT scanners have a much wider cone angle than CT simulators used in the past, so it was important to validate that no artifacts were present that would decrease the accuracy of CT number in treatment planning images. This work was previously published in the Journal of Applied Clinical Medical Physics: Young HM, Park CK, Chau O-W, Lee T-Y, Gaede S. Technical Note: Volumetric computed tomography for radiotherapy simulation and treatment planning. J Appl Clin Med Phys. July 2021. doi:10.1002/acm2.13336. This article was published under an open access agreement.

In Chapter 3, I demonstrated the reduction in respiratory motion artifacts when 4D-CT imaging was performed on a volumetric CT scanner. I also quantitatively evaluated the impact of this reduction in motion artifacts on contouring in images of a motion phantom and patients with NSCLC. In phantom 4D-CT images, target contours were significantly smaller and less variable in v4D-CT images relative to clinical 4D-CT images. In patient images, the mean Hausdorff distance metric measuring the difference between contours on v4D-CT and clinical 4D-CT images was significantly related to the respiratory phase, indicating that motion artifacts contributed to these differences. This article is in preparation for submission to the journal Medical Physics by Young HM, Kempe J, Lee TY, Gaede S.

In Chapter 4, I developed a pipeline to generate lung ventilation, perfusion, and V/Q images from a single, contrast-enhanced imaging protocol using a volumetric CT scanner. I then demonstrated the feasibility of this protocol in two patients with NSCLC before and 6 weeks after conventional radiation therapy. Finally, I show preliminary evidence of a validation study using xenon-enhanced CT and ^{68}Ga-labelled MAA PET perfusion in anesthetized pigs. The feasibility of this protocol was demonstrated in the target patient population, and this method identified changes in the irradiated lobe of both patients 6 weeks after radiation therapy. The validation evidence shows modest voxel-wise correlations between the novel method images and their established counterparts.

In Chapter 5, a summary of the findings and conclusions of Chapters 2-4 is provided, and a discussion of limitations of the work. Finally, the future studies that are planned to build on this work are presented.

1.13 References

1. *Canadian Cancer Statistics 2021*.; 2021.

2. *Canadian Cancer Statistics 2019*.; 2019.

3. Palma DA, Senan S, Tsujino K, et al. Predicting radiation pneumonitis after chemoradiation therapy for lung cancer: an international individual patient data meta-analysis. *Int J Radiat Oncol Biol Phys*. 2013;85(2):444-450.

4. Bradley JD, Paulus R, Komaki R, et al. Standard-dose versus high-dose conformal radiotherapy with concurrent and consolidation carboplatin plus paclitaxel with or without cetuximab for patients with stage IIIA or IIIB non-small-cell lung cancer (RTOG 0617): a randomised, two-by-two factorial p. *Lancet Oncol*. 2015;16(2):187-199.

5. Chun SG, Hu C, Choy H, et al. Impact of intensity-modulated radiation therapy technique for locally advanced non–small-cell lung cancer: a secondary analysis of the NRG oncology RTOG 0617 randomized clinical trial. *J Clin Oncol*. 2017;35(1):56.

6. Boulet L-P. *Applied Respiratory Pathophysiology*. CRC Press; 2017.

7. Shah PL, Herth FJF, Lee YCG, Criner GJ. *Essentials of Clinical Pulmonology*. CRC Press; 2018.

8. Young HM, Eddy RL, Parraga G. MRI and CT lung biomarkers: Towards an in vivo understanding of lung biomechanics. *Clin Biomech*. 2017. doi:10.1016/j.clinbiomech.2017.09.016

9. Sittenfeld SMC, Ward MC, Tendulkar RD, Videtic GMM. *Essentials of Clinical Radiation Oncology*. Springer Publishing Company; 2021.

10. Goldstraw P, Chansky K, Crowley J, et al. The IASLC lung cancer staging project: proposals for revision of the TNM stage groupings in the forthcoming (eighth)

edition of the TNM classification for lung cancer. *J Thorac Oncol*. 2016;11(1):39-51.

11. Brierley JD, Gospodarowicz MK, Wittekind C. *TNM Classification of Malignant Tumours*. John Wiley & Sons; 2017.

12. Vinod SK, Hau E. Radiotherapy treatment for lung cancer: Current status and future directions. *Respirology*. 2020;25:61-71.

13. Le Chevalier T, Arriagada R, Quoix E, et al. Radiotherapy alone versus combined chemotherapy and radiotherapy in nonresectable non-small-cell lung cancer: first analysis of a randomized trial in 353 patients. *JNCI J Natl Cancer Inst*. 1991;83(6):417-423.

14. Sause WT, Scott C, Taylor S, et al. Radiation Therapy Oncology Group (RTOG) 88–08 and Eastern Cooperative Oncology Group (ECOG) 4588: preliminary results of a phase III trial in regionally advanced, unresectable non-small-cell lung cancer. *JNCI J Natl Cancer Inst*. 1995;87(3):198-205.

15. Keall PJ, Mageras GS, Balter JM, et al. The management of respiratory motion in radiation oncology report of AAPM Task Group 76 a. *Med Phys*. 2006;33(10):3874-3900.

16. Lambrecht M, Sonke J-J, Nestle U, et al. Quality assurance of four-dimensional computed tomography in a multicentre trial of stereotactic body radiotherapy of centrally located lung tumours. *Phys imaging Radiat Oncol*. 2018;8:57-62.

17. Wikström KA, Isacsson UM, Pinto MC, Nilsson KM, Ahnesjö A. Evaluation of irregular breathing effects on Internal Target Volume definition for lung cancer radiotherapy. *Med Phys*. March 2021. doi:10.1002/mp.14824

18. Vergalasova I, Cai J. A modern review of the uncertainties in volumetric imaging of respiratory-induced target motion in lung radiotherapy. *Med Phys*. 2020;47(10):e988-e1008. doi:https://doi.org/10.1002/mp.14312

19. Cancer Care Ontario Lung Working Group. *Radiation Treatment Quality Expectations by Disease Site*.; 2020.

20. Robinson A, Vella ET, Ellis PM, et al. Recommendations for the Treatment of Patients with Clinical Stage III Non-Small Cell Lung Cancer: Endorsement of the 2019 National Institute for Health and Care Excellence Guidance and the 2018 Society for Immunotherapy of Cancer Guidance. *Progr Evidence-Based Care Guidel*. 2020;(7-3).

21. Group IMRTCW. Intensity-modulated radiotherapy: current status and issues of interest. *Int J Radiat Oncol Biol Phys*. 2001;51(4):880-914.

22. Otto K. Volumetric modulated arc therapy: IMRT in a single gantry arc. *Med Phys*. 2008;35(1):310-317.

23. Holt A, van Vliet-Vroegindeweij C, Mans A, Belderbos JS, Damen EMF. Volumetric-modulated arc therapy for stereotactic body radiotherapy of lung tumors: a comparison with intensity-modulated radiotherapy techniques. *Int J Radiat Oncol Biol Phys*. 2011;81(5):1560-1567.

24. Caillet V, Booth JT, Keall P. IGRT and motion management during lung SBRT delivery. *Phys Medica*. 2017;44:113-122.

25. Purdie TG, Bissonnette J-P, Franks K, et al. Cone-beam computed tomography for on-line image guidance of lung stereotactic radiotherapy: localization, verification, and intrafraction tumor position. *Int J Radiat Oncol Biol Phys*. 2007;68(1):243-252.

26. Heinzerling JH, Hampton CJ, Robinson M, et al. Use of surface-guided radiation therapy in combination with IGRT for setup and intrafraction motion monitoring during stereotactic body radiation therapy treatments of the lung and abdomen. *J Appl Clin Med Phys*. 2020;21(5):48-55.

27. Hall EJ, Giaccia AJ. *Radiobiology for the Radiologist*. Vol 6. Philadelphia; 2006.

28. Stevens CW, Munden RF, Forster KM, et al. Respiratory-driven lung tumor motion is independent of tumor size, tumor location, and pulmonary function. *Int J Radiat Oncol Biol Phys*. 2001;51(1):62-68.

29. Hanley J, Debois MM, Mah D, et al. Deep inspiration breath-hold technique for lung tumors: the potential value of target immobilization and reduced lung density in dose escalation. *Int J Radiat Oncol Biol Phys*. 1999;45(3):603-611.

30. Rosenzweig KE, Hanley J, Mah D, et al. The deep inspiration breath-hold technique in the treatment of inoperable non–small-cell lung cancer. *Int J Radiat Oncol Biol Phys*. 2000;48(1):81-87.

31. Yang M, Timmerman R. Stereotactic ablative radiotherapy uncertainties: delineation, setup and motion. In: *Seminars in Radiation Oncology*. Vol 28. Elsevier; 2018:207-217.

32. Molitoris JK, Diwanji T, Snider III JW, et al. Advances in the use of motion management and image guidance in radiation therapy treatment for lung cancer. *J Thorac Dis*. 2018;10(Suppl 21):S2437.

33. Kubo HD, Hill BC. Respiration gated radiotherapy treatment: a technical study. *Phys Med Biol*. 1996;41(1):83.

34. Vedam SS, Keall PJ, Kini VR, Mohan R. Determining parameters for respiration-gated radiotherapy. *Med Phys*. 2001;28(10):2139-2146.

35. Cox JD. Toxicity criteria of the radiation therapy oncology group (RTOG) and the European organization for research and treatment of cancer (EORTC). *Int J Radiat Oncol Biol Phys*. 1995;31:1341-1346.

36. US Department of Health and Human Services. *Common Terminology Criteria Fo Adverse Events (CTCAE).*; 2017.

37. Arroyo-Hernández M, Maldonado F, Lozano-Ruiz F, Muñoz-Montaño W, Nuñez-Baez M, Arrieta O. Radiation-induced lung injury: current evidence. *BMC Pulm*

Med. 2021;21(1):1-12.

38. Hanania AN, Mainwaring W, Ghebre YT, Hanania NA, Ludwig M. Radiation-induced lung injury: assessment and management. *Chest*. 2019;156(1):150-162.

39. Roy S, Salerno KE, Citrin DE. Biology of radiation-induced lung injury. In: *Seminars in Radiation Oncology*. Vol 31. Elsevier; 2021:155-161.

40. Tsujino K, Hashimoto T, Shimada T, et al. Combined analysis of V20, VS5, pulmonary fibrosis score on baseline computed tomography, and patient age improves prediction of severe radiation pneumonitis after concurrent chemoradiotherapy for locally advanced non–small-cell lung cancer. *J Thorac Oncol*. 2014;9(7):983-990.

41. Yaremko BP, Guerrero TM, Noyola-Martinez J, et al. Reduction of normal lung irradiation in locally advanced non–small-cell lung cancer patients, using ventilation images for functional avoidance. *Int J Radiat Oncol Biol Phys*. 2007;68(2):562-571.

42. Yamamoto T, Kabus S, Von Berg J, Lorenz C, Keall PJ. Impact of four-dimensional computed tomography pulmonary ventilation imaging-based functional avoidance for lung cancer radiotherapy. *Int J Radiat Oncol Biol Phys*. 2011;79(1):279-288.

43. Vinogradskiy Y, Castillo R, Castillo E, et al. Results of a multi-institutional phase 2 clinical trial for 4DCT-ventilation functional avoidance thoracic radiation therapy. *Int J Radiat Oncol Biol Phys*. 2022;112(4):986-995.

44. Hounsfield GN. Computerized transverse axial scanning (tomography): Part 1. Description of system. *Br J Radiol*. 1973;46(552):1016-1022.

45. Bushberg JT, Boone JM. *The Essential Physics of Medical Imaging*. Lippincott Williams & Wilkins; 2011.

46. Hurlock GS, Higashino H, Mochizuki T. History of cardiac computed

tomography: single to 320-detector row multislice computed tomography. *Int J Cardiovasc Imaging*. 2009;25(1):31-42.

47. Tang X, Hsieh J, Hagiwara A, Nilsen RA, Thibault J-B, Drapkin E. A three-dimensional weighted cone beam filtered backprojection (CB-FBP) algorithm for image reconstruction in volumetric CT under a circular source trajectory. *Phys Med Biol*. 2005;50(16):3889.

48. Axente M, Paidi A, Von Eyben R, et al. Clinical evaluation of the iterative metal artifact reduction algorithm for CT simulation in radiotherapy. *Med Phys*. 2015;42(3):1170-1183.

49. Barrett JF, Keat N. Artifacts in CT: recognition and avoidance. *Radiographics*. 2004;24(6):1679-1691.

50. Boas FE, Fleischmann D. CT artifacts: causes and reduction techniques. *Imaging Med*. 2012;4(2):229-240.

51. Vedam SS, Keall PJ, Kini VR, Mostafavi H, Shukla HP, Mohan R. Acquiring a four-dimensional computed tomography dataset using an external respiratory signal. *Phys Med Biol*. 2003;48(1):45-62. doi:10.1088/0031-9155/48/1/304

52. Pan T, Lee T-Y, Rietzel E, Chen GTY. 4D-CT imaging of a volume influenced by respiratory motion on multi-slice CT. *Med Phys*. 2004;31(2):333-340. doi:10.1118/1.1639993

53. Keall PJ, Starkschall G, Shukla H, et al. Acquiring 4D thoracic CT scans using a multislice helical method. *Phys Med Biol*. 2004;49(10):2053-2067. doi:10.1088/0031-9155/49/10/015

54. Chen Q-S, Weinhous MS, Deibel FC, Ciezki JP, Macklis RM. Fluoroscopic study of tumor motion due to breathing: Facilitating precise radiation therapy for lung cancer patients. *Med Phys*. 2001;28(9):1850-1856. doi:10.1118/1.1398037

55. Park JC, Park SH, Kim JH, et al. Liver motion during cone beam computed

tomography guided stereotactic body radiation therapy. *Med Phys*. 2012;39(10):6431-6442. doi:10.1118/1.4754658

56. Lauria M, Navaratna R, O'Connell D, Santhanam A, Lee P, Low DA. Investigating internal–external motion correlation using fast helical CT. *Med Phys*. 2021;48(4):1823-1831.

57. Fayad H, Pan T, François Clement J, Visvikis D. Correlation of respiratory motion between external patient surface and internal anatomical landmarks. *Med Phys*. 2011;38(6Part1):3157-3164.

58. Ionascu D, Jiang SB, Nishioka S, Shirato H, Berbeco RI. Internal-external correlation investigations of respiratory induced motion of lung tumors. *Med Phys*. 2007;34(10):3893-3903.

59. Pierce G, Wang K, Gaede S, Battista J, Lee T. The effect of an inconsistent breathing amplitude on the relationship between an external marker and internal lung deformation in a porcine model. *Med Phys*. 2010;37(11):5951-5960.

60. Lee D, Greer PB, Paganelli C, Ludbrook JJ, Kim T, Keall P. Audiovisual biofeedback improves the correlation between internal/external surrogate motion and lung tumor motion. *Med Phys*. 2018;45(3):1009-1017.

61. Yamamoto T, Langner U, Loo BW, Shen J, Keall PJ. Retrospective Analysis of Artifacts in Four-Dimensional CT Images of 50 Abdominal and Thoracic Radiotherapy Patients. *Int J Radiat Oncol Biol Phys*. 2008;72(4):1250-1258. doi:10.1016/j.ijrobp.2008.06.1937

62. Clements N, Kron T, Franich R, et al. The effect of irregular breathing patterns on internal target volumes in four-dimensional CT and cone-beam CT images in the context of stereotactic lung radiotherapy. *Med Phys*. 2013;40(2):21904. doi:10.1118/1.4773310

63. Sentker T, Schmidt V, Ozga A-K, et al. 4D CT image artifacts affect local control

in SBRT of lung and liver metastases. *Radiother Oncol J Eur Soc Ther Radiol Oncol*. 2020;148:229-234. doi:10.1016/j.radonc.2020.04.006

64. Pan T, Sun X, Luo D. Improvement of the cine-CT based 4D-CT imaging. *Med Phys*. 2007;34(11):4499-4503.

65. Carnes G, Gaede S, Yu E, Van Dyk J, Battista J, Lee T-Y. A fully automated non-external marker 4D-CT sorting algorithm using a serial cine scanning protocol. *Phys Med Biol*. 2009;54(7):2049-2066. doi:10.1088/0031-9155/54/7/013

66. Haasbeek CJA, Spoelstra FOB, Lagerwaard FJ, et al. Impact of audio-coaching on the position of lung tumors. *Int J Radiat Oncol Biol Phys*. 2008;71(4):1118-1123.

67. Mori S, Endo M, Tsunoo T, et al. Physical performance evaluation of a 256-slice CT-scanner for four-dimensional imaging. *Med Phys*. 2004;31(6):1348-1356.

68. Mori S, Endo M, Nishizawa K, Murase K, Fujiwara H, Tanada S. Comparison of patient doses in 256-slice CT and 16-slice CT scanners. *Br J Radiol*. 2006;79(937):56-61.

69. Gur D, Drayer BP, Borovetz HS, Griffith BP, Hardesty RL, Wolfson SK. Dynamic computed tomography of the lung: regional ventilation measurements. *J Comput Assist Tomogr*. 1979;3(6):749-753.

70. Murphy DMF, Nicewicz JT, Zabbatino SM, Moore RA. Local pulmonary ventilation using nonradioactive xenon-enhanced ultrafast computed tomography. *Chest*. 1989;96(4):799-804.

71. Marcucci C, Nyhan D, Simon BA. Distribution of pulmonary ventilation using Xe-enhanced computed tomography in prone and supine dogs. *J Appl Physiol*. 2001;90(2):421-430. doi:10.1152/jappl.2001.90.2.421

72. Chon D, Simon BA, Beck KC, et al. Differences in regional wash-in and wash-out time constants for xenon-CT ventilation studies. *Respir Physiol Neurobiol*. 2005;148(1-2):65-83.

73. Pinkham DW, Negahdar M, Yamamoto T, et al. A Feasibility Study of Single-inhalation, Single-energy Xenon-enhanced CT for High-resolution Imaging of Regional Lung Ventilation in Humans. *Acad Radiol*. March 2018. doi:10.1016/j.acra.2018.03.006

74. Kreck TC, Krueger MA, Altemeier WA, et al. Determination of regional ventilation and perfusion in the lung using xenon and computed tomography. *J Appl Physiol*. 2001;91(4):1741-1749.

75. Guerrero T, Sanders K, Castillo E, et al. Dynamic ventilation imaging from four-dimensional computed tomography. *Phys Med Biol*. 2006;51(4):777-791. doi:10.1088/0031-9155/51/4/002

76. Kipritidis J, Tahir BA, Cazoulat G, et al. The VAMPIRE challenge: A multi-institutional validation study of CT ventilation imaging. *Med Phys*. 2019;46(3):1198-1217. doi:10.1002/mp.13346

77. Hegi-Johnson F, de Ruysscher D, Keall P, et al. Imaging of regional ventilation: Is CT ventilation imaging the answer? A systematic review of the validation data. *Radiother Oncol*. 2019;137:175-185. doi:10.1016/j.radonc.2019.03.010

78. Reinhardt JM, Ding K, Cao K, Christensen GE, Hoffman EA, Bodas S V. Registration-based estimates of local lung tissue expansion compared to xenon CT measures of specific ventilation. *Med Image Anal*. 2008;12(6):752-763. doi:10.1016/j.media.2008.03.007

79. Ding K, Cao K, Fuld MK, et al. Comparison of image registration based measures of regional lung ventilation from dynamic spiral CT with Xe-CT. *Med Phys*. 2012;39(8):5084-5098. doi:10.1118/1.4736808

80. Kipritidis J, Siva S, Hofman MS, Callahan J, Hicks RJ, Keall PJ. Validating and improving CT ventilation imaging by correlating with ventilation 4D-PET/CT using 68Ga-labeled nanoparticles. *Med Phys*. 2014;41(1):11910. doi:10.1118/1.4856055

81. Tahir BA, Van Holsbeke C, Ireland RH, et al. Comparison of CT-based Lobar Ventilation with 3He MR Imaging Ventilation Measurements. *Radiology*. 2016;278(2):585-592. doi:10.1148/radiol.2015142278

82. Castillo E, Castillo R, Vinogradskiy Y, et al. Robust CT ventilation from the integral formulation of the Jacobian. *Med Phys*. 2019;46(5):2115-2125. doi:https://doi.org/10.1002/mp.13453

83. Yamamoto T, Kabus S, Lorenz C, et al. 4D CT lung ventilation images are affected by the 4D CT sorting method. *Med Phys*. 2013;40(10):101907. doi:10.1118/1.4820538

84. Yamamoto T, Kabus S, Klinder T, et al. Four-dimensional computed tomography pulmonary ventilation images vary with deformable image registration algorithms and metrics. *Med Phys*. 2011;38(3):1348-1358. doi:10.1118/1.3547719

85. Fazio F, Jones T. Assessment of regional ventilation by continuous inhalation of radioactive krypton-81m. *Br Med J*. 1975;3(5985):673-676.

86. Loken MK, Westgate HD. Using Xenon-133 and a scintillation camera to evaluate pulmonary function. *J Nucl Med*. 1968;9(2):45-50.

87. Kotrappa P, Raghunath B, Subramanyam PS, Raikar UR, Sharma SM. Scintiphotography of lungs with dry aerosol--generation and delivery system: concise communication. *J Nucl Med Off Publ Soc Nucl Med*. 1977;18(11):1082-1085.

88. Bajc M, Neilly JB, Miniati M, Schuemichen C, Meignan M, Jonson B. EANM guidelines for ventilation/perfusion scintigraphy. *Eur J Nucl Med Mol Imaging*. 2009;36(8):1356-1370.

89. Kotzerke J, Andreeff M, Wunderlich G. PET aerosol lung scintigraphy using Galligas. *Eur J Nucl Med Mol Imaging*. 2010;37(1):175-177.

90. Hofman MS, Beauregard J-M, Barber TW, Neels OC, Eu P, Hicks RJ. 68Ga

PET/CT ventilation–perfusion imaging for pulmonary embolism: a pilot study with comparison to conventional scintigraphy. *J Nucl Med*. 2011;52(10):1513-1519.

91. MacFall JR, Charles HC, Black RD, et al. Human lung air spaces: potential for MR imaging with hyperpolarized He-3. *Radiology*. 1996;200(2):553-558.

92. Ebert M, Grossmann T, Heil W, et al. Nuclear magnetic resonance imaging with hyperpolarised helium-3. *Lancet*. 1996;347(9011):1297-1299.

93. Bergin CJ, Pauly JM, Macovski A. Lung parenchyma: projection reconstruction MR imaging. *Radiology*. 1991;179(3):777-781.

94. Johnson KM, Fain SB, Schiebler ML, Nagle S. Optimized 3D ultrashort echo time pulmonary MRI. *Magn Reson Med*. 2013;70(5):1241-1250.

95. Capaldi DPI, Sheikh K, Guo F, et al. Free-breathing pulmonary 1H and Hyperpolarized 3He MRI: comparison in COPD and bronchiectasis. *Acad Radiol*. 2015;22(3):320-329.

96. Capaldi DPI, Eddy RL, Svenningsen S, et al. Free-breathing pulmonary MR imaging to quantify regional ventilation. *Radiology*. 2018;287(2):693.

97. Grover J, Byrne HL, Sun Y, Kipritidis J, Keall P. Investigating the use of machine learning to generate ventilation images from CT scans. *Med Phys*. 2022.

98. Zhong Y, Vinogradskiy Y, Chen L, et al. Deriving ventilation imaging from 4 DCT by deep convolutional neural network. *Med Phys*. 2019;46(5):2323-2329.

99. Kajikawa T, Kadoya N, Maehara Y, et al. A deep learning method for translating 3D-CT to SPECT ventilation imaging: First comparison with 81mKr-gas SPECT ventilation imaging. *Med Phys*. 2022.

100. Liu Z, Miao J, Huang P, et al. A deep learning method for producing ventilation images from 4DCT: First comparison with technegas SPECT ventilation. *Med*

Phys. 2020;47(3):1249-1257.

101. Palmer J, Bitzén U, Jonson B, Bajc M. Comprehensive ventilation/perfusion SPECT. *J Nucl Med*. 2001;42(8):1288-1294.

102. Vidal Melo MF, Layfield D, Harris RS, et al. Quantification of regional ventilation-perfusion ratios with PET. *J Nucl Med*. 2003;44(12):1982-1991.

103. Zhernosekov KP, Filosofov D V, Baum RP, et al. Processing of generator-produced 68Ga for medical application. *J Nucl Med*. 2007;48(10):1741-1748.

104. Miles KA, Cuenod CA, Husband J. Multi-detector computed tomography in oncology: CT perfusion imaging. 2007.

105. Lee TY, Ellis RJ, Dunscombe PB, et al. Quantitative computed tomography of the brain with xenon enhancement: a phantom study with the GE9800 scanner. *Phys Med Biol*. 1990;35(7):925.

106. Yamamoto T, Kabus S, Bal M, Keall P, Benedict S, Daly M. The first patient treatment of computed tomography ventilation functional image-guided radiotherapy for lung cancer. *Radiother Oncol*. 2016;118(2):227-231.

107. Vinogradskiy Y, Schubert L, Diot Q, et al. Regional lung function profiles of stage I and III lung cancer patients: an evaluation for functional avoidance radiation therapy. *Int J Radiat Oncol Biol Phys*. 2016;95(4):1273-1280.

108. Lavrenkov K, Christian JA, Partridge M, et al. A potential to reduce pulmonary toxicity: the use of perfusion SPECT with IMRT for functional lung avoidance in radiotherapy of non-small cell lung cancer. *Radiother Oncol*. 2007;83(2):156-162.

109. Lavrenkov K, Singh S, Christian JA, et al. Effective avoidance of a functional spect-perfused lung using intensity modulated radiotherapy (IMRT) for non-small cell lung cancer (NSCLC): An update of a planning study. *Radiother Oncol*. 2009;91(3):349-352.

110. Khalil AA, Hau E, Gebski V, et al. Personal innovative approach in radiation therapy of lung cancer-functional lung avoidance SPECT-guided (ASPECT) radiation therapy: a study protocol for phase II randomised double-blind clinical trial. *BMC Cancer*. 2021;21(1):1-9.

111. Siva S, Thomas R, Callahan J, et al. High-resolution pulmonary ventilation and perfusion PET/CT allows for functionally adapted intensity modulated radiotherapy in lung cancer. *Radiother Oncol*. 2015;115(2):157-162.

112. Kimura T, Doi Y, Nakashima T, et al. Combined ventilation and perfusion imaging correlates with the dosimetric parameters of radiation pneumonitis in radiation therapy planning for lung cancer. *Int J Radiat Oncol Biol Phys*. 2015;93(4):778-787.

113. Li Z, Le Roux P-Y, Callahan J, et al. Quantitative assessment of ventilation-perfusion relationships with gallium-68 positron emission tomography/computed tomography imaging in lung cancer patients. *Phys imaging Radiat Oncol*. 2022;22:8-12.

114. Wuschner AE, Wallat EM, Flakus MJ, et al. Radiation-induced Hounsfield unit change correlates with dynamic CT perfusion better than 4DCT-based ventilation measures in a novel-swine model. *Sci Rep*. 2021;11(1):1-14.

115. Zhang LJ, Zhou CS, Schoepf UJ, et al. Dual-energy CT lung ventilation/perfusion imaging for diagnosing pulmonary embolism. *Eur Radiol*. 2013;23(10):2666-2675.

CHAPTER 2

2 Volumetric Computed Tomography for Radiotherapy Simulation and Treatment Planning

We measured several quality metrics in phantom scans performed on a 256-slice volumetric CT scanner to assess the utility of volumetric CT for radiotherapy simulation and treatment planning. The results of the study showed that artifacts potentially introduced by volumetric CT imaging are mitigated by the scanner, and no clinically significant artifacts were observed. This study demonstrates the utility of volumetric CT for radiotherapy simulation, which can have an important clinical impact by greatly reducing the presence of 4D-CT motion artifacts that have been shown to negatively impact patient outcomes.

The contents of this chapter were previously published in the Journal of Applied Clinical Medical Physics: Young HM, Park CK, Chau O-W, Lee T-Y, Gaede S. Technical Note: Volumetric computed tomography for radiotherapy simulation and treatment planning. J Appl Clin Med Phys. July 2021. doi:10.1002/acm2.13336. This article was published under an open access agreement.

2.1 Introduction

Four-dimensional computed tomography (4D-CT) is part of the standard of care for radiotherapy treatment planning for tumours influenced by respiratory motion, such as in lung and liver cancer. Lung and liver tumours have been shown to move up to 50 mm during free breathing[1,2]. However, conventional CT scanners have a narrow axial field-of-view (aFOV) of 40mm or less, so images must be acquired at multiple couch positions and recombined to construct a complete image set. Irregular breathing motion during this acquisition can result in significant motion-induced artifacts[3]. These artifacts may lead to inaccuracies in target delineation and contouring organs at risk due to geometric distortion[4,5], and have been shown to significantly impact clinical outcomes in patients with lung and liver lesions[6].

New volumetric CT scanners (also called area detector scanners) with 160 mm aFOV greatly reduce the artifacts caused by irregular breathing motion during imaging[7]. However, accurate CT density measurements are critical for radiation dose calculations, and the volumetric geometry used in vCT may result in cone beam artifacts which could distort the measured CT number. This effect could limit the application of vCT for radiation treatment planning and dose calculations. Previous studies have investigated image quality metrics in other scanners, finding evidence of cone-beam artifacts that were not clinically significant[8]. In addition, one recent study investigated dose and effective energy in a 160mm aFOV scan in a volumetric scanner[9].

The objective of this study is to examine the image quality of vCT images acquired on the GE Revolution CT scanner across multiple axial fields-of-view using a Catphan 504 phantom (The Phantom Laboratory Inc., Greenwich, USA). CT number linearity, uniformity, noise, and low-contrast resolution were assessed across increasing aFOV. Furthermore, we generated relative electron density (RED) curves for clinical implementation in radiotherapy treatment planning systems.

2.2 Materials and Methods

2.2.1 Image Acquisition

The Catphan 504 phantom was imaged on a 256-slice GE Revolution volumetric CT scanner (GE Medical Systems, Madison, USA) at 120 kV, 590 mA, 0.625 mm pixel spacing, and 1.0 s rotation speed with 980 projections. Images were reconstructed with the "Standard" convolution kernel and the filter type "Medium Filter", with a cut-off frequency (5% MTF) of 8 lp/cm. Repeated scans with aFOV of 40, 80, 120, 140, and 160 mm were performed, and the entire phantom was scanned in axial mode for each aFOV. Phantom specifications for expected CT number and relative electron density (RED) for the phantom density inserts were taken from the Catphan 504 manual[10]. summarized in Table 2-1. To test for changes in image uniformity along the z-axis, the Catphan was imaged with an aFOV of 160 mm positioned in the center of the bore, and at the outer edges of the scanner.

Table 2-1 Catphan 504 phantom density insert measurements
Mean CT number measured in circular regions in the Catphan 504 phantom density inserts. Expected CT number given as [minimum, maximum] and relative electron density (RED) given in the Catphan manual.

Material	**Measured CT Number [HU]**					**Expected CT Number [HU]**	**RED**
	40 mm	80 mm	120 mm	140 mm	160 mm		
Teflon	889.01	890.37	900.94	904.68	904.86	[941, 1060]	1.868
Delrin	302.44	306.08	311.66	316.84	317.18	[344, 387]	1.363
Acrylic	121.68	120.89	120.48	121.21	120.13	[92, 137]	1.147
Polystyrene	-36.4	-36.3	-36.3	-35.8	-37.2	[-65, -29]	0.998
LDPE	-94.41	-92.85	-94.4	-93.15	-93.1	[-121, -87]	0.945
PMP	-187.45	-185.72	-185.8	-185.21	-185.61	[-220, -176]	0.853
Air	-995.73	-992.53	-992.24	-992.2	-990.92	[-1046, -986]	0.001

LDPE = Low-density polyethylene; PMP = Polymethylpentene

2.2.2 Image Analysis

Image analysis for CT number measurements including linearity, uniformity, noise, and low-contrast resolution was performed using ITK-SNAP (version 3.4.0)[11] for all aFOV values.

2.2.2.1 Linearity

Linearity was measured by measuring the average CT number in a region of interest (ROI) within the sensitometry (CTP404) module in inserts containing Teflon, Delrin, acrylic, polystyrene, low-density polyethylene (LDPE), polymethylpentene (PMP), and air as shown in Figure 2-1. These values were compared to the expected range given in the Catphan manual.

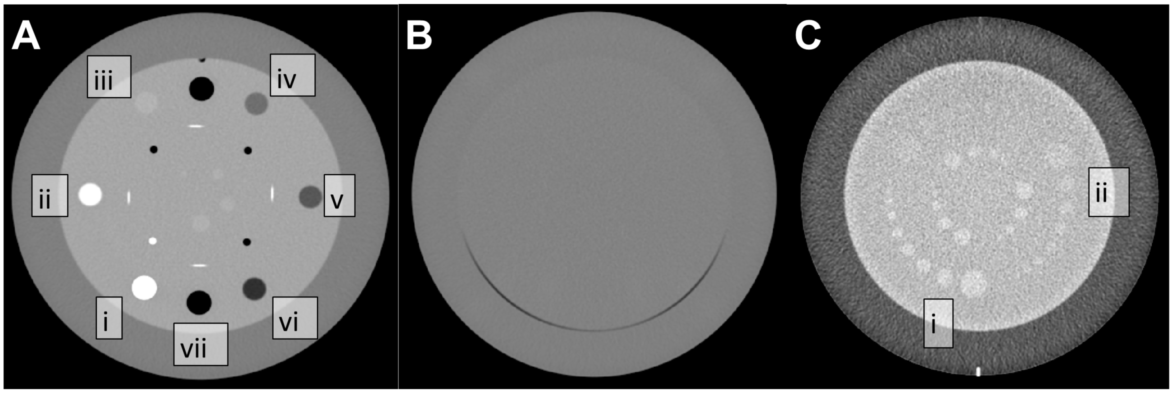

Figure 2-1 Axial CT images of Catphan 504 phantom modules analyzed using ITK-Snap (A) The sensitometry module used for linearity measurements containing (i) Teflon, (ii) Delrin, (iii) acrylic, (iv) polystyrene, (v) LDPE, (vi) PMP, and (vii) air density inserts (window width/window level = 600/0 HU). (B) The uniformity (CTP486) module used to measure uniformity and noise (window width/window level = 600/0 HU). (C) The low-contrast resolution (CTP515) module used to measure contrast-to-noise (CNR) in the (i) 1.0% and (ii) 0.5% nominal contrast level targets (window width/window level = 120/20 HU).

2.2.2.2 CT Number Uniformity

CT number uniformity across an image was evaluated using the phantom uniformity (CTP486) module using circular ROIs (area = 520 mm^2) manually placed in the centre of the phantom (1 ROI) and at the periphery of the phantom (4 ROIs) as described in the phantom manual. The mean intensity was measured in each ROI, and the absolute difference between the centre region and maximum periphery region was calculated using Equation 2-1:

Equation 2-1

$$Max\ difference = \left|CT_{mean,center} - CT_{max,periphery}\right|$$

The CT number [HU] difference measured in the uniformity module is expected to be within 2% (20 HU) of that of water, usually in the range 5 – 18 HU[10].

To test image uniformity in the z-direction, horizontal image profiles were taken across a uniform region of the phantom positioned at the outer edges of the scanner bore and in the center. These profiles were visually examined for artifacts. A longitudinal profile was also taken in a uniform region of the phantom, to evaluate possible correlations between CT number and position on the z-axis.

2.2.2.3 Image Noise

Image noise was quantified by measuring the standard deviation of the CT number within a circular ROI (area = 2500 mm^2) in the uniformity module.

2.2.2.4 Low-Contrast Resolution

Low-contrast resolution was assessed using three nominal target contrast levels of 1.0%, 0.5%, and 0.3%. For each level, an image from the low-contrast (CTP515) module was displayed with fixed image settings (window=400, level=40). Three independent observers manually counted the number of targets visible in the image. The viewing conditions including the computer screen and location brightness, and physical environmental surroundings were kept constant.

2.2.2.5 Contrast-to-Noise Ratio (CNR)

To measure CNR, targets were selected in the 1.0% and 0.5% contrast regions in the low-contrast module, and two background targets of the same size (area = 90 mm^2) were selected adjacent to the targets, as shown in Figure 2-1. CNR was measured according to Equation 2-2 below:

Equation 2-2

$$CNR = \frac{2(C_0 - C_b)^2}{\sigma_0 - \sigma_b}$$

Where C_0 and σ_0 are the mean and standard deviation of the signal from the target, and C_b and σ_b are the mean and standard deviation of the signal from the background.

2.2.2.6 RED Calibration Curves

RED calibration curves for each aFOV were generated by plotting the measured CT number and the known RED obtained from the Catphan 504 phantom manual as shown in Table 2-1.

2.2.3 Statistical Analysis

All statistical analysis was performed using Prism 7.0 (GraphPad Software Inc., California, USA). Spearman correlation coefficient (ρ) was used to assess correlations between measured parameters and aFOV, and linear regression was used to assess the strength of significant correlations.

2.3 Results

2.3.1 Linearity

The measured CT number for all aFOV was within the range specified in the Catphan 504 manual for air, PMP, LDPE, polystyrene, and acrylic. CT number was underestimated at all aFOV settings for the two high-density inserts: Delrin and Teflon. All CT number measurements are shown in Table 2-1.

Measured CT number was significantly correlated with aFOV in Teflon ($\rho = 1.0$, $p = 0.02$, $r^2 = 0.92$), Delrin ($\rho = 1.0$, $p = 0.02$, $r^2 = 0.97$) and air ($\rho = 1.0$, $p = 0.02$, $r^2 = 0.83$) with a significantly non-zero slope (Teflon: $p = 0.01$, Delrin: $p = 0.002$, air: $p = 0.03$), as shown in Figure 2-2. Measured HU and aFOV were not significantly related for acrylic ($\rho = -0.7$, $p = 0.2$), polystyrene ($\rho = -0.05$, $p = 0.9$), LDPE ($\rho = 0.4$, $p = 0.5$), or PMP ($\rho = 0.8$, $p = 0.1$).

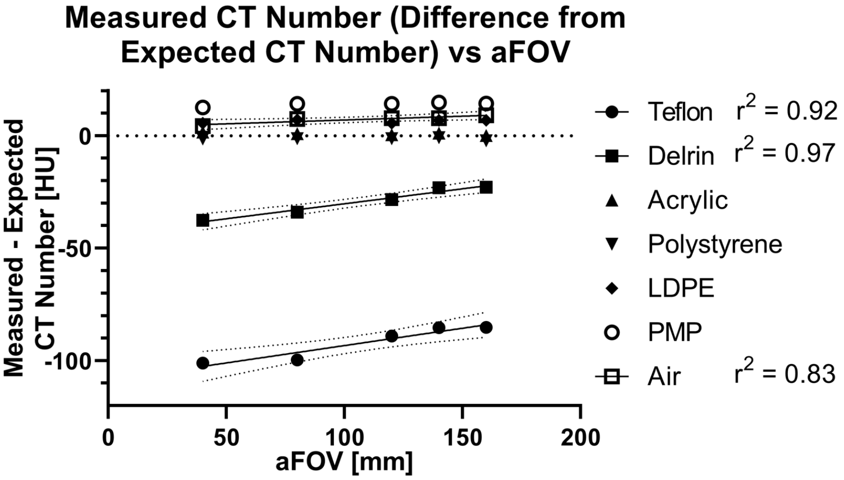

Figure 2-2 Difference between measured CT number in the sensitometry (CTP404) module and the expected CT number for each aFOV in the vCT images.

CT number and aFOV were not significantly correlated for: acrylic ($\rho = -0.7$, $p = 0.2$), polystyrene ($\rho = -0.05$, $p > 0.99$), LDPE ($\rho = 0.4$, $p = 0.5$), and PMP ($\rho = 0.8$, $p = 0.1$). Measured CT number was significantly correlated with aFOV for: Teflon ($\rho = 1.0$, $p = 0.02$, $r^2=0.92$), Delrin ($\rho = 1.0$, $p = 0.02$, $r^2=0.97$), and air ($\rho = 1.0$, $p = 0.02$, $r^2=0.83$).

2.3.2 Uniformity

The average CT number in each uniformity ROI across all aFOV images was (10.8 +/- 1.2) HU (A), (11.3 +/- 0.7) HU (B), (9.9 +/- 0.4) HU (C), (8.6 +/- 0.6) HU (D), and (9.9 +/- 0.5) HU (E). The mean measured CT number in all ROIs was within 2% (20 HU) of the expected value (0 HU). The maximum absolute difference in CT number between central and peripheral ROIs was (2.1 +/- 1.1) HU and < 5 HU for all measurements. The maximum absolute difference in CT number was not significantly correlated with aFOV ($r=0.235$, $p=0.7$), as shown in Figure 2-3.

2.3.3 Noise

Noise in the uniformity module for all aFOV values was 4.6 +/- 0.04 HU. Noise was not significantly correlated to aFOV ($\rho = -0.4$, $p=0.4$), as shown in Figure 2-3.

2.3.4 Low-Contrast Resolution

Three independent observers counted the number of targets in the low-contrast resolution module at contrast levels 1.0%, 0.5%, and 0.3% for each aFOV. The number of observed targets was 8.7 +/- 0.5 at 1.0%, 6.7 +/- 0.4 at 0.5%, and 0.33 +/- 0.4 at 0.3%, as shown in Figure 2-3. Number of observed targets was not significantly correlated with aFOV at 1.0% ($p = 0.067$), 0.5% ($p = 0.2$), or 0.3% ($p > 0.99$).

Contrast-to-noise ratio (CNR) was analyzed on the low-contrast resolution image (Figure 2-1) using the 15 mm targets in the 1.0% and 0.5% nominal contrast levels. The CNR at 1.0% was 5.2 +/- 0.9 and at 0.5% was 1.6 +/- 0.6. CNR was not significantly related to aFOV at 1.0% ($\rho = 0.4$, $p = 0.5$) or 0.5% ($\rho = -0.3$, $p = 0.7$), as shown in Figure 2-3.

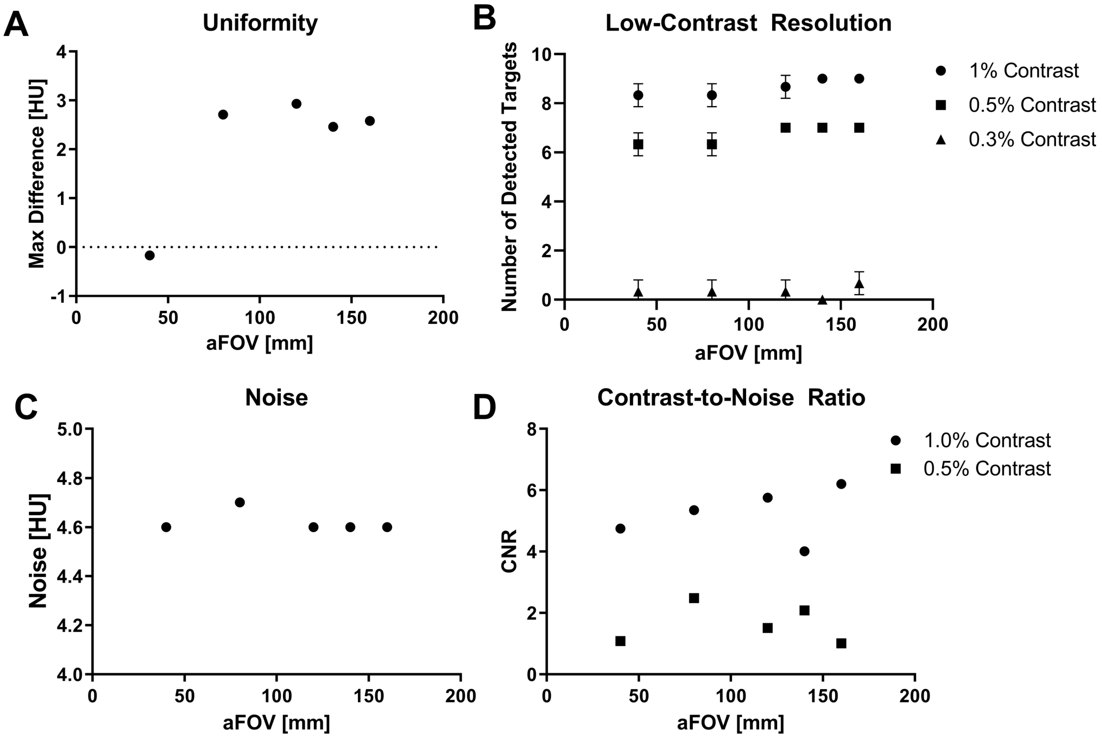

Figure 2-3 Correlation between image quality metrics and aFOV
(A) Maximum absolute difference [HU] between central and peripheral ROIs vs axial-field-of-view (aFOV) in the uniformity (CTP486) module ($\rho = 0.20$, $p = 0.78$). (B) Mean number of observed targets counted by three independent observers vs aFOV in the low-contrast (CTP515) module at contrast levels: 1.0% ($\rho = 0.95$, $p = 0.067$), 0.5% ($\rho = 0.87$, $p = 0.20$), and 0.3% ($\rho = 0.22$, $p > 0.99$). (C) Noise in the uniformity ROI vs aFOV in the uniformity (CTP486) module ($\rho = -0.35$, $p = 0.40$). (D) Contrast-to-noise ratios (CNR) in nominal contrast levels 1.0% and 0.5% vs aFOV in the low-contrast (CTP515) module ($\rho = 0.40$, $p = 0.52$ (1.0%), $\rho = -0.30$, $p = 0.68$ (0.5%)).

2.3.5 Longitudinal Directional Dependence

Horizontal profiles were compared from images taken at the center of the imaging bore of the scanner and at the outer edges of the bore at 160mm aFOV. The profiles were plotted as shown in Figure 2-4. No visible artifacts were identified, and there were no visible differences between the profiles. In the longitudinal profile, shown in Figure 2-4, there was no significant correlation between z position and measured CT number ($\rho = 0.04$, $p = 0.8$).

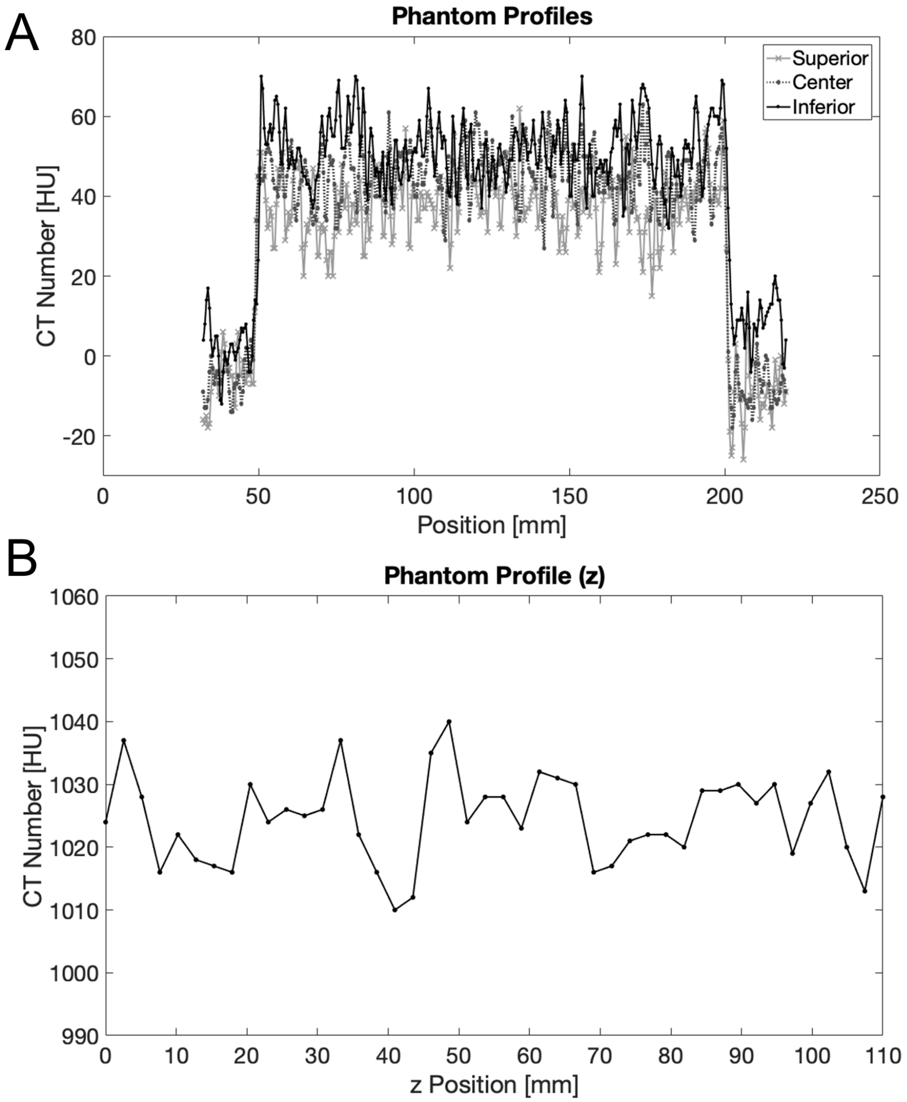

Figure 2-4 Horizontal and Vertical Catphan profiles
(A) Horizontal profiles of a uniform volume in the Catphan 504 phantom taken when the phantom was in a superior, center, and inferior position along the z-axis. These profiles appear to be consistent across the imaging volume. (B) A longitudinal profile of the uniform acrylic perimeter of the Catphan phantom. There is no significant relationship between measured CT number and position within the imaging bore ($\rho = 0.04$, $p = 0.8$).

Slices from the linearity module acquired at each aFOV value were also compared by visual inspection and by comparing line profiles through each image, as shown in Figure 2-5. There were no visible differences between the images from each aFOV

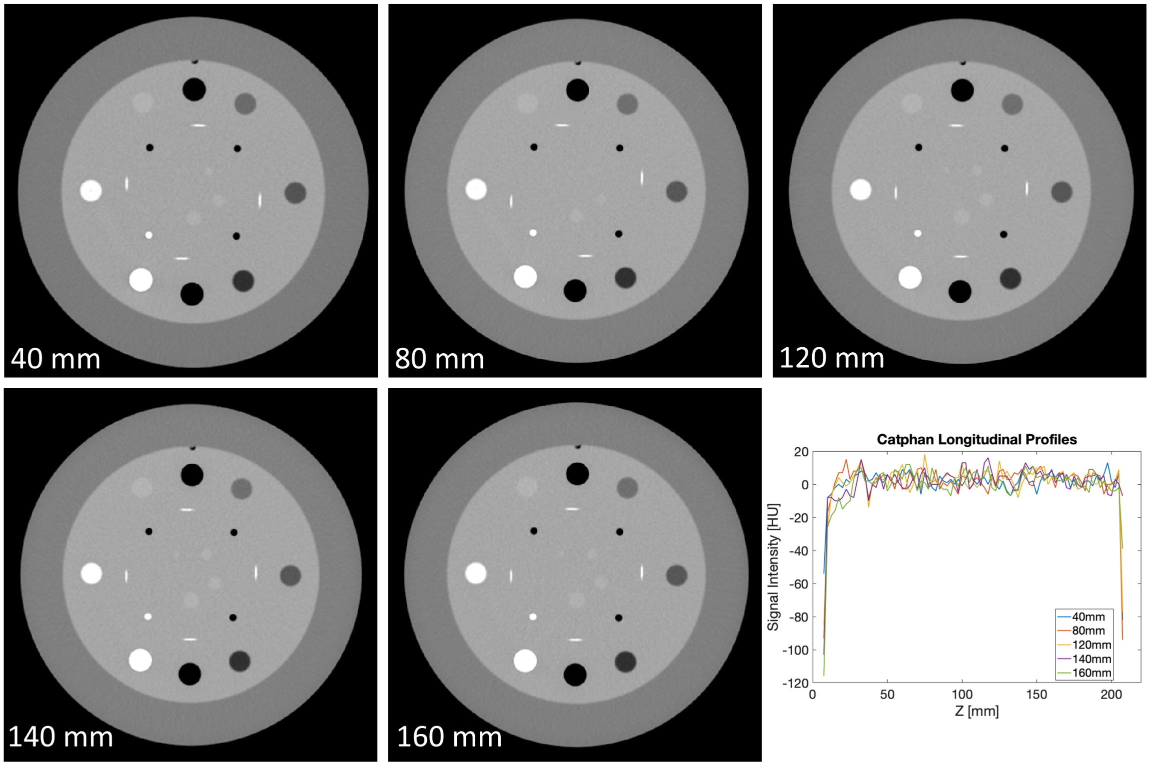

Figure 2-5 Comparison of images across aFOV
An axial slice of the linearity module in the Catphan 504 phantom acquired at each aFOV value tested in this study, and longitudinal profiles from each image. Visual comparison shows no obvious differences between the images.

2.3.6 RED Calibration

To perform dose calculations using a CT image, a relative electron density (RED) curve specific to the CT scanner and imaging parameters is required. We generated RED curves for each image set, shown in Figure 2-6.

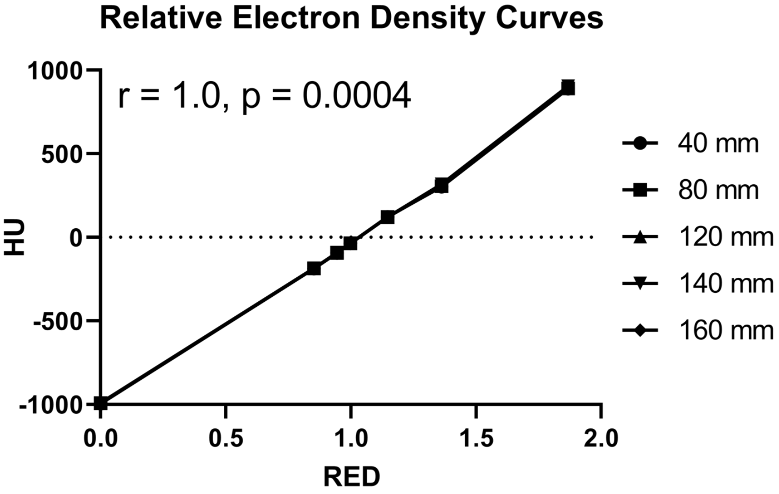

Figure 2-6 Relative electron density curves
Relative electron density (RED) calibration curves of measured CT number against Catphan 504 Phantom RED specifications for aFOV of 40 mm, 80 mm, 120 mm, 140 mm, and 160 mm on the vCT, and for the clinical CT. All RED curves were highly correlated ($\rho = 1.0$, $p = 0.0004$).

2.4 Discussion

In this paper, we assessed the utility of volumetric CT for radiotherapy simulation, treatment planning, and dose calculation. Volumetric CT is particularly useful for dynamic imaging techniques, such as contrast-enhanced imaging and 4D-CT, both of which are used in radiation treatment planning. Previous research has investigated the impact of volumetric imaging on these dynamic techniques, and has demonstrated that contrast-enhanced imaging is not negatively affected by cone-beam artifacts in volumetric imaging[9,12] and vCT can reduce the presence of respiratory motion artifacts in 4D-CT used for motion management[7]. These findings support the potential use of vCT for treatment planning.

We investigated the differences in linearity, RED, noise, and uniformity of images acquired using a 256-slice vCT scanner at different aFOV settings. The measurements were compared to the Catphan 504 phantom manual to determine if any artifacts were present that could impact the use of this scanner for CT simulation and radiation therapy planning.

We also imaged the phantom at different locations along the longitudinal axis of the scanner to test for cone-beam artifacts.

Our measurements demonstrated that measured CT number in acrylic, polystyrene, LDPE, PMP and air were consistent with the values expected from the Catphan manual (Table 1-1). However, measured CT number in Teflon and Delrin were underestimated for each axial coverage compared to these specifications. CT density is dependent on various factors including energy, scattering, and reconstruction algorithms[13,14]. The phantom specifications are defined over 94 different scanners and protocols, and the manual explicitly states that dramatic deviations from the specified HU range are not unusual[10]. In addition, a single scanner is known to produce variable results over time[15], and this variability is expected and accounted for in commissioning and quality assurance protocols. For treatment planning purposes, these variations will be accounted for with the relative electron density curve that is specific to the scanner. Therefore, while these deviations are statistically significant, we do not expect them to be clinically significant. We also observed that measured CT number in acrylic, polystyrene, LDPE, and PMP were not significantly correlated to aFOV, but Teflon, Delrin, and air increased significantly with aFOV. However, the relative change in CT number was small in all these cases (<5% for Delrin, and <1% for all lower density materials). These results suggest that most artifacts of increased aFOV are mitigated by hardware (ie. an anti-scatter grid) and algorithms to reduce artifacts in reconstructed images on the CT scanner. In addition, any remaining artifacts are so small that they are not considered clinically significant.

Uniformity measurements were in agreement with the recommended range[16] for each aFOV measured and were not significantly correlated with aFOV. Noise was also not correlated with aFOV. In our low-contrast resolution test there was strong agreement between our observers, and the number of targets identified was not significantly related to aFOV. CNR was analyzed for the 1.0% and 0.5% contrast modules and was also not significantly related to aFOV.

This study is limited by the fact that only phantom images were studied. Anthropomorphic phantoms or human images can also be compared between a clinical and volumetric scanner to confirm these findings. In addition, it is noteworthy that the relatively small bore size of this scanner (80 cm) limits its use for radiation therapy planning for some patients. Most clinical CT simulators are wide-bore scanners to accommodate a range of patient sizes and to include immobilization equipment, which can be very bulky. The small bore of the scanner in this study means that it likely cannot meet all CT simulation needs, as a large bore scanner will be needed for some patients. In the future, large-bore volumetric CT scanners could enable wider use of this technology in radiation oncology.

These results have significant implications for future clinical research projects. Dynamic contrast-enhanced CT imaging with a vCT scanner enables high-resolution functional mapping over a large anatomical volume. This advanced imaging technique can facilitate research projects such as functional avoidance treatment planning or studying imaging biomarkers of treatment response. The use of a vCT scanner for treatment planning facilitates direct access for researchers to volumetric imaging for research studies. Further work must be done to fully characterize the RED in clinical conditions before this system can be used clinically, in accordance with AAPM recommendations[16,17].

2.5 Conclusions

We imaged a Catphan phantom on a vCT scanner to assess image quality and generated RED calibration curves for increasing axial coverage up to 160 mm. CT linearity, uniformity, noise, and low-contrast resolution were within the expected range for most measurements, and deviations were determined to be not clinically significant. Our results suggest that most artifacts resulting from increased aFOV are mitigated by reconstruction techniques on the scanner, and remaining artifacts are considered clinically acceptable for radiation treatment planning. This study demonstrates that the vCT scanner can be used for CT simulation and radiotherapy treatment planning.

2.6 References

1. Chen Q-S, Weinhous MS, Deibel FC, Ciezki JP, Macklis RM. Fluoroscopic study of tumor motion due to breathing: Facilitating precise radiation therapy for lung cancer patients. *Med Phys*. 2001;28(9):1850-1856. doi:10.1118/1.1398037

2. Park JC, Park SH, Kim JH, et al. Liver motion during cone beam computed tomography guided stereotactic body radiation therapy. *Med Phys*. 2012;39(10):6431-6442. doi:10.1118/1.4754658

3. Yamamoto T, Langner U, Loo BW, Shen J, Keall PJ. Retrospective Analysis of Artifacts in Four-Dimensional CT Images of 50 Abdominal and Thoracic Radiotherapy Patients. *Int J Radiat Oncol Biol Phys*. 2008;72(4):1250-1258. doi:10.1016/j.ijrobp.2008.06.1937

4. Miyamae Y, Akimoto M, Sasaki M, Fujimoto T, Yano S, Nakamura M. Variation in target volume and centroid position due to breath holding during four-dimensional computed tomography scanning: A phantom study. *J Appl Clin Med Phys*. 2020;21(1):11-17. doi:10.1002/acm2.12692

5. Clements N, Kron T, Franich R, et al. The effect of irregular breathing patterns on internal target volumes in four-dimensional CT and cone-beam CT images in the context of stereotactic lung radiotherapy. *Med Phys*. 2013;40(2):21904. doi:10.1118/1.4773310

6. Sentker T, Schmidt V, Ozga A-K, et al. 4D CT image artifacts affect local control in SBRT of lung and liver metastases. *Radiother Oncol J Eur Soc Ther Radiol Oncol*. 2020;148:229-234. doi:10.1016/j.radonc.2020.04.006

7. Young HM, Lee T-Y, Gaede S. Respiratory Motion Characterization and Motion Artefact Reduction Using Volumetric 4-Dimensional Computed Tomography. *Med Phys*. 2019;46(6):E211-E211.

8. Coolens C, Breen S, Purdie TG, et al. Implementation and characterization of a 320-

slice volumetric CT scanner for simulation in radiation oncology. *Med Phys*. 2009;36(11):5120-5127. doi:10.1118/1.3246352

9. Hara T, Niwa S, Urikura A, et al. Assessment of longitudinal beam property and contrast uniformity for 256- and 320-row area detector computed tomography scanners in the 160-mm nonhelical volume-acquisition mode. *J Appl Clin Med Phys*. 2019;20(8):164-170. doi:10.1002/acm2.12670

10. The Phantom Laboratory. *Catphan504 Manual*. Salem, NY; 2013. https://www.phantomlab.com/additional-catphans.

11. Yushkevich PA, Piven J, Hazlett HC, et al. User-guided 3D active contour segmentation of anatomical structures: significantly improved efficiency and reliability. *Neuroimage*. 2006;31(3):1116-1128. doi:10.1016/j.neuroimage.2006.01.015

12. So A, Imai Y, Nett B, et al. Technical Note: Evaluation of a 160-mm/256-row CT scanner for whole-heart quantitative myocardial perfusion imaging. *Med Phys*. 2016;43(8):4821. doi:10.1118/1.4957389

13. Birnbaum B a, Hindman N, Lee J, Babb JS. Multi-detector row CT attenuation measurements: assessment of intra- and interscanner variability with an anthropomorphic body CT phantom. *Radiology*. 2007;242(1):109-119. doi:10.1148/radiol.2421052066

14. Vergalasova I, McKenna M, Yue NJ, Reyhan M. Impact of computed tomography (CT) reconstruction kernels on radiotherapy dose calculation. *J Appl Clin Med Phys*. September 2020. doi:10.1002/acm2.12994

15. Roa AM a, Andersen HK, Martinsen ACT. CT image quality over time: comparison of image quality for six different CT scanners over a six-year period. *J Appl Clin Med Phys*. 2015;16(2):4972. doi:10.1120/jacmp.v16i2.4972

16. Samei E, Bakalyar D, Boedeker KL, et al. Performance evaluation of computed

tomography systems: Summary of AAPM Task Group 233. *Med Phys*. 2019;46(11):e735-e756. doi:10.1002/mp.13763

17. Mutic S, Palta JR, Butker EK, et al. Quality assurance for computed-tomography simulators and the computed-tomography-simulation process: report of the AAPM Radiation Therapy Committee Task Group No. 66. *Med Phys*. 2003;30(10):2762-2792. doi:10.1118/1.1609271

CHAPTER 3

3 Reduction of respiratory motion artifacts using volumetric four-dimensional computed tomography

Four patients with non-small cell lung cancer and a motion phantom underwent clinical 4D-CT imaging on a conventional scanner and 4D-CT on a volumetric CT scanner (v4D-CT) which was used to simulate a conventional acquisition (sim4D-CT). The clinical 4D-CT phantom contours were significantly larger than the v4D-CT contours, suggesting an over-estimation of target size, and the differences between clinical contours in patient clinical 4D-CT and v4D-CT were significantly correlated with the respiratory phase, suggesting that motion artifacts contributed to this difference. These results demonstrate that v4D-CT reduces motion artifacts, decreasing contour variability throughout the respiratory cycle.

The contents of this chapter are in preparation for submission to the Journal of Medical Physics by: HM Young, J Kempe, TY Lee, and S Gaede.

3.1 Introduction

Radiation treatment planning for non-small cell lung cancer (NSCLC) is often complicated by the respiratory motion of the tumors and surrounding organs at risk (OARs). To ensure sufficient dose is delivered to the tumor, and OARs are spared, motion management techniques are necessary. Four-dimensional computed tomography (4D-CT) is an important part of the treatment planning process in which the motion of the tumor is quantified, and anatomical images for treatment planning are acquired. However, 4D-CT images are prone to artifacts caused by irregular breathing motion[1]. These artifacts have a negative impact on contouring of the target and surrounding organs at risk[2–7] and have even been shown to reduce local control after stereotactic radiation therapy to the lung or liver[8].

Various methods have been developed to mitigate the effects of irregular breathing on 4D-CT image quality. Some methods use improved image sorting and reconstruction algorithms[9,10]. This approach is limited due to a lack of image data, in an effort to limit the radiation dose from imaging. Other methods use motion tracking to improve data acquisition on the scanner, by turning off the x-ray beam when breathing motion is outside the expected range[11]. This method has been shown to be feasible for clinical use and reduces visibly obvious motion artifacts[12,13]. However, artifacts remain in some images. Other studies have investigated methods which require a significantly higher imaging dose, such as an oversampling acquisition[14]. This method reduces motion artifacts, but the increased imaging dose limits its applicability.

Volumetric CT scanners can overcome these limitations by implementing a wide-area detector (160mm axial field-of-view) so a large volume can be imaged in a single rotation. Therefore, a treatment planning 4D-CT scan can be acquired in two to three couch positions, so variation in respiratory motion between slices is limited. In addition, these scanners employ a faster rotation time (0.28s) than many clinical CT scanners to date, which minimizes blurring due to motion. This technology may enable the acquisition of 4D-CT with few or no respiratory motion artifacts if the patient is positioned such that the motion of the target is captured within the 160 mm aFOV. This would enable more accurate contouring, which can increase the dose delivered to the target, and decrease the dose delivered to surrounding healthy tissue. In addition, this technology will enable the acquisition of dynamic functional imaging across a large volume, which can be used to study functional properties of the tumor or surrounding tissue before treatment, or to assess treatment response.

The objective of this study is to quantify the reduction in respiratory motion artifacts by using a volumetric CT scanner. To control for daily variations in patient breathing, we also simulated a conventional 4D-CT acquisition using volumetric CT images to induce motion artifacts. The images were compared visually, and quantitative analysis of contours of a phantom target and patient OARs was performed across image types and respiratory phases.

3.2 Materials and Methods

3.2.1 Image Acquisition

3.2.1.1 Phantom Study

For this study, we used the Quasar Programmable Respiratory Motion Phantom (Modus Medical Devices, London Canada), shown in Figure 3-1. This phantom consists of an acrylic thorax-shaped phantom containing a customized moving cedar insert, which contains 4 polystyrene spheres (with known diameter). The largest polystyrene sphere also contains implanted gold VISICOIL markers (IZI Medical, Owings Mills, USA). The phantom was programmed to move with 3 different motion traces: (1) Sinusoidal motion (20 mm peak-to-peak amplitude, 4.0 s period), (2) a patient-derived motion trace demonstrating a baseline drift artifact (initial amplitude 15 mm, maximum drift 12.8 mm), and (3) a patient-derived motion trace demonstrating an irregular amplitude artifact (minimum amplitude = 5 mm, maximum amplitude = 25 mm). The moving phantom was imaged on a GE Revolution 256-slice volumetric CT scanner (GE Healthcare, Milwaukee, USA), and on a Philips Brilliance Big Bore 16-slice CT simulator (Philips Healthcare, Fitchburg, USA). The image acquisition details are shown in Table 3-1.

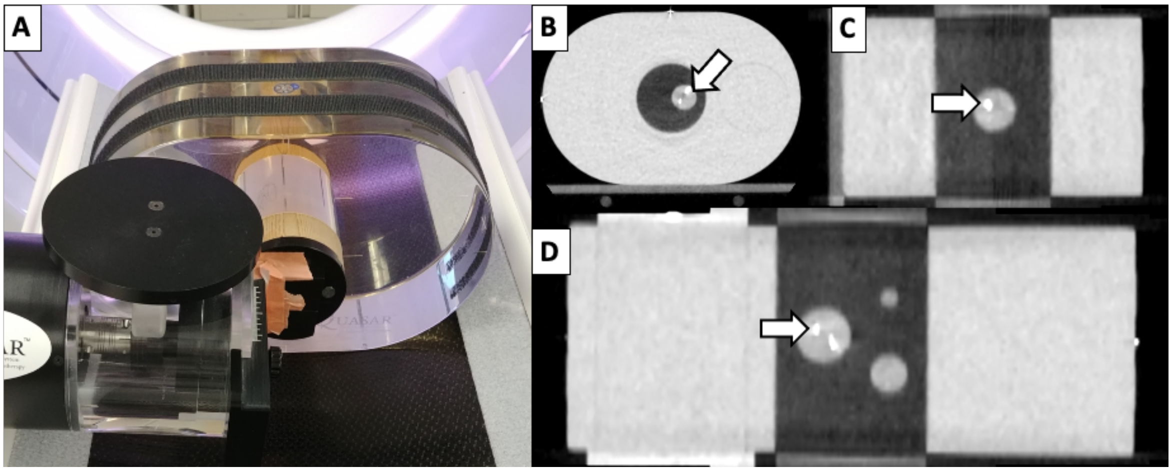

Figure 3-1 Quasar programmable respiratory motion phantom used for all phantom imaging.
(A) Photo of the Quasar phantom set up on the bed of the volumetric CT scanner before imaging. (B) Axial, (C) Sagittal, and (D) Coronal slices from a single volumetric CT image of the phantom. No marker block was used for this scan, motion tracking and phase binning was performed using the VISICOIL marker indicated by the arrows in (B), (C), and (D).

3.2.1.2 NSCLC Patient Study

Four NSCLC patients received standard of care clinical 4D-CT simulation on a Philips16-slice CT scanner and received a free breathing CT scan on the research 256-slice CT scanner. The image acquisition details for both scanners are shown in Table 3-1. On the clinical scanner, chest motion was captured simultaneously during image acquisition by the Varian RGSC system (Varian Medical Systems, Palo Alto, USA) and used to reconstruct the images into 10 breathing phases. The volumetric 4D-CT research scan was acquired as part of another research study (NCT03416972) and included an iodine-based contrast administered approximately 10 seconds after the beginning of the dynamic CT scan.

Table 3-1 Scan parameters for all image acquisitions

Scanner	Mode	Rotation Speed [s]	aFOV [mm]	Voltage [kV]	Current [mA]	Scan time [s]
vCT	cine	0.28	160	120	100	10
vCT	cine	0.28	160	120	10	45
Clinical	helical	0.5	24	120	97	30-120

3.2.1.3 Simulated Conventional 4D-CT from Volumetric CT Images

The volumetric images that were acquired using an aFOV of 160mm were retrospectively resampled and sorted to simulate image acquisition with a narrow aFOV of 20mm and a cine-mode acquisition using in-house software, as shown in the schematic in Figure 3-2. First, a semi-automated edge detection method was used to extract diaphragm motion from the images. An edge detection filter was applied to a manually defined region of interest, and thresholding was used to identify the curve of the diaphragm. The peak of this curve was used to define diaphragm position. This motion was used as a surrogate for the external chest motion data to simulate the respiratory trace captured by the Varian RGSC system in the clinical 4D-CT scan. The diaphragm position data was interpolated using spline interpolation in MATLAB, and end-inhale phases were manually identified in this motion trace. The volumetric images were sorted by phase-based binning using the internal motion data. To mimic cine-mode acquisition using 8 s per couch position and a 20mm aFOV, only the images acquired within an 8 s time window at a simulated couch position were used and the remainder discarded. To ensure there was enough time series data, we looped from the last acquired imaging set to the first acquired imaging set. No slices were duplicated in this process since the first 40s of the simulated scan contained only slices from the superior half of the image dataset and the remaining scan contained only slices from the inferior half of the image dataset. From theses remaining images, volumes were reconstructed at 10 respiratory phases using in-house software to create a simulated conventional 4D-CT (sim4D-CT).

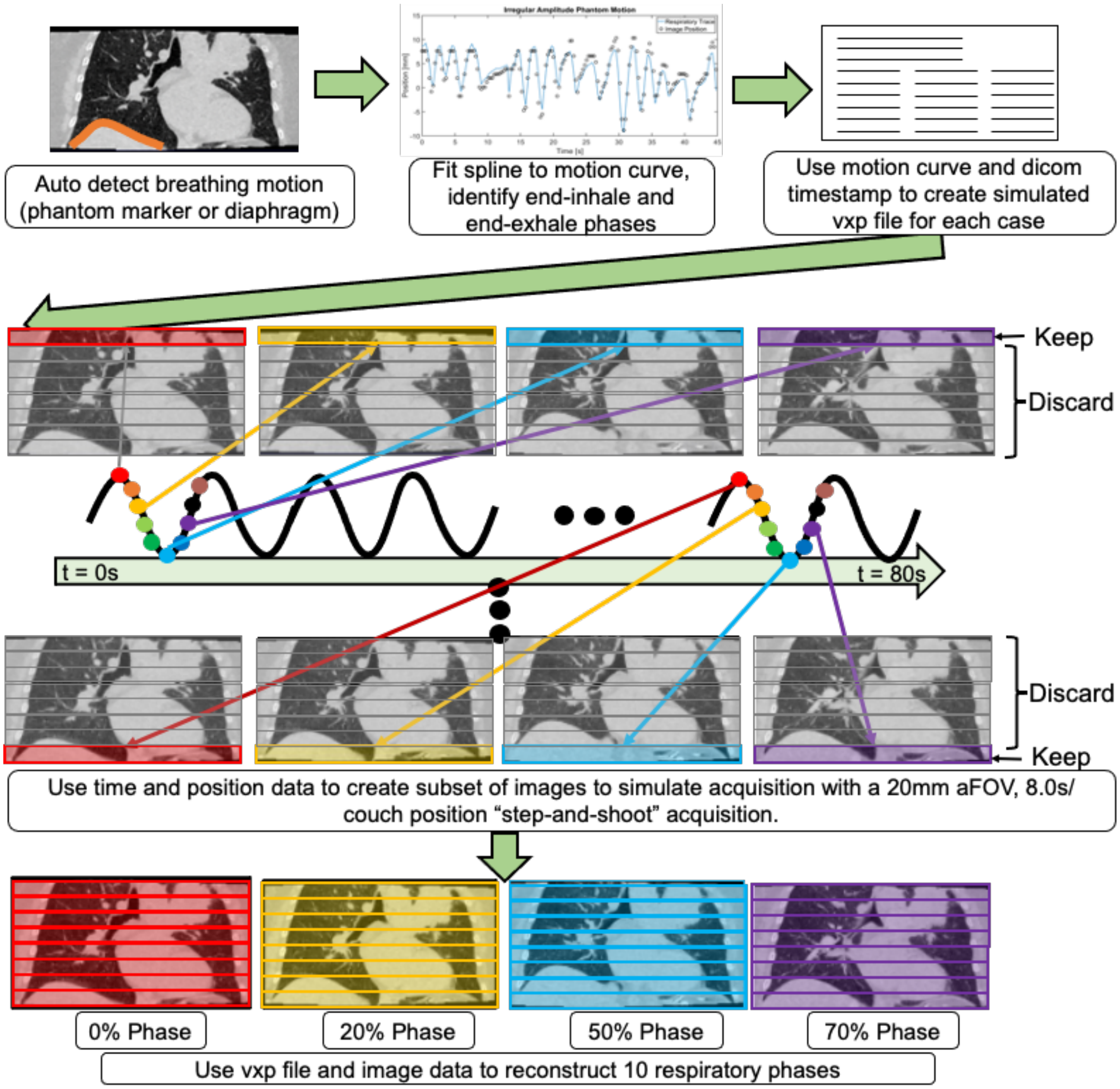

Figure 3-2 Workflow of method used to generate sim4D-CT images from volumetric CT images.

3.2.2 Image Analysis

3.2.2.1 Phantom Study

The largest polystyrene sphere implanted in the phantom was manually segmented on every phase of each 4D-CT image set ITKSnap[15], and the volume of each contour was measured. The mean and standard deviation of these volumes were compared between scan types using a one-way ANOVA and Bartlett's test. These measured volumes were compared to the known volume of 1.41 x 10^4 mm^3. Any contour which was within 5% of the known volume was deemed acceptable, and those which deviated by more than 5% were considered unacceptable. Then, using only the v4D-CT images, a thresholding method was used to automatically detect the motion of the implanted gold marker in the phantom throughout the scan. This measured position was compared to the input motion trace at each timepoint using Pearson correlation for each motion type. The images were also assessed qualitatively for differences between each scan type.

3.2.2.2 Patient Study

First, the images were assessed qualitatively for differences between each scan type. Contours for organs at risk (left and right lung, bronchi, trachea, and spinal cord) were delineated using a commercial deep-learning based auto-contouring program (Limbus AI, Regina, Canada) with some manual corrections on all phases of all 4D-CT images. The heart was not included in this study because the cardiac motion presents an additional source of artifacts. For each phase and each patient, the clinical and sim4D-CT images were rigidly registered to the v4D-CT image in 3DSlicer[16] (version 4.10.2). The contours for each image were compared using the Dice coefficient and mean Hausdorff distance with the Segment Comparison tool in 3DSlicer. For long tube-like structures, including the bronchial tree and spinal cord, only the mean Hausdorff distance was calculated, as it is the more appropriate metric for that type of structure.

3.2.3 Statistical Analysis

Phantom contours volumes were compared across the three scan types using a one-way ANOVA and Dunnett's multiple comparisons test. Bartlett's test was used to test if the standard deviation of each measurement was different across the three scan types.

To evaluate the changes in patient contours as a function of phase, which is cyclical and often measured as a percentage of the cycle, the measure of phase was converted as shown in Equation 3-1 below to establish a linear relationship.

Equation 3-1

$$Phase_{sin} = sin(Phase)$$

The highest value of $Phase_{sin}$ corresponds to the end-exhale and early inhale phase of the respiratory cycle and the lowest value corresponds to the mid-exhale phase. Relationships between Mean Hausdorff distance and Dice coefficient were compared to phase using the Pearson correlation coefficient. All statistical tests were performed using GraphPad Prism (version 9.3.1).

3.3 Results

3.3.1 Phantom Study

3.3.1.1 Qualitative Results

The clinical 4D-CT, v4D-CT, and sim4D-CT images of the Quasar respiratory motion phantom were all compared qualitatively for the presence of visually obvious motion artifacts. A subset of images showing this comparison is shown in Figure 3-3. In the v4D-CT images, no visually obvious motion artifacts were visible in any of the images. However, in the sim4D-CT and v4D-CT images there were several motion artifacts seen in each scan. In the Baseline Drift and Irregular Motion scans there were artifacts which distorted the size and shape of the spherical inserts, mostly in the mid-inhale and mid-exhale phases of the respiratory cycle. Artifacts were not visible at the end-exhale phase. and in the sinusoidal motion scan there was primarily blurring visible in the mid-inhale and mid-exhale phases.

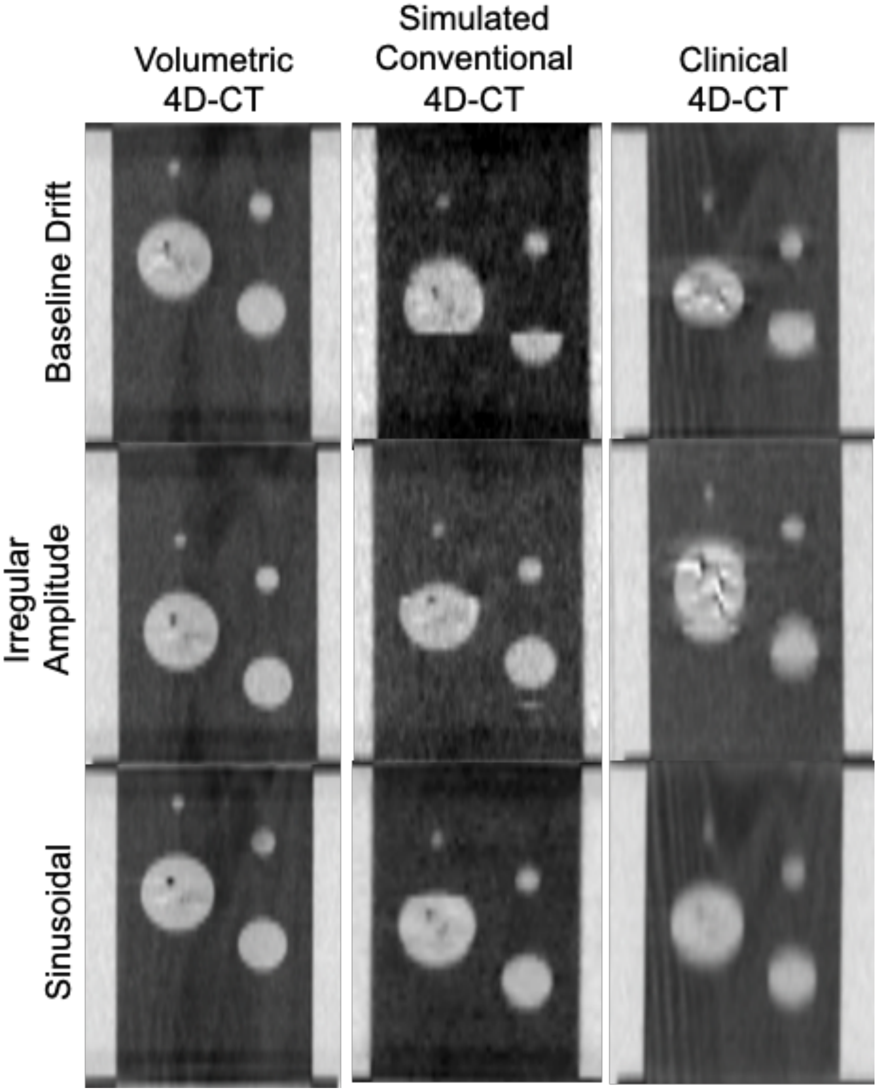

Figure 3-3 Images of the Quasar Motion Phantom from clinical and volumetric 4D-CT. Images of Quasar respiratory motion phantom from v4D-CT (first column), sim4D-CT (second column) and clinical 4D-CT (third column) scans under baseline drift (first row) irregular amplitude (second row) and sinusoidal (third row) motion conditions. All images are mid-exhale images taken from a 4D-CT scan. While there were no visually obvious motion artifacts present in the v4D-CT images, there were visible motion artifacts in the sim4D-CT and clinical 4D-CT images under all motion conditions.

3.3.1.2 Quantitative Results

For the volumetric CT scan under all motion conditions, the contours were within 5% of the known volume of the phantom sphere. For the simulated clinical 4DCT images under all motion conditions, only 30% of the contours were within 5% of the known volume.

47% of the contours were above the known volume, and the remaining 23% were below. For the clinical scanner under all motion conditions, only 7% of the contours were within 5% of the known volume. 80% of contours were above the known volume, and the remainder were below the known volume.

There was not a significant difference found between the mean volumes measured in the baseline drift scan, but there were significant differences found in the irregular amplitude ($p = 0.02$) and sinusoidal ($p < 0.0001$) scans. Bartlett's test showed significantly different standard deviations between the groups for baseline drift ($p < 0.0001$), irregular amplitude ($p < 0.0001$), and sinusoidal motion ($p = 0.002$). These results are shown in Figure 3-4.

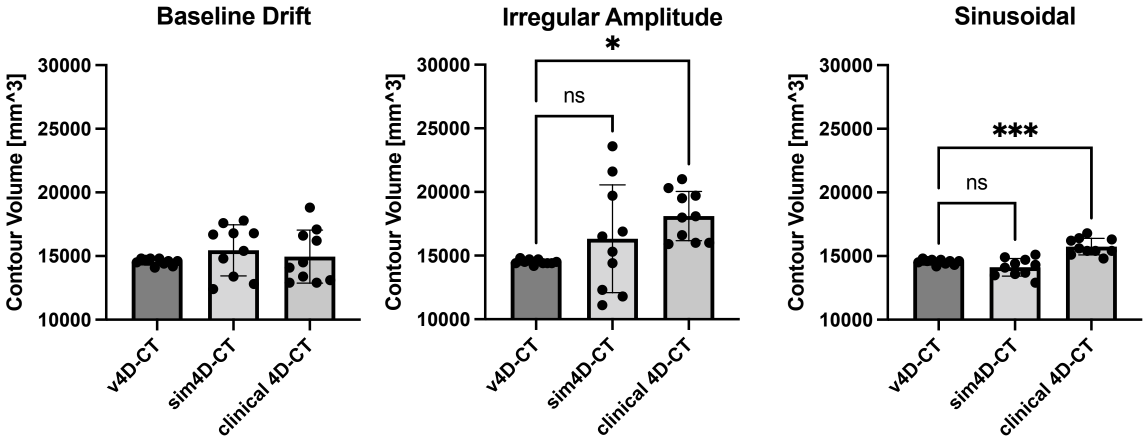

Figure 3-4 Phantom contour volume across motion conditions and scan type.
Contour volume of a spherical target in the Quasar respiratory motion phantom across three motion conditions using v4D-CT, sim4D-CT and clinical 4D-CT measured at each respiratory phase. There was no significant difference between mean measured volume between scan types under baseline drift motion. There was a significant difference in mean volume between v4D-CT and clinical 4D-CT under irregular amplitude ($p = 0.02$) and sinusoidal motion conditions ($p < 0.0001$), but not between v4D-CT and clinical 4D-CT. There was a significant difference in the standard deviation of the measures across scan types for all three motion conditions, resulting in the high variation in contour volume seen in the sim4D-CT and clinical 4D-CT plots above.

The measured position of the gold marker in the v4D-CT images was highly correlated with the known phantom position for all motion patterns (baseline drift: r=0.997, p<.0001; irregular amplitude: r=0.997, p<.0001; sinusoidal: r=0.998, p<.0001). These results are shown in Figure 3-5. Both the size and motion of the sphere were determined with high accuracy in all v4D-CT scans.

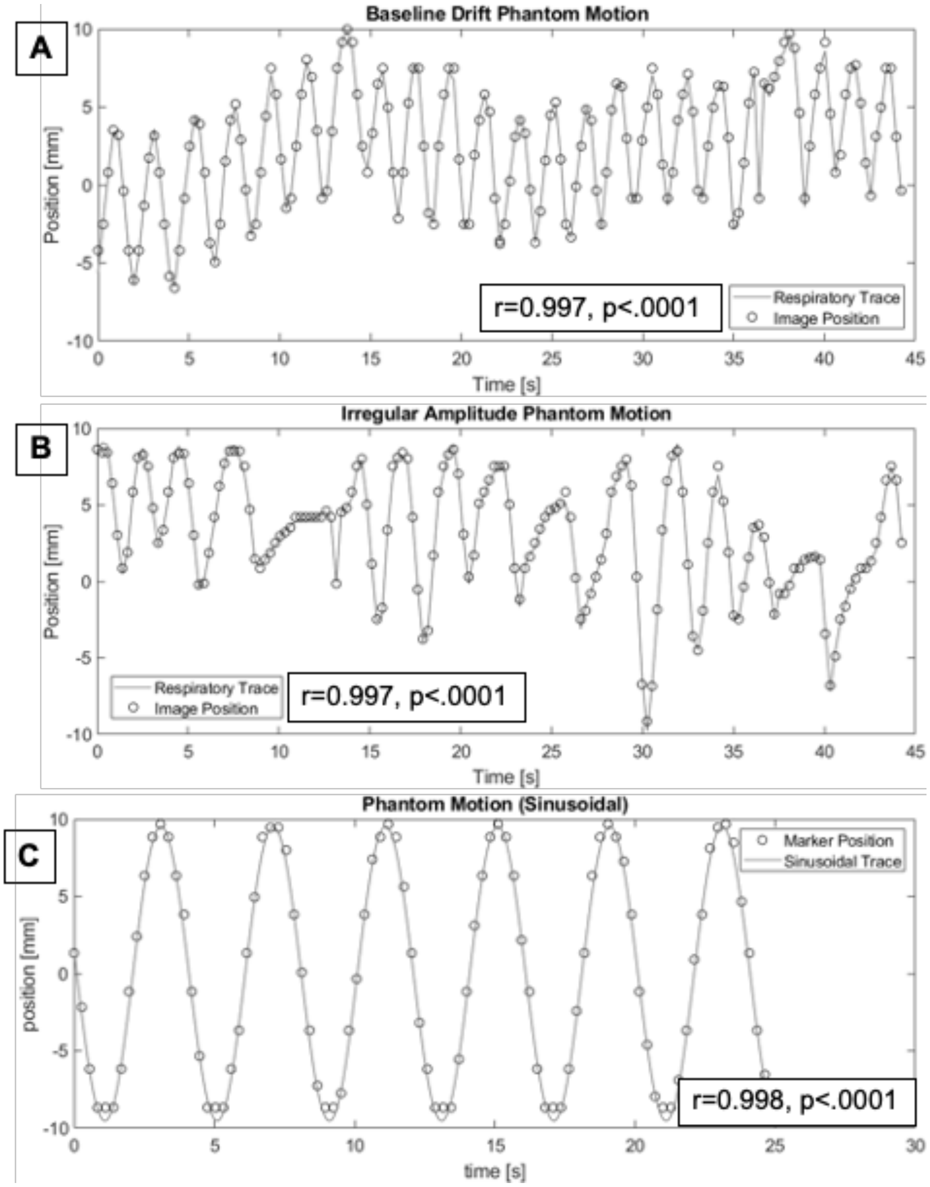

Figure 3-5 Phantom motion input and measured phantom position in v4D-CT images. Plots of measured marker position taken from vCT images of the motion phantom (markers), plotted with the input motion trace to the phantom (solid line). Correlation between these two measurements is given for (A) Baseline Drift scan ($r = 0.997$, $p < 0.0001$), (B) Irregular Motion scan ($r = 0.997$, $p < 0.0001$), (C) Sinusoidal scan ($r = 0.998$, $p < 0.0001$).

3.3.2 Patient Study

3.3.2.1 Qualitative Results

For all patients, there were no visually obvious motion artifacts present in the volumetric 4D-CT images. Motion artifacts were seen in at least one phase of the sim4D-CT images and clinical 4D-CT images for all patients. These were most commonly seen in mid-inhale and mid-exhale images, and in these four patients no motion artifacts were observed in the end-exhale image. Representative images for each imaging type for each patient are shown in Figure 3-6. Within a single patient, artifacts in sim4D-CT images and artifacts in the corresponding phase of the clinical 4D-CT often occur in the same anatomical region. It should be noted that the entire iodine contrast-enhanced image series from the v4D-CT imaging was used to generate the sim4D-CT images. This means that the contrast is visible in some of the sim4D-CT images.

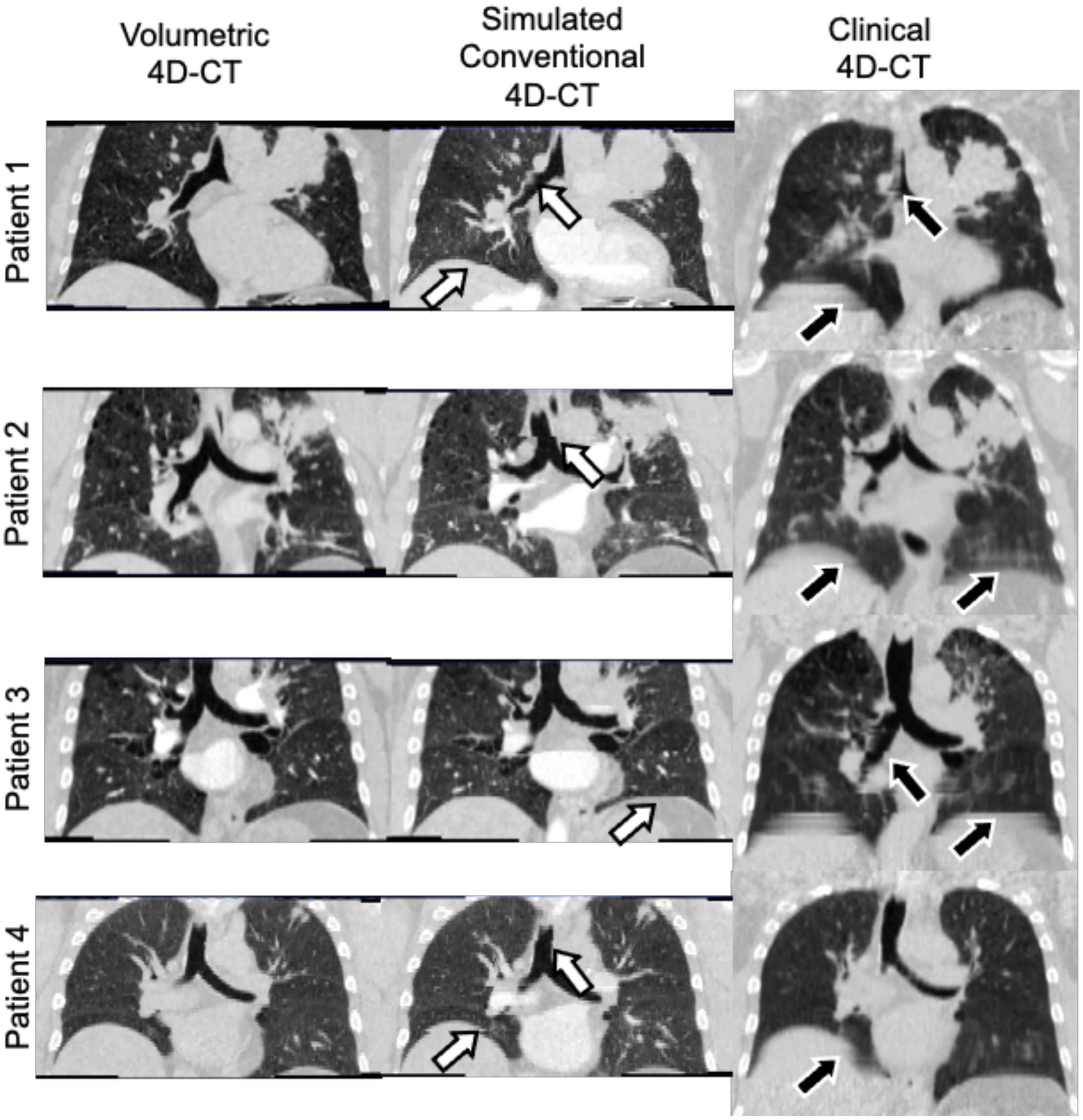

Figure 3-6 Mid-exhale images from each patients' 4D-CT images
Each column contains the images from a single patient, as labelled. The volumetric 4D-CT images (top row) have no visible blurring or motion artifacts. The simulated conventional 4D-CT images (center row) contain some motion artifacts, indicated by white arrows. The clinical 4D-CT images (bottom row) contain several motion artifacts, indicated by black arrows.

3.3.2.2 Quantitative Results

When comparing the OAR contours between the v4D-CT images and the clinical 4D-CT images, the agreement between contours of the same organ varied throughout the breathing cycle. Contours were compared to $\text{Phase}_{\text{sin}}$ such that the highest value of $\text{Phase}_{\text{sin}}$

corresponds to the end-exhale and early inhale phase of the respiratory cycle and the lowest value corresponds to the mid-exhale phase. There was a significant correlation between Phase$_{\text{sin}}$ and the mean Hausdorff distance between the bronchial tree (r = -0.84, p = 0.002) and trachea (r = -0.86, p = 0.001) contours. There was no significant correlation between Phase$_{\text{sin}}$ and mean Hausdorff distance between the spinal cord contours (r = 0.04, p = 0.9), as the spinal cord undergoes very little respiratory motion in the supine position. There was also a significant correlation between Phase$_{\text{sin}}$ and the Dice coefficients and mean Hausdorff distance between the right lung (r = 0.95, p < 0.0001; r = -0.90, p = 0.0004) contours. There was no significant relationship between Phase$_{\text{sin}}$ and measures of the left lung contours. These results are shown in Figure 3-7.

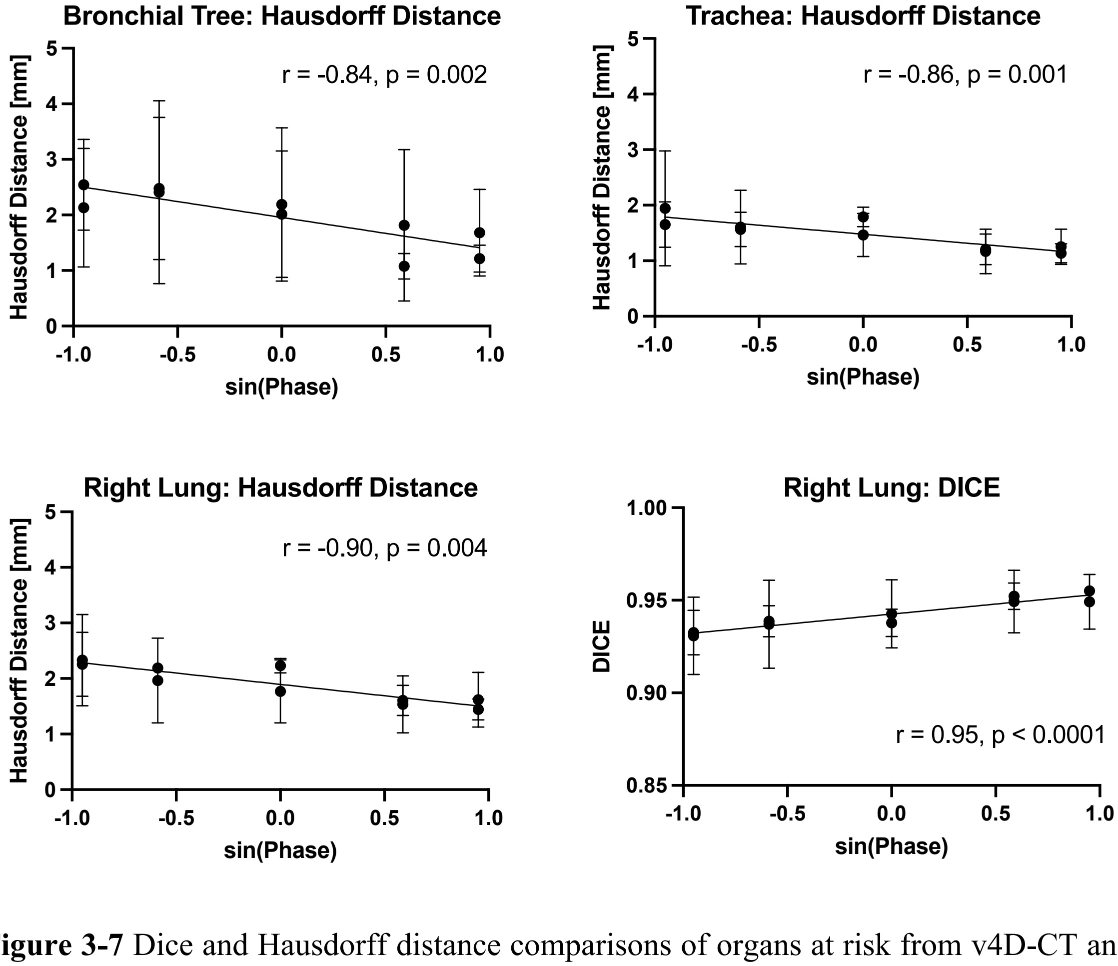

Figure 3-7 Dice and Hausdorff distance comparisons of organs at risk from v4D-CT and clinical 4D-CT scans of four patients with non-small cell lung cancer.
Mean Hausdorff distance between the bronchial tree, trachea, and right lung were significantly correlated to sin(Phase). The Dice coefficient between the right lung contours was also significantly correlated to sin(Phase).

When comparing OAR contours between the v4D-CT images and the sim4D-CT images, the measures showed the same trends relative to respiratory phase, but the correlations were weak and were not statistically significant.

3.4 Discussion

In the sim4D-CT and clinical 4D-CT phantom images, the observed motion artifacts distorted the size and shape of the spherical markers. This finding was expected, as it has been clearly documented in previous studies that motion artifacts can significantly impact the contouring of the target in radiation therapy[2–6]. This idea is strengthened by the phantom contour results, where v4D-CT images produced accurate volumetric measurements of the spherical marker while the sim4D-CT and clinical 4D-CT images did not. In addition, the marker motion in the v4D-CT images was highly correlated to the known motion. This demonstrates clearly that the size and motion of a potential target can be clearly measured using v4D-CT while clinical 4D-CT is known to perform poorly in this task.

The impact of motion artifacts on contouring was again demonstrated in the patient contour results, as agreement between OAR contours between v4D-CT and clinical 4D-CT scans varied by respiratory phase. This is likely due to the increased presence of artifacts at mid-inhale and mid-exhale phases. There was no significant correlation between measures of v4D-CT and sim4D-CT with phase. This may be because fewer artifacts were present in the sim4D-CT images, and the inherent relationship between the images as they were created from the exact same data set. In addition, the faster rotation speed of the volumetric scanner results in decreased blurring due to motion, and this factor is present in both the v4D-CT and sim4D-CT images.

The reduced variability of contour volumes in v4D-CT relative to clinical 4D-CT demonstrated here suggests that v4D-CT can enable more precise dose calculations and delivery of radiation to the target. In addition, motion artifacts can impact organ-at-risk contouring, radiation dose calculations, matching with cone-beam CT (CBCT) for image guidance. The reduction of motion artifacts shown in this study may have implications for clinical and research applications of dynamic CT imaging.

Artifacts also have a significant impact on CT ventilation[17] imaging which is currently used in clinical trials to map high- and low-functioning regions of the lung for functional avoidance treatment planning. The current high rate of artifacts in clinical 4D-CT is one reason that there is ongoing debate as to whether functional-guided radiation therapy should be used clinically[18]. Future work in this area will include direct comparison on CT ventilation maps derived from clinical, volumetric, and sim4D-CT images.

It should be noted that in the simulated 4D-CT images, an aFOV of 20 mm was used, as it was the closest match to the clinical 4D-CT scanner and allowed us to sample the entire aFOV of the vCT images. However, the clinical 4D-CT images were collected with an aFOV of 24 mm, so the two image sets cannot be exactly compared. In addition, the v4D-CT and sim4D-CT images were acquired with a 0.28s rotation speed with a cine mode acquisition and were reconstructed in image space. The clinical 4D-CT images were acquired with a 0.5s rotation speed with a slow helical acquisition and were reconstructed in sinogram space. The effects of the different rotation speed, aFOV, and acquisition and reconstruction type cannot be separated in this study. Despite this, we still demonstrate many similar motion artifact distributions between each patient's clinical 4D-CT and sim4D-CT. In addition, the increase in motion artifacts present in the sim4D-CT scan as compared to the volumetric scan clearly demonstrates the utility of volumetric CT for generating artifact-free 4D-CT scans.

It should also be noted that there are limitations which may inhibit the use of volumetric CT in radiation treatment planning in the short term, as outlined in previous work done by this group[19]. Volumetric CT scanners are significantly more expensive than a conventional CT simulator (usually with 16-64 slice detectors, as compared to the 256-slice detector in a volumetric scanner), and currently have a narrower bore than is typically used to accommodate large patients and immobilization devices in CT simulation. These limitations may change over time but are currently relevant considerations to weigh against the demonstrated benefits of volumetric CT scanners.

3.5 Conclusion

4D-CT images acquired using a volumetric scanner contained no visibly obvious motion artifacts, which were present in all clinical 4D-CT images of the phantom under irregular motion and all patients. In the phantom images, the size, shape, and motion of the spherical targets were measured with lower variability in the v4D-CT images than the clinical 4D-CT images. In the patient images, agreement between v4D-CT and clinical 4D-CT images was significantly correlated to the phase of the respiratory cycle being examined. Artifact reduction using v4D-CT significantly improves target and OAR contouring, which may impact patient outcomes.

3.6 References

1. Yamamoto T, Langner U, Loo BW, Shen J, Keall PJ. Retrospective Analysis of Artifacts in Four-Dimensional CT Images of 50 Abdominal and Thoracic Radiotherapy Patients. *Int J Radiat Oncol Biol Phys*. 2008;72(4):1250-1258. doi:10.1016/j.ijrobp.2008.06.1937

2. Persson GF, Nygaard DE, Brink C, et al. Deviations in delineated GTV caused by artefacts in 4DCT. *Radiother Oncol*. 2010;96(1):61-66.

3. Louie A V, Rodrigues G, Olsthoorn J, et al. Inter-observer and intra-observer reliability for lung cancer target volume delineation in the 4D-CT era. *Radiother Oncol*. 2010;95(2):166-171. doi:https://doi.org/10.1016/j.radonc.2009.12.028

4. Fredberg Persson G, Nygaard DE, af Rosenschöld PM, et al. Artifacts in Conventional Computed Tomography (CT) and Free Breathing Four-Dimensional CT Induce Uncertainty in Gross Tumor Volume Determination. *Int J Radiat Oncol*. 2011;80(5):1573-1580. doi:https://doi.org/10.1016/j.ijrobp.2010.10.036

5. Wikström KA, Isacsson UM, Pinto MC, Nilsson KM, Ahnesjö A. Evaluation of irregular breathing effects on Internal Target Volume definition for lung cancer radiotherapy. *Med Phys*. March 2021. doi:10.1002/mp.14824

6. Clements N, Kron T, Franich R, et al. The effect of irregular breathing patterns on internal target volumes in four-dimensional CT and cone-beam CT images in the context of stereotactic lung radiotherapy. *Med Phys*. 2013;40(2):21904. doi:10.1118/1.4773310

7. Lambrecht M, Sonke J-J, Nestle U, et al. Quality assurance of four-dimensional computed tomography in a multicentre trial of stereotactic body radiotherapy of centrally located lung tumours. *Phys imaging Radiat Oncol*. 2018;8:57-62.

8. Sentker T, Schmidt V, Ozga A-K, et al. 4D CT image artifacts affect local control in SBRT of lung and liver metastases. *Radiother Oncol J Eur Soc Ther Radiol*

Oncol. 2020;148:229-234. doi:10.1016/j.radonc.2020.04.006

9. Pan T, Sun X, Luo D. Improvement of the cine-CT based 4D-CT imaging. *Med Phys*. 2007;34(11):4499-4503.

10. Carnes G, Gaede S, Yu E, Van Dyk J, Battista J, Lee T-Y. A fully automated non-external marker 4D-CT sorting algorithm using a serial cine scanning protocol. *Phys Med Biol*. 2009;54(7):2049-2066. doi:10.1088/0031-9155/54/7/013

11. Keall PJ, Vedam SS, George R, Williamson JF. Respiratory regularity gated 4D CT acquisition: concepts and proof of principle. *Australas Phys Eng Sci Med*. 2007;30(3):211. doi:10.1007/BF03178428

12. Werner R, Sentker T, Madesta F, et al. Intelligent 4D CT sequence scanning (i4DCT): First scanner prototype implementation and phantom measurements of automated breathing signal-guided 4D CT. *Med Phys*. 2020;47(6):2408-2412. doi:https://doi.org/10.1002/mp.14106

13. Szkitsak J, Werner R, Fernolendt S, et al. First clinical evaluation of breathing controlled four-dimensional computed tomography imaging. *Phys imaging Radiat Oncol*. 2021;20:56-61.

14. Castillo SJ, Castillo R, Castillo E, et al. Evaluation of 4D CT acquisition methods designed to reduce artifacts. *J Appl Clin Med Phys*. 2015;16(2):4949.

15. Yushkevich PA, Piven J, Hazlett HC, et al. User-guided 3D active contour segmentation of anatomical structures: significantly improved efficiency and reliability. *Neuroimage*. 2006;31(3):1116-1128. doi:10.1016/j.neuroimage.2006.01.015

16. Fedorov A, Beichel R, Kalpathy-Cramer J, et al. 3D Slicer as an image computing platform for the Quantitative Imaging Network. *Magn Reson Imaging*. 2012;30(9):1323-1341. doi:10.1016/j.mri.2012.05.001

17. Yamamoto T, Kabus S, Lorenz C, et al. 4D CT lung ventilation images are

affected by the 4D CT sorting method. *Med Phys*. 2013;40(10):101907. doi:10.1118/1.4820538

18. Sawant A, Yamamoto T, Cai J. Treatment planning based on lung functional avoidance is not ready for clinical deployment. *Med Phys*. 2018;45(6):2353-2356. doi:10.1002/mp.12881

19. Young HM, Park CK, Chau O-W, Lee T-Y, Gaede S. Technical Note: Volumetric computed tomography for radiotherapy simulation and treatment planning. *J Appl Clin Med Phys*. July 2021. doi:10.1002/acm2.13336

CHAPTER 4

4 Simultaneous Ventilation and Perfusion Using Computed Tomography: Validation of a Novel Lung Imaging Technique

We developed a novel pipeline to simultaneously image ventilation (V), perfusion (Q), and V/Q ratio on a volumetric CT scanner. Two pigs underwent this protocol, and Xe-enhanced CT ventilation and PET perfusion imaging for validation, demonstrating significant correlation between the established methods and our novel technique. Two NSCLC patients underwent the V/Q imaging protocol before and six weeks after radiation therapy, demonstrating its feasibility in this patient population and its sensitivity to functional changes after radiation therapy.

The contents of this chapter are in preparation for submission to the journal Medical Physics by: HM Young, F Su, TY Lee, and S Gaede.

4.1 Introduction

Early trials incorporating CT-based functional lung avoidance in radiation therapy have shown positive results, suggesting the strong potential of this method to substantially reduce radiation toxicity in NSCLC. Studies to validate CT-based ventilation imaging (CTVI) against established methods have shown weak to moderate correlation. There are various potential reasons why correlation is not stronger. First, past validation studies comparing CTVI against "gold standard" measurements of lung ventilation, including Galligas PET[1–3], Technegas SPECT[4], ^{3}He or ^{129}Xe MRI[5–7], and Xe-CT[8–10] required cross modality deformable image registration. Patients are often imaged in a different position, under different breathing conditions (free breathing versus deep inhalation),[7] and on different days. Second, CTVI methods using 4D-CT imaging also require registration of extreme phases of respiration and, therefore, rely on accurate deformable image registration algorithms. Also, 4D-CT is prone to motion artifacts and, therefore, may lead to inaccurate measures of ventilation[11]. Finally, ventilation is only one measure of lung function. Perfusion is also critical to gas exchange, and as such may be an equally important imaging marker of function[12,13].

In the assessment of lung function before and/or after radiation therapy, there have been few studies which include both ventilation and perfusion. As a result, it is difficult to say with confidence whether ventilation, perfusion, or the ventilation-perfusion ratio (V/Q) is a more reliable marker for tissues that should be preferentially spared from radiation to reduce the risk of radiation pneumonitis. One study showed that perfusion more effectively predicted CT density changes after radiation[12], but this has not yet been studied in relation to patient outcomes.

To date, ventilation/perfusion ratio (V/Q) imaging has mostly been performed using nuclear imaging techniques; SPECT and PET[14,15]. These methods are more expensive and less widely accessible to radiation oncology patients. The development of a method which images both ventilation and perfusion, simultaneously, and can be easily incorporated directly into CT based radiation treatment planning will enable research into both measures of lung function and how to optimally define regions of high function for preservation.

Volumetric CT (vCT) scanners have recently been introduced to diagnostic imaging departments world-wide and offer whole organ dynamic imaging capabilities[16]. VCT can image up to 16 cm axial field-of-view (aFOV) and rotate as fast as 0.28 s per revolution. VCT offers a well-established method for measuring cardiac perfusion that is typically acquired under breath-hold conditions.

Volumetric CT scanners are not yet widely used in radiation oncology in North America, but as their prevalence grows in radiology, increased used in radiation oncology may follow. Volumetric 4D-CT has the potential to reduce or eliminate motion artifacts[17] and therefore provide more accurate simulation for radiation therapy and more accurate measures of ventilation. In addition, its wide aFOV enables dynamic perfusion imaging across a larger volume than was possible with previous generations of CT scanners. It is therefore possible to use vCT generate simultaneous 3-dimensional maps of ventilation (V) and perfusion (Q), and V/Q ratio.

The purpose of this study is two-fold. First, we describe and validate a novel protocol to simultaneously image ventilation and perfusion in a dynamic contrast-enhanced CT scan using a volumetric CT scanner using a pre-clinical porcine model. Ventilation imaging will be validated against xenon-enhanced CT ventilation, acquired during the same CT scanning session, and perfusion imaging will be validated against ^{68}Ga labelled macroaggregated albumin (MAA) PET perfusion imaging, acquired in a PET/CT scanning session performed immediately following vCT. Second, applications of 4D-CT ventilation imaging will be considered in two Stage III NSCLC patients where V, Q, and V/Q ratio will be compared at baseline and at 6-weeks post radiotherapy.

4.2 Materials and Methods

4.2.1 Porcine Study

Two pigs were imaged for this study under anesthetic and mechanical ventilation using a Harvard large animal ventilator. The animals were ventilated at a rate of 20 breaths/minute and a breathing volume of 7-15 mL/kg of body weight. One pig was imaged at a single timepoint at a weight of 37 kg and the second pig was imaged at three timepoints (week 0, 33 kg; week 2, 35 kg; week 7, 63 kg).

4.2.1.1 Dynamic Contrast-Enhanced CT Acquisition

The animals were imaged on a GE Revolution 256-slice volumetric CT scanner (GE Healthcare, Milwaukee, USA). The image acquisition details are shown in Table 4-1.

Table 4-1 Scan parameters for all CT image acquisitions

Subject	Mode	Rotation Speed [s]	aFOV [mm]	Voltage [kV]	Current [mA]	Scan time [s]
pig	cine	0.5	160	80	120	60
NSCLC patient	cine	0.28	160	100	100	40-60

The animals were imaged in a supine position with their forearms raised. At the beginning of the study, the animals were breathing medical air. The Xe-enhanced CT scan was performed first, as Xe gas is washed out more quickly than an injected iodine-based contrast agent. An apparatus built in-house was used to switch between medical air and the Xe source during imaging. The experimental setup is shown in Figure 4-1. A reservoir bag was filled with 99.999% purity xenon gas; for the first two studies, a 2 L bag was used. For the final two studies, a 4 L bag was used because the Xe was being diluted with medical air in the tubing before being inhaled. At the beginning of the scan, the animal was breathing in medical air through the ventilator. After 5 seconds passed, a single switch was turned to shut off the ventilator connection to the medical air tank, and to open the connection to the Xe bag. The animal inhaled the Xe gas in multiple breaths, with the concentration in the lungs increasing over time. When the Xe bag was empty, the switch was returned to close the Xe connection to the ventilator and restore the ventilator access to medical air. The concentration of Xe passing from the ventilator to the animal was measured using a Xe/Oxygen concentration monitor and the peak concentration was recorded.

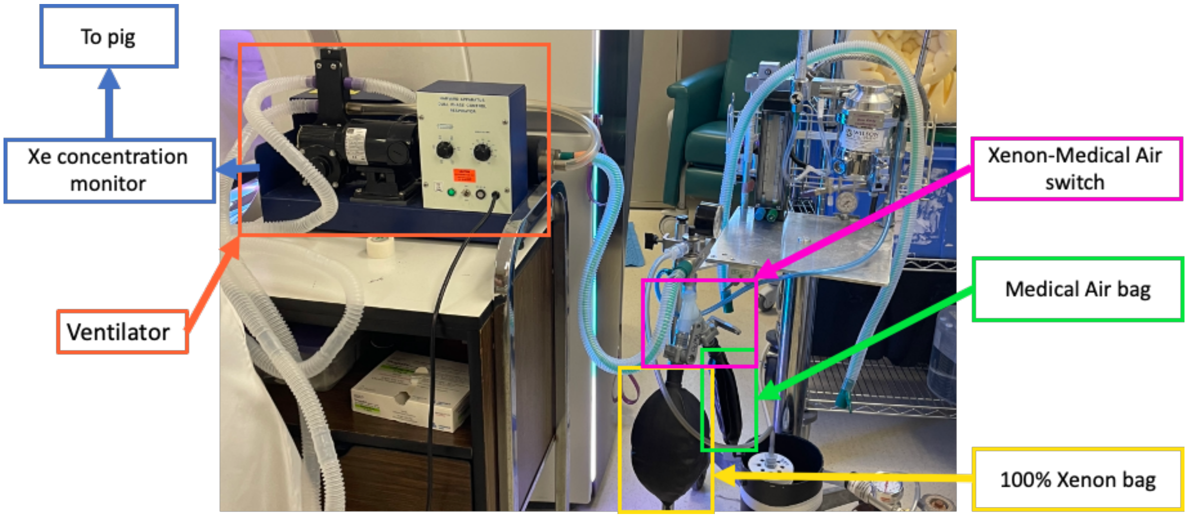

Figure 4-1 Experimental setup used for Xe-enhanced ventilation imaging.
A fixed volume of Xe was stored in one reservoir bag (yellow) and medical air flowed through the second bag (green). An in-house constructed mechanism (pink) was used to switch the ventilator source between these bags. The gas was pulled from one of these bags through the ventilator and passed through a Xe concentration monitor before being inhaled by the anesthetized pig.

A five-minute wait period was used between the Xe-enhanced CT scan and the simultaneous ventilation-perfusion scan to ensure wash-out of the Xe gas. The V/Q scan was acquired with the same parameters as used for the Xe scan, shown above and in Table 4-1. The animal was breathing medical air for the duration of this scan. 10 seconds after the image acquisition started, a bolus injection of Isovue contrast was given. Images were reconstructed into 5 mm slices, with an in-plane resolution of 0.58 mm x 0.58 mm, and a temporal resolution of 0.5 seconds.

4.2.1.2 ^{68}Ga MAA PET Acquisition

Immediately following CT imaging, the animal underwent PET-CT imaging on a GE Discovery VCT PET-CT scanner in the same position as was used for CT imaging: supine with the forearms raised. A slow helical CT image was acquired for attenuation correction and for identifying the thoracic cavity. One vial of macroaggregated albumin (MAA) (Jubilant DraxImage Inc. dba, Montreal Canada) was labelled with up to 200 MBq of Ga-68 produced in a local cyclotron[18]. Up to 10 mL of labelled MAA was injected into the animal and the dose syringe was assayed before and after the injection to determine the activity injected. Immediately after injection, a ten-minute dynamic scan was acquired, followed by two static five-minute scans. All images were reconstructed to 3.3 mm thick slices with an in-plane resolution of 1 mm x 1 mm.

4.2.1.3 Perfusion Analysis

Deformable image registration was performed using Elastix to register all images in the V/Q CT image series to the first image. The registration algorithm used b-spline interpolation, and a normalized mutual information metric. The registered images were loaded into a trial version of GE CT Perfusion software (GE Healthcare, Milwaukee) to calculate blood flow using the Johnson-Wilson-Lee tracer-kinetic model[19].

The first three minutes of the dynamic PET perfusion scan were also loaded into the trial version of CT Perfusion software. Blood flow was calculated using the Johnson-Wilson-Lee tracer-kinetic model with a modified impulse residue function to account for the fact that MAA arrests in the capillaries of the lung after injection.

4.2.1.4 Ventilation Analysis

An end-inhale and an end-exhale image were identified from the pre-contrast portion of the V/Q scan after deformable image registration had been applied as explained above. A lung volume mask was generated using a semi-automatic density-based method. Voxel-wise specific ventilation was calculated within the lung mask from these images using Equation 4-1[20] below, where HU_{in} and HU_{ex} are the CT number of the voxel in the inhale and exhale images, respectively:

Equation 4-1

$$SV = 1000 \times \frac{HU_{in} - HU_{ex}}{HU_{ex}(1000 + HU_{in})}$$

In Equation 4-1 above, SV is specific ventilation, HU_{in} and HU_{ex} are the CT numbers of the voxel in the inhale and exhale images, respectively. From the Xe-enhanced scan, an end-inhale image was identified form the pre-Xe baseline portion of the scan, and from the time of peak Xe enhancement. These images were both non-rigidly registered to the baseline V/Q image using Elastix, so both ventilation maps could be directly compared. A map of ventilation was calculated within the same lung mask using Equation 4-2 below, where HU_{PeakXe} and HU_{BL} represent the CT number of the voxel in the peak enhancement and baseline images, respectively:

Equation 4-2

$$XeVent = HU_{PeakXe} - HU_{BL}$$

4.2.1.5 Statistical Analysis

To compare the V/Q SV maps to the Xe-enhanced ventilation maps, both were down-sampled to 1 cm x 1 cm x 1 cm spatial resolution to minimize the impact of small registration errors and image noise. Ventilation values were compared voxel-wise using the Pearson correlation coefficient. Similarly, the perfusion maps were down sampled to a 5 mm x 5 mm x 5 mm spatial resolution. A smaller resolution was chosen because the CT and PET images were not acquired on the same scanner, so the overlap of the two maps is imperfect and fewer voxels are available for the calculation. Perfusion values were also compared voxel-wise using the Pearson correlation coefficient.

4.2.2 NSCLC Patient Study

Two patients with Stage III non-small cell lung cancer were imaged before and six weeks after undergoing radiation therapy as part of the Radiation Induced Cardiac Toxicity- Lung clinical trial (NCT03416972).

4.2.2.1 Patient Characteristics

Clinical characteristics of the two patients enrolled in the study are summarized in Table 4-2 below:

Table 4-2 Clinical characteristics of the patients who participated in the study.

	Patient 1	**Patient 2**
Age (years)	65	63
Sex	M	M
Tumour Location	Upper left lobe	Upper left lobe
Staging	T3N2M0	T4N2M0
Radiation Dosing	60 Gy in 30 fx	60 Gy in 30 fx with PET-delineated sub-volume simultaneously boosted to 77 Gy
Additional Treatments	concurrent carboplatin and paclitaxel, then durvalumab immunotherapy	concurrent cisplatin and vinblastine, then durvalumab immunotherapy
Comorbidities	History of coronary artery disease	-
Clinical Symptoms After 1 year	Increasing cough, shortness of breath, hypotension	None

4.2.2.2 Image Acquisition

The patients were imaged on a GE Revolution volumetric CT scanner with the acquisition details shown in Table 4-1. Image reconstruction was cardiac-gated for the purposes of the clinical trial, which led to some variation in total scan time and the time at which contrast was injected. An iodine-based contrast was administered approximately 10 seconds after the beginning of the dynamic scan. Images were reconstructed into 5 mm slices, with an in-plane resolution of 0.9 mm x 0.9 mm and a temporal resolution of 0.3 seconds.

4.2.2.3 Perfusion and Ventilation

Deformable image registration was performed to register all images in the CT image series to the first image as described above. Blood flow maps were calculated using a trial version of GE CT Perfusion software (GE Healthcare, Milwake). Specific ventilation maps were calculated using the same method described in the animal study above.

4.2.2.4 V/Q Ratio Maps

The ventilation and perfusion maps were already co-registered as they came from the same registered image set. The ventilation (V) and perfusion (Q) maps were both normalized to the 99th percentile of the image distribution and a V/Q map was calculated as a voxel-wise ratio of the two maps.

4.2.2.5 Interpretation of NSCLC Patient Imaging

The patient results were interpreted qualitatively with a focus on changes from baseline to follow-up imaging after radiation therapy.

4.3 Results

4.3.1 Porcine Study

4.3.1.1 Perfusion

For all imaging sessions, the MAA was successfully labelled with ^{68}Ga[21] and both contrast-enhanced imaging sessions were performed successfully. For all imaging sessions a moderate voxel-wise correlation was observed between the V/Q CT perfusion scan and the PET perfusion scan ($r = 0.24$-0.54, $p < 0.001$ for all). Qualitatively, patterns of perfusion were consistent between the two scan types, with higher perfusion in the posterior lung, and lower perfusion in the anterior. These results are shown in Figure 4-2.

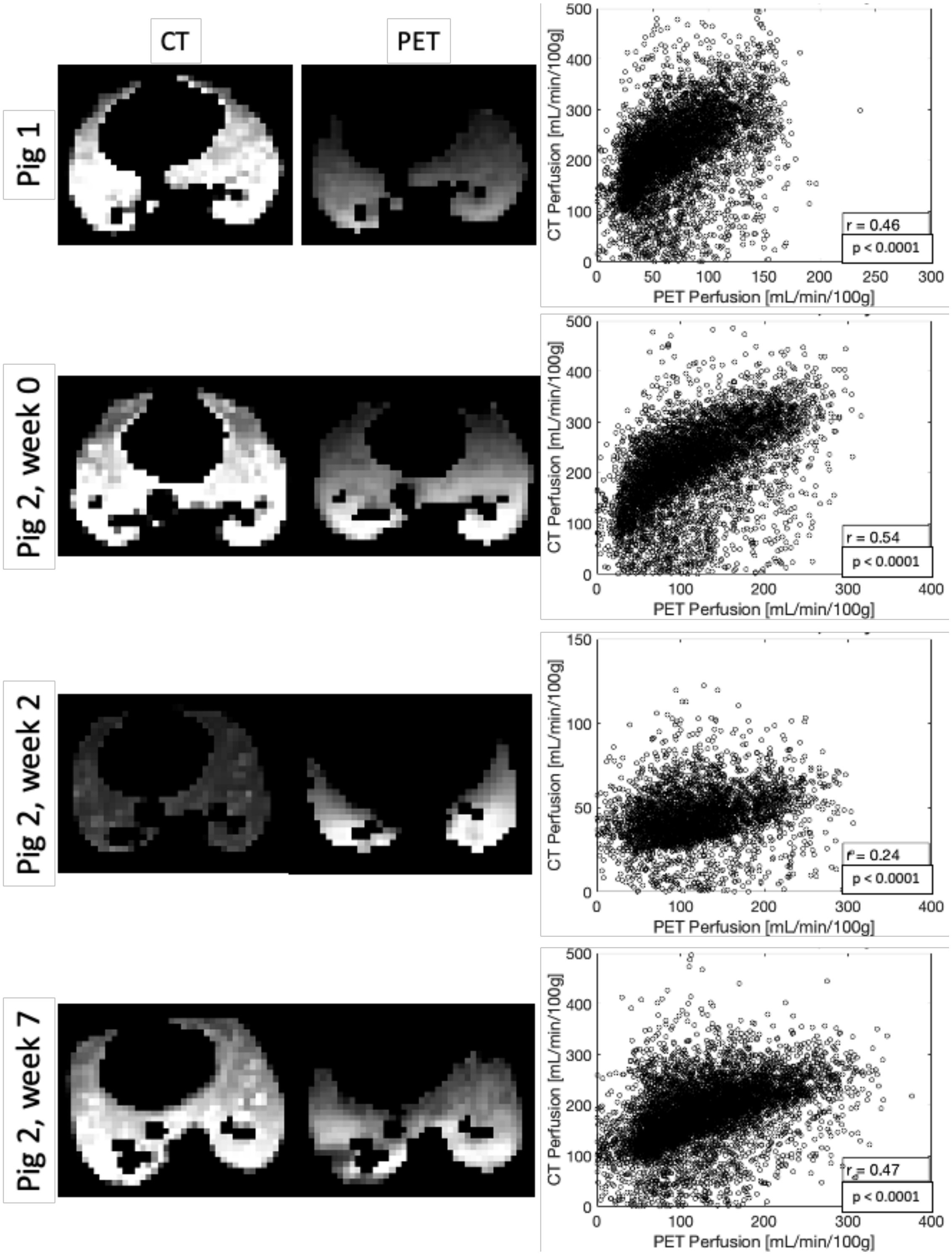

Figure 4-2 Voxel-wise comparison of CT and PET perfusion imaging.
Representative image samples from each scan are shown (W = 220, L = 110 HU) on the left. In the right column, voxel-wise comparison of CT perfusion compared to PET perfusion is shown. The two methods were significantly correlated in all cases (r = 0.24 - 0.54, $p < 0.001$ for all).

4.3.1.2 Ventilation

For all imaging sessions, acquisition of both V/Q and Xe-enhanced ventilation were performed successfully. For the first two imaging sessions (pig 1, and pig 2 week 0) when only 2 L of Xe was used, the CT V/Q ventilation images were not significantly correlated to the Xe-enhanced ventilation images. In these cases, the Xe signal measured in the lungs was lower, and the qualitative distribution of the signal was different than expected, with a low Xe signal in the posterior regions of the lungs. In the second two imaging sessions (pig 2, week 2 and week 7) when 4 L of Xe was used, V/Q and Xe-enhanced ventilation images were significantly correlated. In study 3, the V/Q ventilation and Xe ventilation were moderately correlated ($r = 0.66$, $p < 0.0001$), and in study 4 they were weakly correlated ($r = 0.12$, $p = 0.0001$). Qualitatively, the Xe signal took on the expected distribution with higher ventilation in the posterior lung. These results are shown in Figure 4-3.

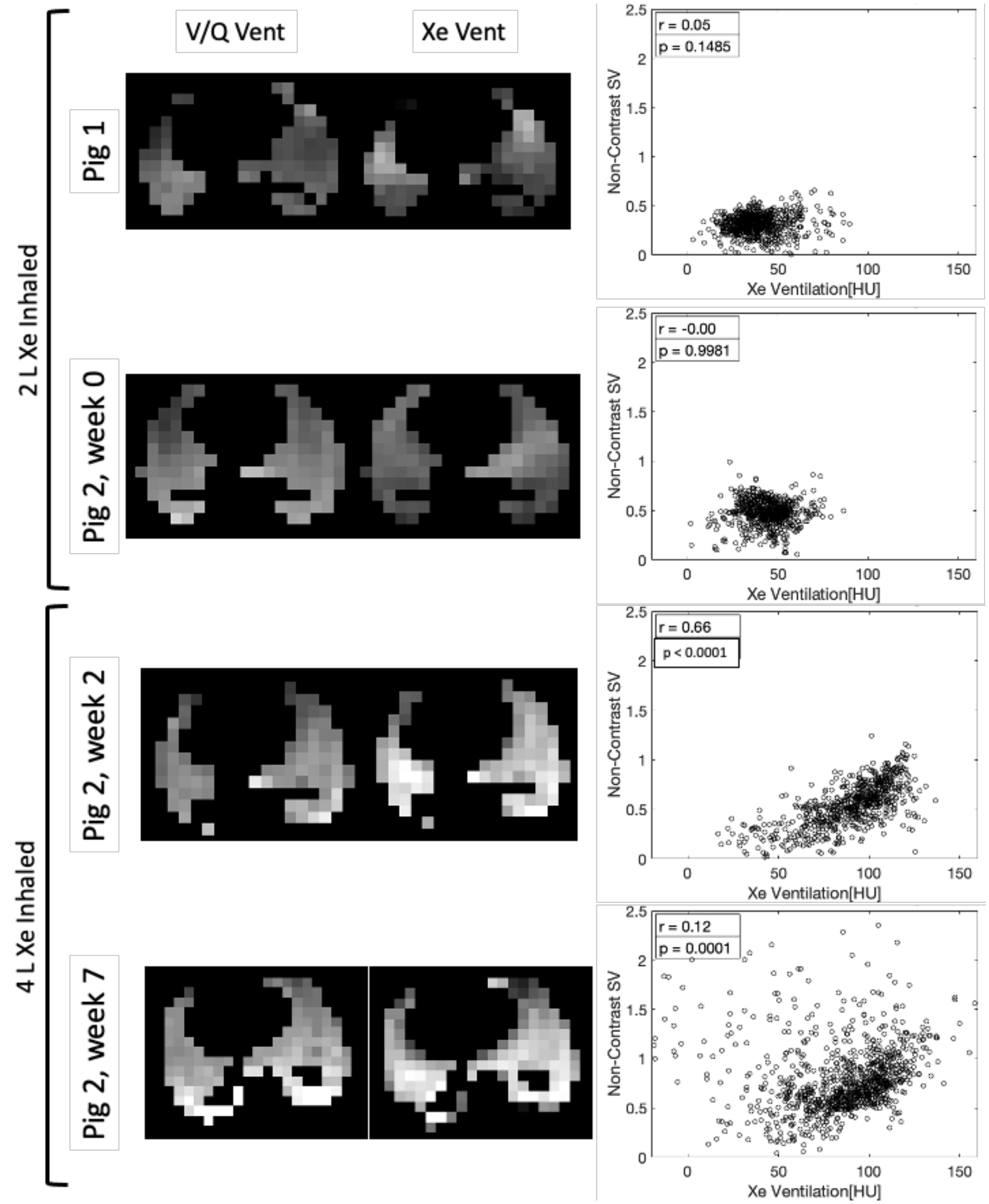

Figure 4-3 Voxel-wise comparison of V/Q and Xe-enhanced CT ventilation imaging. Representative image samples from each scan are shown (V/Q SV: W = 1.5, L = 0.5; Xe-ventilation: W = 120, L = 60 HU) on the left. In the right column, voxel-wise comparison of SV compared to Xe-enhanced ventilation is shown. For the first two sessions, 2 L of Xe was used and the two ventilation measures are not significantly correlated. However, for the second two sessions, 4 L of Xe was used and the V/Q SV maps were significantly correlated to the Xe-enhanced maps ($r = 0.66$, $p < 0.001$; $r = 0.12$, $p = 0.0001$).

4.3.2 NSCLC Patient Study

In both patients, the V/Q imaging procedure was well tolerated. In patient 1, both ventilation and perfusion decreased in the left lung after radiation therapy, as shown in Figure 4-4. The blood flow map shows that the patient's tumour has heterogeneous perfusion before treatment. In patient 2, ventilation decreased in the left lung after radiation therapy, but perfusion increased, as shown in Figure 4-5. This patient exhibited low perfusion and V/Q mismatch in the left lung before treatment, suggesting the tumour may have been restricting blood flow to the area. This patient showed signs of emphysema in the right lung in an area of low attenuation. In this region, the ventilation map appeared normal, but the blood flow map showed very low blood flow. As a result, this region appeared clearly as V/Q mismatch in V/Q imaging.

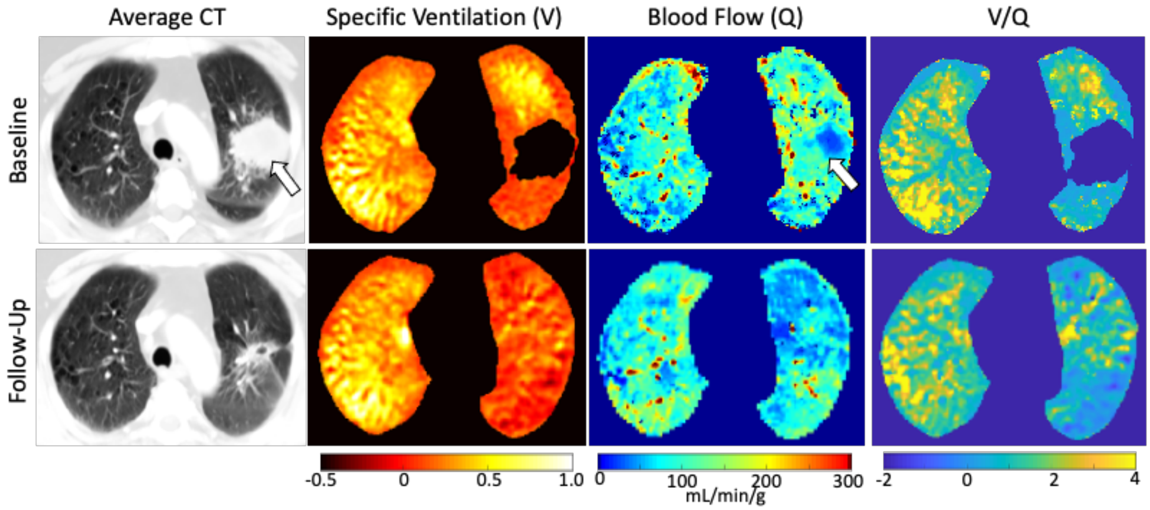

Figure 4-4 Representative slices from V/Q imaging at baseline and 6 weeks after radiotherapy in patient 1.

The averaged CT image (left) is provided for anatomical reference. Specific ventilation maps (second column) indicated decreased ventilation in the left lung after treatment. Blood flow maps (third column) indicated heterogeneous tumour perfusion at baseline (white arrows) and decreased blood flow in the left lung at follow-up. V/Q maps (right) indicated regions of V/Q mismatch (yellow) or reversed mismatch (blue).

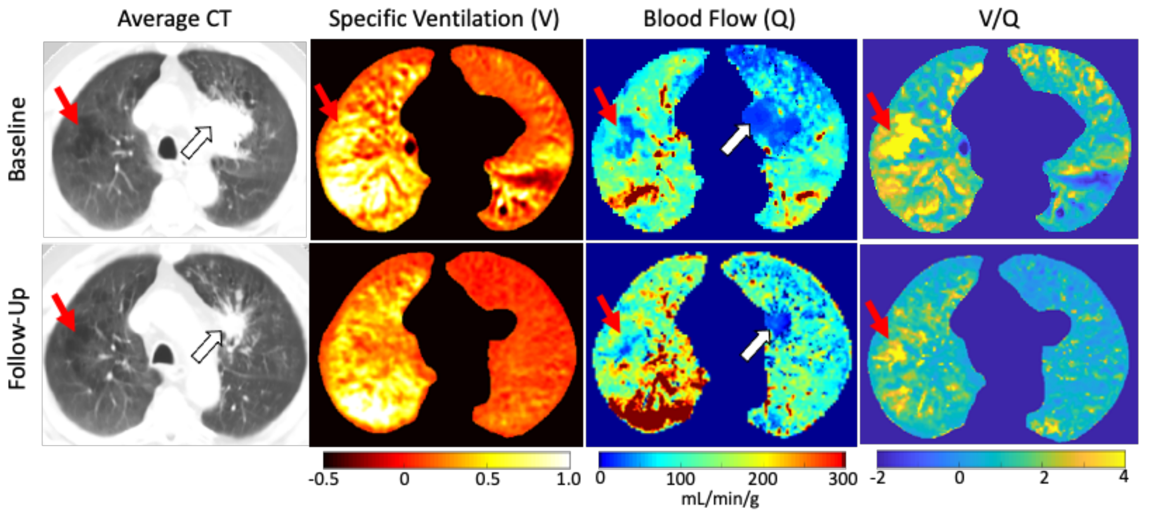

Figure 4-5 Representative slices from V/Q imaging at baseline and 6 weeks after radiotherapy in patient 2.

The averaged CT image (left) is provided for anatomical reference. Specific ventilation maps (second column) showed reduced ventilation in the left lung after treatment. Blood flow maps (third column) showed low tumour perfusion at baseline (white arrows) and increased blood flow in the irradiated lung after treatment. V/Q maps (right) indicated regions of V/Q mismatch (yellow) or reversed mismatch (blue). A region of emphysema (red arrows) appeared normal in the SV map but had low blood flow and appeared as V/Q mismatch.

4.4 Discussion

To the authors' knowledge, this is the first study to implement CT-based ventilation, perfusion, and V/Q imaging before and after radiation therapy in NSCLC. This study demonstrated the feasibility of this technique and demonstrated the method's sensitivity to changes after radiation therapy. While further study is needed to determine the sensitivity of the method to clinically relevant outcomes, these results are promising.

These results indicate two particularly interesting phenomenon that warrant further investigation. First, blood flow imaging in patient 1 indicated heterogeneous tumour blood flow at baseline, and low tumour blood flow in patient 2. Tumour blood flow has known effects on radiosensitivity[22], and the ability of this imaging technique to generate biomarkers predictive of patient outcomes should be further studied. In addition, patient 2's baseline imaging demonstrates the value of collecting ventilation, perfusion, and V/Q imaging simultaneously. There appears to be an emphysematous region with normalappearing ventilation. This is not unusual, as air may easily reach the region and inflate the lung tissue even if it has suffered degradation. However, the tissue loss was clearly seen in blood-flow imaging as a region of low blood flow, and in the V/Q map as a region of mismatch. There have been few studies comparing the ventilation and perfusion for creating functional avoidance structures and the outcomes of using each one or both together[13]. More work is needed in this area to ensure that the imaging used in future clinical trials is both easily implemented in a clinical setting, and highly sensitive to clinically relevant changes.

There have been several studies performed previously which have attempted to validate CT ventilation imaging measures[1]. Reaching a consensus on the best approach for this technique has been challenging as there are many variables to consider including whether the scan was performed under free-breathing or breath-hold conditions, the type of deformable image registration used, the ventilation calculation used, and the "gold standard" to which the CT method is compared. Recent review papers report that validation studies have yielded highly variable results, likely due to these many variables[1,23,24]. In this study, were able to reduce two of these variables by ensuring that all imaging was performed under free-breathing conditions, and both ventilation methods were performed back-to-back on the same scanner, so the animal did not move between images.

In this study, two of the Xe-enhanced CT images were noticeably different than was expected from previous studies, which demonstrated that ventilation was higher in the posterior regions of the lung, and lower in the anterior when the animal is positioned supine[25–27], as is also observed in humans. In the first two studies performed, when only 2 L of Xe was used in our ventilation system, this pattern was not clearly present, and our novel V/Q method did not correlate significantly to the Xe-measured ventilation. However, in the second two studies, when 4 L of Xe was used, the Xe ventilation maps appeared qualitatively as expected, and correlated significantly with our method. This suggests that, using the method outlined in this paper, 2 L of Xe is insufficient to image ventilation in a 30-60 kg pig and that 4 L is more appropriate.

The voxel-wise correlations measured between CT and PET perfusion methods, and between V/Q and Xe-enhanced ventilation methods were moderate, which is in alignment with comparable previous studies[2,24]. The mostly closely related study compared Jacobian-based CT ventilation measurements to Xe-enhanced CT ventilation[8]. This study used voxels within a rectangular region of interest on a chosen sagittal slice for comparison of the two methods. This study found a strong correlation between the novel Jacobian method and the Xe-enhanced method using these selected voxels, but it is unknown how a voxel-wise comparison through the entire lung volume would compare. Our validation study likely performed equally well, as previous studies have shown that voxel-wise correlation improves with the size of the voxels used[6], and a whole-lung method is susceptible to errors due to registration or from partial-volume effects near the lung boundary, so are likely to have reduced total correlation measures.

There are several limitations to our validation method. Firstly, all CT imaging was performed with 0.5 s temporal resolution, so respiratory motion causes minimal blurring in the image, while the PET perfusion imaging had a minimum temporal resolution of 5 s, so the images are blurred from respiratory motion. The measured perfusion values, especially in the inferior lungs, should therefore not be expected to perfectly correlate between the two modalities. Secondly, the pigs in the study were healthy, so they do not represent the heterogeneous ventilation and perfusion that would be present in most clinical applications of this technique. Lastly, the sample size for this study is small, with only two studies performed with an adequate dose of Xe. Further research may strengthen the findings shown here.

The patient imaging included in this study demonstrates several ways that CT V/Q imaging may impact clinical care. These include baseline tumour perfusion, which may suggest hypoxia, and baseline ventilation and perfusion which may indicate the susceptibility of surrounding lung tissue to radiation-induced toxicity. Follow-up imaging after treatment can show changes in blood flow due to reperfusion or inflammation, and changes in ventilation due to decreased airway obstruction or to inflammation. Importantly, this protocol can be easily applied at any follow-up timepoint when the patient would normally undergo CT imaging, so it can be more easily integrated in research or clinical practice than MRI or nuclear imaging. This study showed the feasibility of a novel protocol to derive ventilation, perfusion, and V/Q maps in a single dynamic CT scan and the results shown here highlight the potential clinical impact of this method.

4.5 Conclusion

In this study, the feasibility of a novel imaging acquisition and processing pipeline for CT-based ventilation, perfusion, and V/Q imaging was demonstrated. The technique was applied in 4 scans of 2 pigs, along with Xe-enhanced CT ventilation and PET perfusion, and demonstrated weak to moderate correlation with these established measures. Finally, the technique was used to generate comprehensive maps of lung function in two patients with NSCLC before and after undergoing radiation therapy and was sensitive to post-radiotherapy functional changes. This technique has exciting possible applications in clinical practice for better understanding the lung function of patients, and in research for studies of functional avoidance, treatment response, and other radiobiology research

4.6 References

1. Kipritidis J, Tahir BA, Cazoulat G, et al. The VAMPIRE challenge: A multi-institutional validation study of CT ventilation imaging. *Med Phys*. 2019;46(3):1198-1217. doi:10.1002/mp.13346

2. Kipritidis J, Siva S, Hofman MS, Callahan J, Hicks RJ, Keall PJ. Validating and improving CT ventilation imaging by correlating with ventilation 4D-PET/CT using 68Ga-labeled nanoparticles. *Med Phys*. 2014;41(1):11910. doi:10.1118/1.4856055

3. Eslick EM, Kipritidis J, Gradinscak D, et al. CT ventilation imaging derived from breath hold CT exhibits good regional accuracy with Galligas PET. *Radiother Oncol*. 2018;127(2):267-273.

4. Yamamoto T, Kabus S, Lorenz C, et al. Pulmonary ventilation imaging based on 4-dimensional computed tomography: comparison with pulmonary function tests and SPECT ventilation images. *Int J Radiat Oncol Biol Phys*. 2014;90(2):414-422. doi:10.1016/j.ijrobp.2014.06.006

5. Tahir BA, Van Holsbeke C, Ireland RH, et al. Comparison of CT-based Lobar Ventilation with 3He MR Imaging Ventilation Measurements. *Radiology*. 2016;278(2):585-592. doi:10.1148/radiol.2015142278

6. Tahir BA, Hughes PJC, Robinson SD, et al. Spatial Comparison of CT-Based Surrogates of Lung Ventilation With Hyperpolarized Helium-3 and Xenon-129 Gas MRI in Patients Undergoing Radiation Therapy. *Int J Radiat Oncol • Biol • Phys*. July 2018. doi:10.1016/j.ijrobp.2018.04.077

7. Tahir BA, Marshall H, Hughes PJC, et al. Comparison of CT ventilation imaging and hyperpolarised gas MRI: effects of breathing manoeuvre. *Phys Med Biol*. 2019;64(5):55013. doi:10.1088/1361-6560/ab0145

8. Reinhardt JM, Ding K, Cao K, Christensen GE, Hoffman EA, Bodas S V. Registration-based estimates of local lung tissue expansion compared to xenon CT

measures of specific ventilation. *Med Image Anal*. 2008;12(6):752-763. doi:10.1016/j.media.2008.03.007

9. Ding K, Cao K, Fuld MK, et al. Comparison of image registration based measures of regional lung ventilation from dynamic spiral CT with Xe-CT. *Med Phys*. 2012;39(8):5084-5098. doi:10.1118/1.4736808

10. Fuld MK, Easley RB, Saba OI, et al. CT-measured regional specific volume change reflects regional ventilation in supine sheep. *J Appl Physiol*. 2008;104(4):1177-1184. doi:10.1152/japplphysiol.00212.2007

11. Yamamoto T, Kabus S, Lorenz C, et al. 4D CT lung ventilation images are affected by the 4D CT sorting method. *Med Phys*. 2013;40(10):101907. doi:10.1118/1.4820538

12. Li Z, Le Roux P-Y, Callahan J, et al. Quantitative assessment of ventilation-perfusion relationships with gallium-68 positron emission tomography/computed tomography imaging in lung cancer patients. *Phys imaging Radiat Oncol*. 2022;22:8-12.

13. Wuschner AE, Wallat EM, Flakus MJ, et al. Radiation-induced Hounsfield unit change correlates with dynamic CT perfusion better than 4DCT-based ventilation measures in a novel-swine model. *Sci Rep*. 2021;11(1):1-14.

14. Siva S, Thomas R, Callahan J, et al. High-resolution pulmonary ventilation and perfusion PET/CT allows for functionally adapted intensity modulated radiotherapy in lung cancer. *Radiother Oncol*. 2015;115(2):157-162.

15. Kimura T, Doi Y, Nakashima T, et al. Combined ventilation and perfusion imaging correlates with the dosimetric parameters of radiation pneumonitis in radiation therapy planning for lung cancer. *Int J Radiat Oncol Biol Phys*. 2015;93(4):778-787.

16. So A, Imai Y, Nett B, et al. Technical Note: Evaluation of a 160-mm/256-row CT scanner for whole-heart quantitative myocardial perfusion imaging. *Med Phys*.

2016;43(8):4821. doi:10.1118/1.4957389

17. Young HM, Lee T-Y, Gaede S. Respiratory Motion Characterization and Motion Artefact Reduction Using Volumetric 4-Dimensional Computed Tomography. *Med Phys*. 2019;46(6):E211-E211.

18. Maus S, Buchholz H-G, Ament S, Brochhausen C, Bausbacher N, Schreckenberger M. Labelling of commercially available human serum albumin kits with 68Ga as surrogates for 99mTc-MAA microspheres. *Appl Radiat Isot*. 2011;69(1):171-175.

19. Lee T-Y, Yang DM, Li F, Marants R. CT perfusion techniques and applications in stroke and cancer. In: *Computed Tomography*. Springer; 2020:347-365.

20. Guerrero T, Sanders K, Castillo E, et al. Dynamic ventilation imaging from four-dimensional computed tomography. *Phys Med Biol*. 2006;51(4):777-791. doi:10.1088/0031-9155/51/4/002

21. Kotzerke J, Andreeff M, Wunderlich G. PET aerosol lung scintigraphy using Galligas. *Eur J Nucl Med Mol Imaging*. 2010;37(1):175-177.

22. Moeller BJ, Richardson RA, Dewhirst MW. Hypoxia and radiotherapy: opportunities for improved outcomes in cancer treatment. *Cancer Metastasis Rev*. 2007;26(2):241-248.

23. Hegi-Johnson F, de Ruysscher D, Keall P, et al. Imaging of regional ventilation: Is CT ventilation imaging the answer? A systematic review of the validation data. *Radiother Oncol*. 2019;137:175-185. doi:10.1016/j.radonc.2019.03.010

24. Vinogradskiy Y. CT-based ventilation imaging in radiation oncology. *BJR| Open*. 2019;1(xxxx):20180035.

25. Marcucci C, Nyhan D, Simon BA. Distribution of pulmonary ventilation using Xe-enhanced computed tomography in prone and supine dogs. *J Appl Physiol*. 2001;90(2):421-430. doi:10.1152/jappl.2001.90.2.421

26. Kreck TC, Krueger MA, Altemeier WA, et al. Determination of regional ventilation and perfusion in the lung using xenon and computed tomography. *J Appl Physiol*. 2001;91(4):1741-1749.

27. Fuld MK, van Beek EJ, Simon BA, Morgan JH, Hoffman EA. Establishing "Normal": Regional Ventilation Via Dynamic Xenon-CT in Humans. In: *B63. IMAGING: EVOLVING TECHNOLOGIES AND RELATION TO PATHOLOGY*. American Thoracic Society; 2009:A3530.

CHAPTER 5

5 CONCLUSIONS AND FUTURE DIRECTIONS

In this final chapter, a summary of the important findings and conclusions of Chapters 2-4 are provided, as well as a discussion of the limitations of each chapter. Finally, future studies to build on this work are outlined.

5.1 Overview and Research Questions

Volumetric CT scanners show great promise for both clinical and research applications in radiation oncology, especially in thoracic cancers such as non-small cell lung cancer (NSCLC). First, it was important to validate that the techniques used to reduce cone-beam artifacts in these scanners are sufficient to produce accurate CT numbers for CT simulation and radiation treatment planning. The first research objective in this thesis is to determine if volumetric CT scanners are suitable for use in radiotherapy simulation and treatment planning.

Next, I demonstrated how a volumetric CT scanner may be used to improve 4D-CT imaging of NSCLC. The second research objective was to determine if a 4D-CT protocol using a volumetric CT scanner reduces visible motion artifacts in patients with NSCLC and if so, if this reduction in motion artifacts significantly improves contouring accuracy.

The final objective of this thesis was to develop and demonstrate the feasibility of a method to image lung ventilation, perfusion, and ventilation-perfusion ratio in a single volumetric CT scanning protocol.

5.2 Summary and Conclusions

In Chapter 2 I imaged a Catphan phantom (The Phantom Laboratory, Salem, NY, USA) in a volumetric CT scanner using a range of aFOV values from the narrowest (40 mm) to the widest (160 mm). I assessed quality metrics including linearity, contrast-to-noise ratio (CNR), and uniformity for every image set, and compared them as a function of aFOV. The CT numbers of the highest density inserts were underestimated, but this could be corrected using an appropriate relative electron density (RED) curve. The RED curves I created from this data varied slightly as a function of aFOV, although the changes are not likely to significantly impact dosimetric calculations. This concern can be eliminated entirely with the use of a separate RED curve for each aFOV or by using an average RED curve. From these results, I concluded that there are no clinically significant differences between narrow and wide aFOV imaging on this scanner, and it is, therefore, suitable for radiation therapy simulation and treatment planning of many patients.

In Chapter 3 of this thesis, I outline the development of a novel method to reconstruct volumetric 4D-CT (v4D-CT). I compared the resulting datasets to clinical 4D-CT by imaging a motion phantom and four patients with NCSLC on both scanners. I re-sorted the v4D-CT image data, and discarded some, to simulate a conventional step-and-shoot acquisition with a clinical CT scanner (sim4D-CT). I qualitatively compared images from these three datasets for changes in visible motion artifacts and in both the phantom and patient images there was a clear reduction in motion artifacts using v4D-CT. I contoured a spherical target in the motion phantom and patient organs at risk (OARs) on each phase of each scan type. The mean Hausdorff distance between v4D-CT and clinical 4D-CT contours was significantly correlated to phase, suggesting that motion artifacts contributed to this difference. From this work I concluded that v4D-CT significantly reduces visible motion artifacts and significantly improves target and OAR contouring, which may impact patient outcomes.

In Chapter 4 of this thesis, I describe the development of a novel method to image ventilation (V), perfusion (Q), and the ventilation-perfusion ratio (V/Q) in a single dynamic contrast-enhanced CT scan. I performed an animal study to validate these methods against established Xe-enhanced CT ventilation and ^{68}Ga labelled MAA PET perfusion and imaged two patients with Stage III NSCLC before and six weeks after radiation therapy. This novel imaging pipeline was feasible in the patient population of interest, and changes in V and Q were detected in both patients six weeks after radiotherapy. The validation results indicated moderate and significant voxel-wise correlation between perfusion images from the V/Q scan and PET perfusion images ($r = 0.24$-0.54, $p < 0.0001$ for all). The V/Q scan ventilation map and the Xe ventilation map were also significantly correlatd for the two studies in which 4 L of Xe was used ($r = 0.66$, $p < 0.0001$; $r = 0.12$, $p = 0.0001$).

In summary, I demonstrated the suitability of vCT for radiation therapy simulation and treatment planning using a Catphan imaging study. I then showed that v4D-CT effectively eliminated visible respiratory motion artifacts which plague current clinical 4D-CT methods and improved contours of a spherical target and OARs, which may impact patient outcomes. Finally, I developed a method to generate images of ventilation, perfusion, and V/Q in a single volumetric CT scan and demonstrated the feasibility and sensitivity of this method in patients with NSCLC before and after radiation therapy.

5.3 Limitations

In this section, limitations from Chapters 2-4 will be summarized. It should be noted that the study-specific limitations are also presented in the Discussion section of each Chapter.

The primary limitation of Chapter 2 is that only Catphan phantom images were analyzed. Additional studies using an anthropomorphic phantom or human subjects may confirm that the findings in this study hold for all imaging applications. In addition, the volumetric CT scanner used in this study has a smaller bore size (diameter 80 cm) than most modern CT simulators. This small bore limits its use for imaging large patients or patients who require large positioning and immobilization equipment. As the prevalence of these scanners increases over time, development of a wide-bore model would facilitate increased use in radiation oncology settings

In Chapter 3, the limitation of the narrow bore size of current volumetric CT scanners also applies. Another limitation of this study is the fact that the sim4D-CT and clinical 4D-CT scans could not be exactly compared. The sim4D-CT data was simulated with an aFOV of 20 mm, while the clinical 4D-CT data was acquired with an aFOV of 24 mm. In addition, the sim 4D-CT images were acquired with a faster rotation time (0.28s/rotation) than the clinical scans (0.5s/rotation), so the blur in the sim4D-CT images was reduced. These limitations are likely the reason the contour comparisons between v4D-CT and sim4D-CT images were not significant. However, the sim4D-CT images still reproduced visually obvious motion artifacts, confirming that from the exact same imaging data, a wide aFOV is the cause of motion artifact reduction.

The primary limitation in Chapter 4 is the small number of patients and animals imaged. While the NSCLC patient imaging clearly demonstrates the feasibility of the technique, more imaging is required to demonstrate the sensitivity of the technique to clinically relevant changes in functional images. While the validation performed for this thesis has already demonstrated significant correlation of ventilation and perfusion imaging from our novel method with established methods, a larger study may strengthen these findings.

5.4 Future Directions

5.4.1 Validation of Ventilation-Perfusion Method

The results shown in Chapter 4 of this thesis demonstrate the feasibility of generating ventilation and perfusion imaging in a single dynamic contrast-enhanced CT scan. This chapter also includes results which show that this method is sensitive to changes in ventilation and perfusion after conventionally fractionated radiation therapy for stage III non-small cell lung cancer in a sample of two patients. A small validation study was also performed with positive results. Building off the findings in this thesis, a larger validation study using the same methods outlined in Chapter 4 may provide stronger evidence to support the translation of this work into other research applications.

Alternatively, to eliminate dependence on Xe for the study, ventilation imaging using Galligas PET imaging may be considered[1], as it is another established method of imaging ventilation and has been used in validation studies of CTVI methods[2,3]. If this method is used, great care must be taken to ensure that deposition of the tracer in the large airways is excluded from the image, so it does not negatively impact the comparison to our CTVI method.

5.4.2 Future Clinical Study

The imaging pipeline developed in Chapter 4 has many potential research applications. It is particularly well-suited to address unanswered questions about which lung imaging metrics are the best predictors of patient outcomes such as radiation pneumonitis. There are already ongoing clinical trials using ventilation or perfusion metrics to generate functional avoidance volumes[4], and early results are positive[5]. However, there has been little work done to compare the effectiveness of different functional imaging metrics so it is not known which methods will perform best clinically. One animal study suggested that perfusion measurements were more predictive of increased lung density at follow-up than ventilation[6], but the clinical impact of this difference is not yet known.

Functional lung imaging may also provide important information for research involving other treatments for NSCLC including surgery, chemotherapy, and more recently, immunotherapy. Surgery is a local treatment, so lung function before surgery is important when determining if surgery is the best course of treatment. Global measures of lung function such as spirometry and the diffusing capacity of the lungs for carbon monoxide (DL_{CO}) are often used, but research in other lung diseases suggests that the spatial information provided by imaging can help to predict patient outcomes[7]. Chemotherapy and immunotherapy are often used in conjunction with radiation therapy, and combined therapies are known to increase the risk of radiation pneumonitis[8,9]. More research is needed to determine which patients will develop unacceptable toxicity, and how it might be prevented.

In a study being prepared for ethics submission, we aim to use the technique outlined in Chapter 4 to image ventilation, perfusion, and V/Q ratio in patients with Stage I-III NSCLC before and after their treatment. This treatment may include surgery, chemotherapy, immunotherapy, or radiation therapy. This study will address the following research questions:

1) *Does the volume of total lung, ventilated lung, perfused lung, or V/Q matched lung receiving over 20 Gy predict the risk of pneumonitis?*

2) *Are there significant differences in the changes in ventilation, perfusion, or V/Q ratio after therapy for patients undergoing single modality treatment, chemo-radiation, or chemo-radiation followed by immunotherapy?*

3) *Do changes in functional imaging metrics at 6 weeks after therapy predict toxicity present at 6 months or 1 year following treatment?*

5.5 Significance and Impact

NSCLC remains the leading cause of cancer deaths in Canada[10], and potentially severe treatment toxicities often prevent the use of higher radiation doses or otherwise more aggressive treatment plans. Currently, approximately 30% of patients who undergo radiation therapy experience radiation-induced lung injury (RILI)[11]. Limitations in imaging have contributed to these problems; 4D-CT motion artifacts have been shown to be related to reduced local control in liver cancer[12]. Developments in lung imaging, including functional imaging for functional avoidance treatment planning, show promise for reducing the risks of RILI[13].

In this thesis, I explore methods to exploit the benefits of volumetric (or area-detector) CT scanners to improve anatomical and functional imaging used in clinical care and research of NSCLC. Volumetric CT scanners are increasing in use worldwide and will likely be used increasingly in radiation oncology settings. This thesis sets the foundation for how these scanners can be used in radiation oncology settings to significantly improve patient care. In addition, there are innumerable research opportunities created by the ability to image lung function using CT in a radiation oncology setting, as explained in section 5.4.

In this thesis, I demonstrated that volumetric CT scanners are suitable for CT simulation and radiation treatment planning. I then demonstrated how the application of volumetric 4D-CT can greatly reduce motion artifacts and uncertainties in target and OAR contouring, which may contribute to improved patient outcomes. Finally, I developed a protocol to simultaneously image lung ventilation, perfusion, and V/Q ratio. I demonstrated how new imaging protocols using volumetric CT advance both anatomical and functional lung imaging in ways that can impact clinical care and provide new opportunities for clinical research into lung function in patients with thoracic cancers.

The work in this thesis has many applications outside of NSCLC, including small-cell lung cancer, esophageal cancer, breast cancer, and mediastinal lymphomas. These cancers are all treated with high curative-intent doses, and RILI is a risk in all these patient cohorts[14–16]. Therefore, more accurate and detailed structural and functional lung imaging may be of benefit in all these cases to reduce treatment toxicity. This work has may potential applications in research on radiation biology, functional lung avoidance, treatment response research and more. Most importantly, the novel imaging methods explored in this thesis can be easily implemented using any volumetric or area-detector CT scanner. As this type of scanner becomes more commonplace in hospitals and cancer clinics, this research may facilitate improvements in routine clinical imaging, and the use of validated functional imaging biomarkers to improve patient outcomes.

5.6 References

1. Kotzerke J, Andreeff M, Wunderlich G. PET aerosol lung scintigraphy using Galligas. *Eur J Nucl Med Mol Imaging*. 2010;37(1):175-177.

2. Kipritidis J, Siva S, Hofman MS, Callahan J, Hicks RJ, Keall PJ. Validating and improving CT ventilation imaging by correlating with ventilation 4D-PET/CT using 68Ga-labeled nanoparticles. *Med Phys*. 2014;41(1):11910. doi:10.1118/1.4856055

3. Eslick EM, Kipritidis J, Gradinscak D, et al. CT ventilation imaging derived from breath hold CT exhibits good regional accuracy with Galligas PET. *Radiother Oncol*. 2018;127(2):267-273.

4. Khalil AA, Hau E, Gebski V, et al. Personal innovative approach in radiation therapy of lung cancer-functional lung avoidance SPECT-guided (ASPECT) radiation therapy: a study protocol for phase II randomised double-blind clinical trial. *BMC Cancer*. 2021;21(1):1-9.

5. Vinogradskiy Y, Castillo R, Castillo E, et al. Results of a multi-institutional phase 2 clinical trial for 4DCT-ventilation functional avoidance thoracic radiation therapy. *Int J Radiat Oncol Biol Phys*. 2022;112(4):986-995.

6. Wuschner AE, Wallat EM, Flakus MJ, et al. Radiation-induced Hounsfield unit change correlates with dynamic CT perfusion better than 4DCT-based ventilation measures in a novel-swine model. *Sci Rep*. 2021;11(1):1-14.

7. Adams CJ, Capaldi DPI, Di Cesare R, McCormack DG, Parraga G, Network CRR. On the potential role of MRI biomarkers of COPD to guide bronchoscopic lung volume reduction. *Acad Radiol*. 2018;25(2):159-168.

8. Paz-Ares L, Spira A, Raben D, et al. Outcomes with durvalumab by tumour PD-L1 expression in unresectable, stage III non-small-cell lung cancer in the PACIFIC trial. *Ann Oncol*. 2020;31(6):798-806.

9. LeClair JN, Merl MY, Cohenuram M, Luon D. Real-world incidence of pneumonitis in patients receiving durvalumab. *Clin Lung Cancer*. 2022;23(1):34-42.

10. *Canadian Cancer Statistics 2021*.; 2021.

11. Palma DA, Senan S, Tsujino K, et al. Predicting radiation pneumonitis after chemoradiation therapy for lung cancer: an international individual patient data meta-analysis. *Int J Radiat Oncol Biol Phys*. 2013;85(2):444-450.

12. Sentker T, Schmidt V, Ozga A-K, et al. 4D CT image artifacts affect local control in SBRT of lung and liver metastases. *Radiother Oncol J Eur Soc Ther Radiol Oncol*. 2020;148:229-234. doi:10.1016/j.radonc.2020.04.006

13. Yamamoto T, Kabus S, Von Berg J, Lorenz C, Keall PJ. Impact of four-dimensional computed tomography pulmonary ventilation imaging-based functional avoidance for lung cancer radiotherapy. *Int J Radiat Oncol Biol Phys*. 2011;79(1):279-288.

14. Goldman UB, Wennberg B, Svane G, Bylund H, Lind P. Reduction of radiation pneumonitis by V20-constraints in breast cancer. *Radiat Oncol*. 2010;5(1):1-6.

15. Tonison JJ, Fischer SG, Viehrig M, et al. Radiation pneumonitis after intensity-modulated radiotherapy for esophageal cancer: institutional data and a systematic review. *Sci Rep*. 2019;9(1):1-8.

16. Pinnix CC, Smith GL, Milgrom S, et al. Predictors of radiation pneumonitis in patients receiving intensity modulated radiation therapy for Hodgkin and non-Hodgkin lymphoma. *Int J Radiat Oncol Biol Phys*. 2015;92(1):175-182.

APPENDIX

Appendix A – Health Science Research Ethics Board Approval Notices

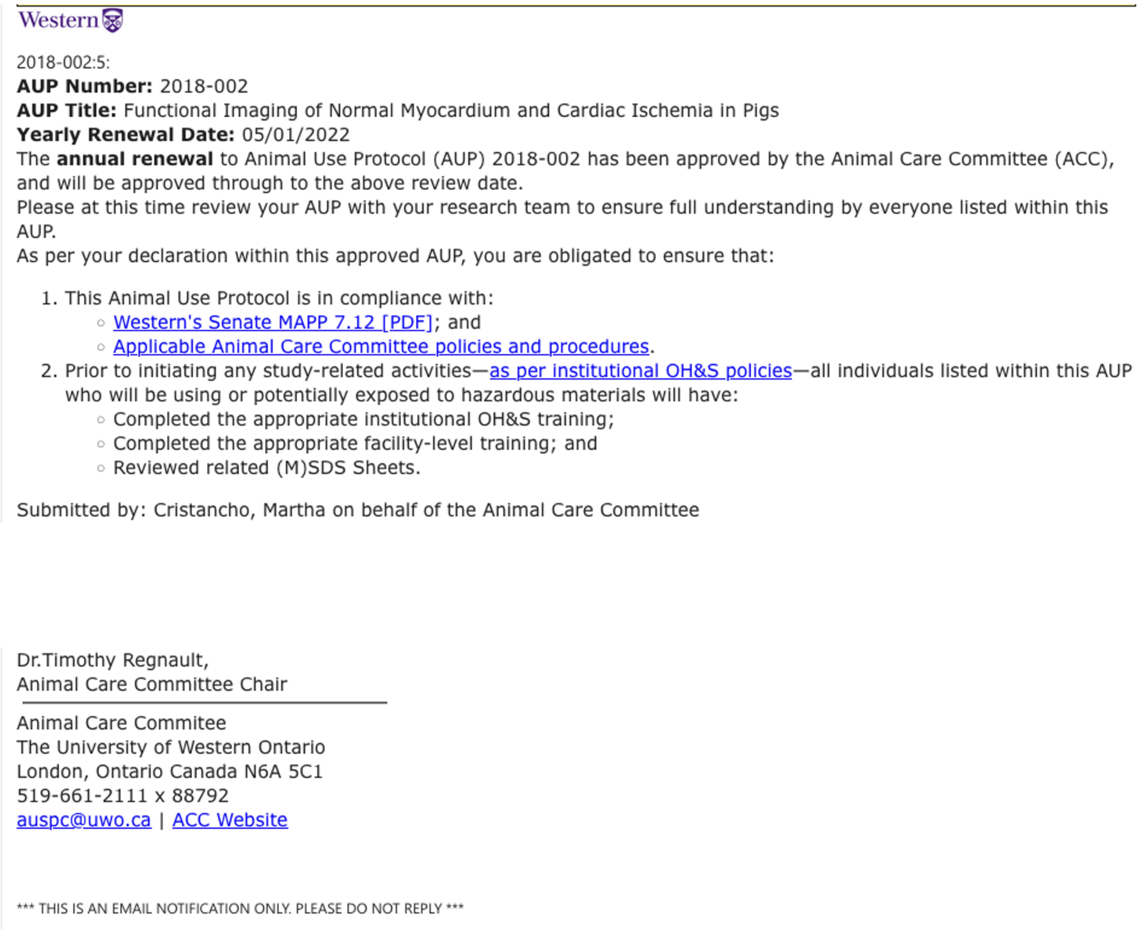

Western

2018-002:5:
AUP Number: 2018-002
AUP Title: Functional Imaging of Normal Myocardium and Cardiac Ischemia in Pigs
Yearly Renewal Date: 05/01/2022
The **annual renewal** to Animal Use Protocol (AUP) 2018-002 has been approved by the Animal Care Committee (ACC), and will be approved through to the above review date.
Please at this time review your AUP with your research team to ensure full understanding by everyone listed within this AUP.
As per your declaration within this approved AUP, you are obligated to ensure that:

1. This Animal Use Protocol is in compliance with:
    - Western's Senate MAPP 7.12 [PDF]; and
    - Applicable Animal Care Committee policies and procedures.
2. Prior to initiating any study-related activities—as per institutional OH&S policies—all individuals listed within this AUP who will be using or potentially exposed to hazardous materials will have:
    - Completed the appropriate institutional OH&S training;
    - Completed the appropriate facility-level training; and
    - Reviewed related (M)SDS Sheets.

Submitted by: Cristancho, Martha on behalf of the Animal Care Committee

Dr.Timothy Regnault,
Animal Care Committee Chair

Animal Care Commitee
The University of Western Ontario
London, Ontario Canada N6A 5C1
519-661-2111 x 88792
auspc@uwo.ca | ACC Website

*** THIS IS AN EMAIL NOTIFICATION ONLY. PLEASE DO NOT REPLY ***

Western Research

Date: 13 May 2021

To: Stewart Gaede

Project ID: 109084

Study Title: Identification of acute radiation-induced cardiac toxicity after non-small cell lung cancer radiotherapy with advanced multi-modality imaging (RICT-LUNG)

Reference Number/ID: N/A

Application Type: HSREB Amendment Form

Review Type: Delegated

Full Board Reporting Date: 08/June/2021

Date Approval Issued: 13/May/2021 14:48

REB Approval Expiry Date: 07/Jun/2021

Dear Stewart Gaede ,

The Western University Health Sciences Research Ethics Board (HSREB) has reviewed and approved the WREM application form for the amendment, as of the date noted above.

Documents Approved:

Document Name	Document Type	Document Date	Document Version
12May2021 - RICT Lung Ethics Protocol - cc	Protocol (Western)	12/May/2021	
12May2021 - RICT Lung Protocol - cc	Protocol	12/May/2021	
12May2021 - LOI RICT-Lung - cc	Consent Form	12/May/2021	

Documents Acknowledged:

Document Name	Document Type	Document Date	Document Version
12May2021 - RICT Lung Ethics Protocol - trcked	Summary of Changes	12/May/2021	
12May2021 - RICT Lung Protocol - trcked	Summary of Changes	12/May/2021	

REB members involved in the research project do not participate in the review, discussion or decision.

The Western University HSREB operates in compliance with, and is constituted in accordance with, the requirements of the TriCouncil Policy Statement: Ethical Conduct for Research Involving Humans (TCPS 2); the International Conference on Harmonisation Good Clinical Practice Consolidated Guideline (ICH GCP); Part C, Division 5 of the Food and Drug Regulations; Part 4 of the Natural Health Products Regulations; Part 3 of the Medical Devices Regulations and the provisions of the Ontario Personal Health Information Protection Act (PHIPA 2004) and its applicable regulations. The HSREB is registered with the U.S. Department of Health & Human Services under the IRB registration number IRB 00000940.

Please do not hesitate to contact us if you have any questions.

Sincerely,

Ms. Nicola Geoghegan-Morphet , Ethics Officer on behalf of Dr. Philip Jones, HSREB Chair

Note: This correspondence includes an electronic signature (validation and approval via an online system that is compliant with all regulations).

Appendix B – Curriculum Vitae

Education

2018-present	PhD Medical Biophysics Candidate (CAMPEP accredited) Supervisors: Dr. Stewart Gaede, Dr. Ting-Yim Lee Thesis: *Anatomical and Functional Lung Imaging with Volumetric Computed Tomography in Non-Small cell Lung Cancer* **The University of Western Ontario, London, Canada**
2016-2017	MSc Medical Biophysics 2017 Supervisor: Dr. Grace Parraga Thesis: *Evaluating Small Airways Disease in Asthma and COPD using the Forced Oscillation Technique and Magnetic Resonance Imaging* **The University of Western Ontario, London, Canada**
2011-2016	BSc Honours Physics, Co-Operative Program 2016 **The University of Waterloo, Waterloo, Canada**

Positions

Sept 2018-Aug 2020	**London Regional Cancer Program** CAMPEP QA-ship Coordinator – Graduate Student Assistant Department of Medical Biophysics, University of Western Ontario Supervisor: Dr. Robert Stodilka
2018-present	**University of Western Ontario, London, Ontario** Graduate Research Assistant, PhD Candidate Department of Medical Biophysics, University of Western Ontario Supervisor: Dr. Stewart Gaede
2016-2017	**Robarts Research Institute, London, Ontario** Graduate Research Assistant, MSc Candidate Department of Medical Biophysics, University of Western Ontario Supervisor: Dr. Grace Parraga
2015-2016	**University of Waterloo, Waterloo, Ontario** Undergraduate Research Assistant Supervisor: Dr. Melanie Campbell Project: 'Polarization Properties of Amyloid Beta in the Retina in an Animal Model of Alzheimer's Disease'
Sept-Dec 2014, May-Aug 2015	**London Regional Cancer Program, London, Ontario** Undergraduate Co-op Student Supervisors: Dr. Stewart Gaede, Dr. Slav Yartsev

Sept 2013- April 2014	**Northeast Cancer Centre** **Sudbury, Ontario** Undergraduate Co-op Student Supervisor: Dr. Daniel Provost
Jan-April 2013	**SNOLAB** **Lively, Ontario** Undergraduate Research Assistant Supervisor: Dr. Chris Jillings

Honours and Awards

June 2021	**Poster Presentation Award** Western University Department of Oncology Research Education Day Institutional
June 2019	**Magna Cum Laude Presentation Award** London Imaging Discovery Day Institutional
May 2019	**Alexander Graham Bell Canada Graduate Scholarship Doctoral (CGS D)** Natural Sciences and Engineering Research Council of Canada (NSERC) National ($105,000 over 3 years)
May 2019	**Ontario Graduate Scholarship (declined)** Provincial ($15,000, 1 year)
July 2018	**Lawson Internal Research Fund Studentship** Lawson Health Research Institute Institutional ($15,000, 1 year)
September 2017	**AC Groom Graduate Seminar Award** Department of Medical Biophysics, University of Western Ontario Institutional ($500)

Publications

A Peer-Reviewed Journal Manuscripts (5)

1. **HM Young**, CK Park, OW Chau, TY Lee, and S Gaede. Technical Note: Volumetric Computed Tomography for Radiotherapy Simulation and Treatment Planning. *J Appl Clin Med Phys. July 2021. doi:10.1002/acm2.13336*

2. **HM Young,** F Guo, RL Eddy, GN Maksym, and G Parraga. Oscillometry and Pulmonary MRI Measurements of Ventilation Heterogeneity in Obstructive Lung

Disease: Relationship to Quality of Life and Disease Control. *J Appl Physiol 125: 73–85, 2018. doi: https://doi.org/10.1152/japplphysiol.01031.2017.*

3. **HM Young**, RL Eddy, and G Parraga. MRI and CT Lung Biomarkers: Towards an *In Vivo* Understanding of Lung Biomechanics. *Invited Review, Clinical Biomechanics. 66: 107-122, 2019. doi: 10.1016/j.clinbiomech.2017.09.016.*
4. E Lessard, **HM Young**, A Bhalla, D Pike, K Sheikh, DG McCormack, A Ouriadov and G. Parraga. Pulmonary Magnetic Resonance Imaging Biomarkers of Regional Airspace Enlargement in Alpha-1 Antitrypsin Deficiency. Acad Radiol, 24(11), 1402-1411. doi: 10.1016/j.acra.2017.05.008.
5. K Sheikh, A Bhalla, A Ouriadov, **HM Young**, CM Yamashita, TM Luu, S Katz and G Parraga. Pulmonary magnetic resonance imaging biomarkers of lung structure and function in adult survivors of bronchopulmonary dysplasia with COPD. Cogent Medicine, 4(1), 1282033. doi: 10.1080/2331205X.2017.1282033

B Proffered Oral Presentations (16)

1. **HM Young**, F Su, TY Lee and S Gaede. Feasibility of Simultaneous Whole-Lung Ventilation-Perfusion Imaging with Volumetric CT in Non-Small Cell Lung Cancer. Imaging Network Ontario Annual Meeting. March 24, 2022.
2. **HM Young,** F Su, TY Lee and S Gaede. Simultaneous Whole- Lung Ventilation-Perfusion Imaging with Volumetric CT in Non-Small Cell Lung Cancer: A Feasibility Study. Lung Function Imaging Workshop. August 19, 2021.
3. **HM Young,** F Su, TY Lee and S Gaede. Simultaneous Whole- Lung Ventilation-Perfusion Imaging with Volumetric CT in Non-Small Cell Lung Cancer: A Feasibility Study. American Association of Physicists in Medicine Annual Meeting. July 25, 2021.
4. **HM Young**, J Kempe, TY Lee and S Gaede. Evaluation of Motion Artifacts in 4D-CT Simulated from Volumetric Dynamic CT in Non-Small Cell Lung Cancer Patients. Canadian Organization of Medical Physicists Annual Scientific Meeting. June 23, 2021.
5. **HM Young,** F Su, TY Lee and S Gaede. Simultaneous Whole- Lung Ventilation-Perfusion Imaging with Volumetric CT in Non-Small Cell Lung Cancer: A Feasibility Study. Great Lakes Chapter- American Association of Physicists in Medicine Young Investigator Symposium. May 26, 2021.
6. **HM Young,** TY Lee and S Gaede. Impact of Volumetric 4D-CT Motion Artifact Reduction on Ventilation Imaging. Imaging Network Ontario Annual Meeting. March 23, 2021.

7. O Chau, **HM Young**, K Burgers, TY Lee, FS Prato, G Wisenberg and S Gaede. Multi-Modality Imaging Assessment of the Heart and Lungs Before and After Stage III Non-Small Cell Cancer Radiotherapy. Imaging Network Ontario Annual Meeting. March 23, 2021.

8. **HM Young***, O Chau*, K Burgers, TY Lee, FS Prato, G Wisenberg, S Gaede. Multi-modality imaging of the cardio-pulmonary system in stage III non-small cell lung cancer. Joint AAPM COMP Virtual Meeting, Ventilation Workshop. July 12, 2020.

9. **HM Young**, TY Lee, S Gaede. Impact of Volumetric 4D-CT Motion Artifact Reduction on Ventilation Imaging. Joint AAPM COMP Virtual Meeting, Ventilation Workshop. July 12, 2020.

10. **HM Young**, TY Lee, S Gaede. Impact of Volumetric 4D-CT Motion Artifact Reduction on Ventilation Imaging. Joint AAPM COMP Virtual Meeting. July 15, 2020.

11. **HM Young**, TY Lee, S Gaede. Respiratory Motion Characterization and Motion Artefact Reduction Using Volumetric 4-Dimensional Computed Tomography. American Association of Physicists in Medicine Annual Meeting. San Antonio USA. July 14, 2019.

12. **HM Young**, TY Lee, S Gaede. Volumetric 4-dimensional computed tomography for artefact reduction and respiratory motion characterization. London Imaging Discovery Day. London, Canada. June 12, 2019.

13. **HM Young**, K Burgers, TY Lee, S Gaede. Simultaneous Ventilation and Perfusion Imaging with Volumetric 4-Dimensional Computed Tomography. American Association of Physicists in Medicine Annual Meeting, Ventilation Workshop. Nashville USA July 29, 2018.

14. **HM Young**, F Guo, RL Eddy, GN Maksym, G Parraga. Pulmonary MRI Measurements of Ventilation Heterogeneity in Obstructive Lung Disease: Relationship to Oscillometry, Quality of Life and Disease Control. ISMRM 26th Annual Meeting Paris, France June 2018.

15. **HM Young**, DPI Capaldi, K Sheikh, DG McCormack, CM Yamashita, and G Parraga. Ultra-Short Echo Time MRI Quantification of Airspace Enlargement in Bronchopulmonary Dysplasia and Alpha-1 Antitrypsin Deficiency: Parenchyma Destruction, Air trapping or Both? 15th Annual Imaging Network Ontario Symposium, London, Canada, March 15-16, 2017.

16. **HM Young,** M Mulligan, K Jordan, S Gaede. Patient-Specific QA of Respiratory-Gated VMAT using a Programmable Cylindrical Respiratory Motion Insert for the ArcCHECK™ Phantom. World Congress on Medical Physics and Biomedical Engineering 2015, Toronto Canada, June 7-12, 2015.

C Proffered Poster Presentations (23)

1. **HM Young,** F Su, TY Lee and S Gaede. Simultaneous Whole- Lung Ventilation-Perfusion Imaging with Volumetric CT in Non-Small Cell Lung Cancer: A Feasibility Study. Department of Oncology Research and Education Day. June 18, 2021
2. O Chau*, **HM Young***, K Burgers, TY Lee, FS Prato, G Wisenberg and S Gaede. Multi-Modality Imaging Assessment of the Heart and Lungs Before and After Stage III Non-Small Cell Lung Cancer Radiotherapy Department of Oncology Research and Education Day. June 18, 2021
3. **HM Young,** F Su, TY Lee and S Gaede. Simultaneous Whole- Lung Ventilation-Perfusion Imaging with Volumetric CT in Non-Small Cell Lung Cancer: A Feasibility Study. London Health Research Day. May 11, 2021.
4. **HM Young***, O Chau*, K Burgers, TY Lee, FS Prato, G Wisenberg, S Gaede. Multi-modality imaging of treatment response after stage III non-small cell lung cancer radiotherapy. Joint AAPM COMP Virtual Meeting. July 2020.
5. **HM Young,** TY Lee and S Gaede. Volumetric vs. Conventional 4-dimensional CT in Non-Small Cell Lung Cancer Patients. Imaging Network Ontario Annual Meeting. Toronto, Canada. March 27, 2020.
6. **HM Young**, TY Lee and S Gaede. Volumetric 4-dimensional Computed Tomography for Reduction of Respiratory Motion Artefacts. Oncology Research and Education Day 2019. London, Canada. June 14 2019.
7. **HM Young,** TY Lee and S Gaede. Volumetric 4-dimensional Computed Tomography for Reduction of Respiratory Motion Artefacts. London Health Research Day 2019. London Canada. April 30 2019.
8. **HM Young**, TY Lee, S Gaede. Motion Artefact Reduction Using Volumetric 4-Dimensional Computed Tomography. Imaging Network of Ontario Annual Meeting, London Canada. March 28-29 2019.
9. **HM Young,** J Kempe, TY Lee and S Gaede. Preliminary Study of Motion Artefact Reduction in Volumetric 4-dimensional Computed Tomography. American Association of Physicists in Medicine Annual Meeting, Nashville USA. July 29-02 2018.
10. **HM Young,** J Kempe, TY Lee and S Gaede. Preliminary Study of Motion Artefact Reduction in Volumetric 4-dimensional Computed Tomography. UWO Department of Oncology Research and Education Day, London, Canada, June 8 2018.

11. RL Eddy, **HM Young**, A Kassay, DPI Capaldi, S Svenningsen, DG McCormack, G Parraga. Contributions of Large Versus Small Airways to MRI Ventilation Heterogeneity in Asthmatics. ISMRM 26th Annual Meeting Paris, France June 2018.

12. A Westcott, RL Eddy, DPI Capaldi, **HM Young**, DG McCormack, G Parraga. Quantification of Hyperpolarized 3He MRI Ventilation Heterogeneity in Asthmatics: Surface Area of Ventilation Clusters. ISMRM 26th Annual Meeting Paris, France June 2018.

13. C Church, **HM Young**, G Parraga and GN Maksym. Improvements in Functional Image Impedance Modelling of Asthmatic Lungs Using K-means Clustering. ATS 2018 International Conference San Diego, CA, May 18-23, 2018.

14. A Ouriadov, DPI Capaldi, **HM Young**, M Kirby, HO Coxson, DG McCormack and G Parraga. Imaging Biomarkers of Emphysema in COPD and Alpha-1 Antitrypsin Deficiency Patients using Accelerated 129Xe MRI. ATS 2018 International Conference San Diego, CA, May 18-23, 2018.

15. **HM Young**, F Guo, RL Eddy, C Church, G Maksym and G Parraga. Forced oscillation technique and MRI predictions of airway reactance in moderate-severe asthma. ERS International Congress, Milan, Italy, September 9-13 2017.

16. **HM Young**, DPI Capaldi, K Sheikh, DM McCormack, CM Yamashita, and G Parraga. Quantifying Airspace Enlargement in Bronchopulmonary Dysplasia and Alpha-1 Antitrypsin Deficiency Using Ultra-Short Echo Time MRI. Robarts Research Retreat 2017. Robarts Research Institute, Western University June 20 2017.

17. A Bhalla, K Sheikh, **HM Young**, RL Eddy, DG McCormack, TM Luu, S Katz, G Parraga. Asthma Phenotypes in Adult Survivors of Premature Birth Using Functional Magnetic Resonance Imaging. ATS International Conference (2017).

18. Alexei Ouriadov, E Lessard, F Guo, **HM Young**, A Bhalla, M Kirby, H Coxson, DG. McCormack and G Parraga. Biomarkers of Emphysema in COPD and Alpha-1 Antitrypsin Deficiency: 129Xe MRI Morphomics. ATS International Conference (2017).

19. **HM Young**, DPI Capaldi, K Sheikh, DM McCormack, CM Yamashita, and G Parraga. Ultra-Short Echo Time MRI Quantification of Airspace Enlargement in Bronchopulmonary Dysplasia and Alpha-1 Antitrypsin Deficiency: Parenchyma Destruction, Air trapping or Both?. ISMRM 25th Annual Meeting, 6799 (2017).

20. A Ouriadov, E Lessard, F Guo, **HM Young**, A Bhalla, DG McCormack, and G Parraga. Accelerated Diffusion-weighted ^{129}Xe MRI Morphometry of Emphysema in COPD and Alpha-1 Antitrypsin Deficiency Patients. ISMRM 25th Annual Meeting, 2664 (2017).

21. **HM Young**, DPI Capaldi, K Sheikh, DM McCormack, CM Yamashita, and G Parraga. Quantifying Airspace Enlargement in Bronchopulmonary Dysplasia and Alpha-1 Antitrypsin Deficiency Using Ultra-Short Echo Time MRI. London Health Research Day 2017. Schulich School of Medicine and Dentistry, Western University March 28 2017.

22. A. Ouriadov, E. Lessard, F. Guo, **HM. Young**, A. Bhalla, D.G. McCormack and G. Parraga. Accelerated Diffusion-weighted 129Xe MRI Morphometry of Emphysema. Imaging Network of Ontario (ImNO), 15th Annual Imaging Network Ontario Symposium, London, Canada, March 15-16, 2017.

23. S Gaede, **HM Young**, M Mulligan, K Jordan, A Programmable Moving Insert for the ArcCHECK^{TM} Phantom for Dose Verification of Respiratory-Gated VMAT. American Association of Physicists in Medicine Annual Meeting 2015 Anaheim CA Jul 12-16, 2015.

Committees and professional activities

Sept 2020 - present	**Biomedical Imaging Research Centre Student Subcommittee** Student Committee Member
Sept 2018 – Aug 2021	**Western University CAMPEP Steering Committee** Student Representative
Sept 2018-June 2019	**Medical Biophysics Graduate Student Association** Site Representative and Internal Communications Representative
Jan-Aug 2018	**Medical Biophysics Graduate Council Working Group** Student Member
2017- 2019	**Medical Biophysics Graduate Recruitment Committee** Student Member
2017 - 2018	**Inspiring Young Women in STEM Conference 2018** Graduate Program Expo Planning Committee- Member
2013 - 2015	**University of Waterloo** Undergraduate Student Representative Department of Physics

Leadership, Volunteer, and Community Activities

2020-present	**Medical Biophysics Academic Mentorship Program** Mentor, *CAMPEP Advisor*
2015-2016	**Physics Interconnected, University of Waterloo** *Mentor*